Luiz Felipe Meirelles Coelho Rocha

Response of Ricobayo Dam spillway walls to extensive rock scour

MASTER THESIS

Institute of Applied Geosciences
Graz University of Technology

Reviewer:
Univ.-Prof. B.A. M.S. Ph.D. Daniel Scott Kieffer
Institute of Applied Geosciences

Graz, March 2012

DECLARATION

I declare that I have authored this thesis independently, that I have not used other than the declared sources / resources, and that I have explicitly marked all material which has been quoted either literally or by content from the used sources.

Graz, March 2012 Luiz Felipe Meirelles Coelho Rocha

ACKNOWLEDGMENTS

I would like to express my deepest gratitude to my advisor Professor Daniel Scott Kieffer for the numerous discussions and suggestions used to construct this Master Thesis, and also for patiently reviewing the manuscript.

I also like to kindly thank Professors Wulf Schubert and Qian Liu, which were not directly involved on the project but were always promptly to receive me and discuss technical aspects, providing suggestions which helped to enrich the present work.

I am very grateful to my work colleges the geology students Christoph Steinbauer, Markus Kaspar, Britta Larsen and Elisabeth Macher for the pleasant work environment and uncountable discussions which helped to enlarge my geological understanding during this period.

I would also like to thank the staff of the Institute for Applied Geoscience, especially Peter Schreiber and Anna Pendl, and of the Institute for Rock Mechanics and Tunneling, especially the DI Thomas Pilgerstorfer, which provided assistance even in short notice.

I am thankful to Iberdrola S.A., represented by Rafael Landín Zorilla and Eduardo Rojo Martinez, for the support provided and access to the Ricobayo Dam site during field work.

I would like to acknowledge my friends from academic years in Brazil and in Austria, namely Horea Hundorfean and the Engineers Fernando Vecina, Tomaz Capelato, Tales Oliveira, André Dias, Ciro Costa Galvão, João Nuno Santos, Mario Fuchsberger and Alexander Kluckner.

Lastly and more important I would like to dedicate this work to my parents Eng. João Carlos Coelho Rocha and Maria Beatriz Rocha, for the education and support provided during all these years. I cannot forget my brothers and all members of my family for the love and deepest friendship, as well as Nora Kandler for the support during these years in Graz.

Abstract

Scour processes are of great concern for hydropower structures. The understanding of large erosion processes, their causes, consequences and development, are of great importance to avoid failure of dam structures, which are related to unacceptable losses of human life and infrastructure. This Master Thesis studies the influence of slope instabilities on rock scour processes of dam spillways and its influences on the sidewalls of eroding channels. The work couples a detailed rock mass characterization with a deterministic and probabilistic block theory analysis to better assess the causes of a large scour event that occurred on the spillway of the Ricobayo Dam in Spain. Analyses show poor stability behaviour for steep slopes generated by primary scour of the spilling channel. This poor geometrical situation appears to have played a central role on the rapid back migration of the spillway head wall, as well as on the formation and enlargement of the plunge pool. Scour is seen as the main factor to trigger slope failures on the spillway by opening free space for potentially unstable blocks to slide. In this matter construction and remediation may have strongly influenced the process, since the spillway was the only option to conduct exceeding flow during construction and remediation seems to have forced the erosion process to concentrate at the bottom of the plunge pool, augmenting relief for the critic slopes. The sum of these factors, operation constrains, little time between scour events for effective remediation measures and unexpected rock mass conditions may have triggered scour, initiating one of the largest scour processes documented at dam spillways.

Kurzfassung

Auskolkungsvorgänge sind beim Bau von Wasserkraftwerken von großer Bedeutung. Es ist wichtig, weitreichende Erosionsprozesse, ihre Ursachen, Konsequenzen und Entwicklung zu verstehen, um ein Versagen von Dammstrukturen zu vermeiden, welches in den meisten Fällen mit der unnötigen Zerstörung von Infrastruktur und dem Verlust von Menschenleben einhergeht. Diese Masterarbeit beschäftigt sich mit dem Einfluss von Hangrutschungen auf Auskolkungsvorgänge in Wehrüberfällen und auf die Seitenwände von Erosionsrinnen. Diese Arbeit soll eine detaillierte Gesteinscharakterisierung mit einer deterministischen Blocktheorie-Analyse und einer Wahrscheinlichkeitsanalyse derselben verbinden, um die Ursachen von massiven Auskolkungsvorgängen, wie sie im Fall des Ricobayo Dammes in Spanien erfolgten, besser bewerten zu können. Analysen zeigen, dass die Instabilität der Steilhänge durch eine primäre Auskolkung der Erosionsrinnen verursacht worden war. Wie sich herausstellte, spielte diese Situation eine entscheidende Rolle bei der raschen Erosion der Frontwand, sowie bei der Bildung und Vergrößerung des Tosbeckens. Auskolkung gilt als der Hauptauslöser von Hangrutschungen im Hochwasserüberfall, da dadurch Raum für mögliche instabile Blöcke geschaffen wird. Da der Hochwasserüberfall in der Bau- und Sanierungsphase die einzige Möglichkeit bot, die Strömung aufzunehmen, haben Konstruktion und Sanierung den Prozess auf diese Weise vermutlich stark beeinflusst. Der Erosionsprozess konzentrierte sich dabei auf den Boden des Tosbeckens und entlastete dabei gleichzeitig die kritischen Hänge. Die Summe aller Faktoren – die Einschränkungen bei der Ausführung, knappe Zeit zwischen den einzelnen Auskolkungsvorgängen und somit für effektive Sanierungsmaßnahmen, ebenso wie unerwartete Beschaffenheit der Gesteinsmassen – könnte Ursache für die Auskolkung gewesen sein, welche einen der größten jemals dokumentierten Auskolkungsvorgänge in einer Entlastungsanlage in Gang setzte.

Table of Contents

1 Introduction 1

2 Aim and Scope 3

3 Method 4

3.1 Rock mass characterization 4

3.1.1 Orientation 4

3.1.2 Spacing 5

3.1.3 Persistence 6

3.1.4 Roughness 7

3.1.5 Wall strength 9

3.1.6 Aperture 11

3.1.7 Filling 11

3.1.8 Seepage 11

3.1.9 Block size 11

3.2 Block Theory 12

3.2.1 Concept 12

3.2.2 Types of Blocks 13

3.2.3 The block pyramid 14

3.2.4 Theorem of finiteness – Shi's theorem 15

3.2.5 Block Removability 17

3.2.6 Kinematics and stability of removable blocks 19

3.2.7 Probabilistic approach 26

3.3 Software 28

3.3.1 Sphaira and Fracman 28

3.3.2 ShapeMetrix^{3D} 28

3.3.3 RisCAN PRO 29

3.3.4 ArcMap 29

3.3.5 Swedge and RocPlane 30

4 The Ricobayo Dam 31

4.1 Original spillway description 33

4.2 Scour events 1934-1939 35

4.3 Scour consequences 41

4.4 Spillway remediation in the early 1940's 41

4.5 Scour event of 1962 and modification of the spillway outlet 44
5 Regional Geology.....46
5.1 Geological setting 46
5.2 Stratigraphy 48
5.3 Structural geology 49
5.3.1 Fold and faults 49
5.4 Metamorphism and Plutonism 53
6 Rock mass characterization 54
6.1 Orientation and joint set determination 54
6.2 Spacing 59
6.3 Persistence 59
6.3.1 Lineament studies and Trace maps 61
6.4 Roughness 65
6.5 Wall strength 68
6.6 Aperture 70
6.7 Filling 71
6.8 Seepage 71
6.9 Block size 72
6.10 Shear strength of discontinuities 73
7 Stability Analysis 75
7.1 Input parameters 75
7.1.1 Slope parameters 75
7.1.2 Joint parameters 77
7.1.3 Water 77
7.1.4 Sampling size 78
7.2 Head wall 81
7.3 Left wall 88
7.4 Right wall 95
8 Conclusion.....102
References 107
APPENDIX 111

List of Figures

Figure 1.1 – The Ricobayo plunge pool 2
Figure 3.1 – Dip vector definition 5
Figure 3.2 – Stereographic projections 5
Figure 3.3 – Termination type terminology 7
Figure 3.4 – Typical roughness profiles 8
Figure 3.5 – Roughness profiles and respective JRC values 9
Figure 3.6 – Block types 13
Figure 3.7 – Block pyramid 15
Figure 3.8 – Block finiteness in 2D 16
Figure 3.9 – Block removability in 2D 18
Figure 3.10 – System of forces acting on a block 19
Figure 3.11 – Flow chart for Monte Carlo simulation 27
Figure 3.12 - Principle of the Shape Metrix^{3D} surface measurement 29
Figure 3.13 – Swedge probabilistic analysis 30
Figure 4.1 – Geographic location of the Ricobayo Dam 32
Figure 4.2 – General plan, 1933 33
Figure 4.3 - Longitudinal profile A-A' of the original spillway 34
Figure 4.4 – Esla River flow regime 34
Figure 4.5 – Initial spillway operation 35
Figure 4.6 – Spillway situation during second scour event 36
Figure 4.7 – Right wall situation in 26/03/1934 37
Figure 4.8 – Remediation works of 1934 38
Figure 4.9 – Spilling gorge before and after third scour event 38
Figure 4.10 – Detail of the spillway after first phase of the fourth scour event 39
Figure 4.11 – Right wall in 28/04/1936 40
Figure 4.12 – Plunge pool situation in 21/10/1936 40
Figure 4.13 – Scour evolution, 1933 to 1939 41
Figure 4.14 – Plan view of the plunge pool 42
Figure 4.15 – Longitudinal profile B-B' of the plunge pool 43
Figure 4.16 – Deflector walls and emissary 44
Figure 4.17 – Concrete erosion observed in 1961 45
Figure 4.18 – Splitters at the spillway outlet 45
Figure 5.1 - Iberian Massif zones. 47

Figure 5.2 – Geological map of the area..... 50
Figure 6.1 – Granitoid rocks outcropping at Ricobayo Dam 54
Figure 6.2 – Probability contours of all measured data..... 55
Figure 6.3 – Statistical analysis of structural orientation data – Joint set 1..... 55
Figure 6.4 – Statistical analysis of structural orientation data – Joint set 2..... 56
Figure 6.5 – Statistical analysis of structural orientation data – Joint set 3..... 56
Figure 6.6 – Statistical analysis of structural orientation data – Joint set 4..... 56
Figure 6.7 – Statistical analysis of structural orientation data – Joint set 5..... 57
Figure 6.8 - Geographic distribution of joint orientation measurements..... 58
Figure 6.9 – Termination type of all measured data 60
Figure 6.10 – Trace map locations 61
Figure 6.11 – Trace map 1 62
Figure 6.12 – Trace map 2 63
Figure 6.13 – Major lineaments interpreted from the topography and field data..... 64
Figure 6.14 – Set 1 slickensides..... 65
Figure 6.15 – JRC histogram of all measured joint surfaces 65
Figure 6.16 – JRC histogram – Set 1 66
Figure 6.17 - JRC histogram – Set 2 66
Figure 6.18 - JRC histogram – Set 3 67
Figure 6.19 - JRC histogram – Set 4 67
Figure 6.20 – JRC histogram – Set 5 67
Figure 6.21 – Estimated wall strength index values..... 68
Figure 6.22 – Estimated weathering index values 69
Figure 6.23 – Typical weathering situation 69
Figure 6.24 – Strong weathering observed along wet discontinuity planes. 70
Figure 6.25 – Typical joint plane apertures at the surface and underground..... 70
Figure 6.26 – Joint aperture in unstable areas 71
Figure 6.27 – Water condition observed in winter of 2011..... 71
Figure 6.28 – Frequency along Scanline – all sets considered..... 72
Figure 6.29 – Rock blocks encountered inside the plunge pool..... 72
Figure 7.1 – Estimated slope directions..... 76
Figure 7.2 – Assumed water pressure distribution..... 78
Figure 7.3 – Probability of failure variation with sample size – Head wall..... 79
Figure 7.4 - Probability of failure variation with sample size – Left wall 80

Figure 7.5 - Probability of failure variation with sample size – Right wall 80
Figure 7.6 – Block removability – Head wall compound slope 81
Figure 7.7 – Mode analysis – Head wall compound slope 82
Figure 7.8 – Probabilistic analyses – Head wall compound slope 84
Figure 7.9 – Ratio of dry to filled probability of kinetic instability – Head wall compound slope 85
Figure 7.10 – Mean block volume obtained from probabilistic analyses – Head wall compound slope 87
Figure 7.11 – Block removability – Left wall compound slope 88
Figure 7.12 – Mode analysis – Left wall compound slope 89
Figure 7.13 - Probabilistic analyses – Left wall compound slope 91
Figure 7.14 - Ratio of dry to filled probability of kinetic instability – Left wall compound slope 92
Figure 7.15 - Mean block volume obtained from probabilistic analyses – Left wall compound slope 93
Figure 7.16 – Rock wedge moulds observed on the left wall 94
Figure 7.17 – Block removability – Right wall compound slope 95
Figure 7.18 – Mode analysis – Right wall compound slope 96
Figure 7.19 - Probabilistic analyses – Right wall compound slope 98
Figure 7.20 – Ratio of dry to filled probability of kinetic instability – Right wall compound slope 99
Figure 7.21 - Mean block volume obtained from probabilistic analyses – Right wall compound slope 101
Figure 8.1 – Ricobayo Dam plunge pool 106

1 Introduction

Rock scour is a process of great interest for dam authorities and owners. Failure of dam structures can be disastrous and result in unacceptable loss of life, infrastructure, and environmental resources. To reduce the risk of failure, all failure modes must be understood and should be quantified. Scour processes and related events represent a potential failure mode involving structural undermining and debutressing.

Erosion processes are not easy to assess because of the nature of the driving forces related to water action and also, in the case of rock, the uncertainties about the rock mass conditions. The problem has been studied in the 90's by a number of researches, which intended to apply the Erodibility Index developed by Kirsten (1982) to scour. This semi-empirical approach is today a respected tool in the field and has been particularly well developed by Annandale (2006). This geomechanical index is used to quantify the relative ability of an earth material to resist the erosive capacity of water. Another large contribution in the field has been made by Bollaert and Schleiß (2005). Their method is based on a near prototype experiment and intended to overcome limitations of empirical methods and take into account basic physical processes of rock mass break-up. Both methods take into account some rock mass characteristics, but the rock mechanics advances achieved along the years did not find application in the field of study. Block Theory, developed by Goodman and Shi (1985), is one method that quantifies structural characteristics of blocky rock systems and could be a powerful tool to enhance the quality of scour analysis as suggested by Annandale (2006).

Figure 1.1 – The Ricobayo plunge pool

The following work applies Block Theory, in a deterministic and probabilistic manner, to a known scour case at Ricobayo Dam (Figure 1.1). This case has been studied by Annandale (2006), but the back-erosion of the head wall and related effects that led to large failures of the side walls and subsequent enlargement of the plunge pool have not been considered in detail. Rock slope failure processes had a considerable influence on the migration of the head wall towards the reservoir and on the stability of the plunge pool sidewalls, consequently influencing the geometry of the formed plunge pool and the volume of eroded material.

2 Aim and Scope

The objective of this Master Thesis is to assess the stability and response of the rock walls surrounding the plunge pool at Ricobayo Dam to extensive rock scour. It is intended to clarify how geological conditions and slope instabilities may have influenced the plunge pool enlargement and back migration of the head wall. To accomplish this objective the following scope of work has been performed:

- Review of available historical records and construction details of the original spillway;
- Geological and geotechnical characterization of the site;
- Stability analyses and evaluation of rock slope response.

Historical records reviewed include published literature, together with records provided by the dam owner (Iberdrola S.A.). Evaluation of geological conditions was based on published literature and site-specific field work performed in February of 2011. The field data has been evaluated and utilized in 3D stability analyses, from which relevant conclusions were developed.

3 Method

This chapter presents the theoretical basis used for the data acquisition and analyses performed in the work. The method for the acquisition of data and rock mass characterization is presented first, followed by the theoretical basis of block theory, which was used for the kinematical and stability analyses. The chapter also presents the software used within the work, with some comments about their functionality and theoretical background.

3.1 Rock mass characterization

The rock mass discontinuities have been described/characterized according to the ISRM Suggested Methods (1981). The main parameters and the data acquisition methods are described in this item. They are: Orientation, Spacing, Persistence, Roughness, Wall strength, Aperture, Filling, Seepage, and Block size.

3.1.1 Orientation

The orientation of a discontinuity relative to an engineering structure largely controls the possibility of instabilities and deformation development, as well as the geometry of individual blocks forming the rock mass (ISRM, 1981). Orientation of a discontinuity is described by its dip vector. The dip vector is defined as the line of steepest inclination measured with the horizontal, the dip (α) is the angle with the horizontal and the dip direction (β) is the azimuth from true north of this line. These parameters are illustrated in Figure 3.1. In this master thesis the discontinuities orientations have been measured using two methods: manually with a compass and digitally with the photogrammetric software ShapeMetriX^{3D}.

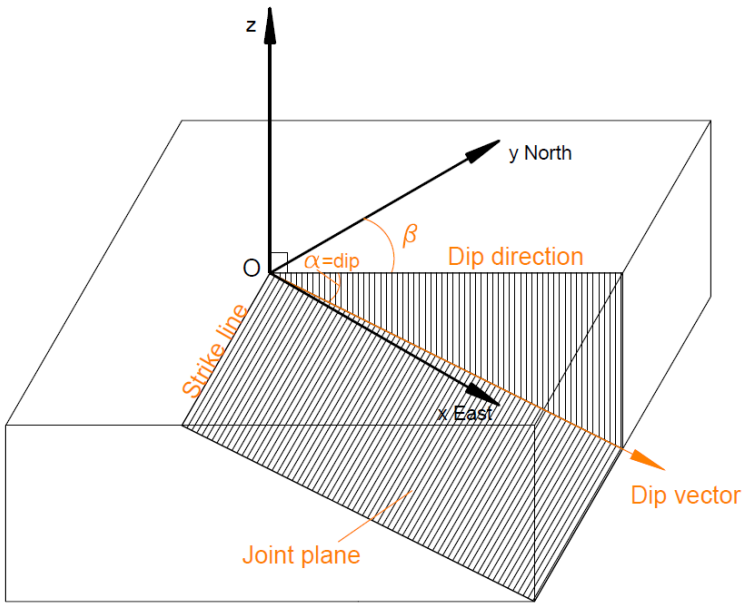

Figure 3.1 – Dip vector definition – adapted from Goodman and Shi (1985)

- Results presentation

The results from orientation measurements (lines and planes) are presented in equal area stereographic projections. All the results are presented in lower half-space reference circles (LHRC). Figure 3.2 illustrates how a stereographic projection works and how planes, poles and lines are projected into equal area stereonets.

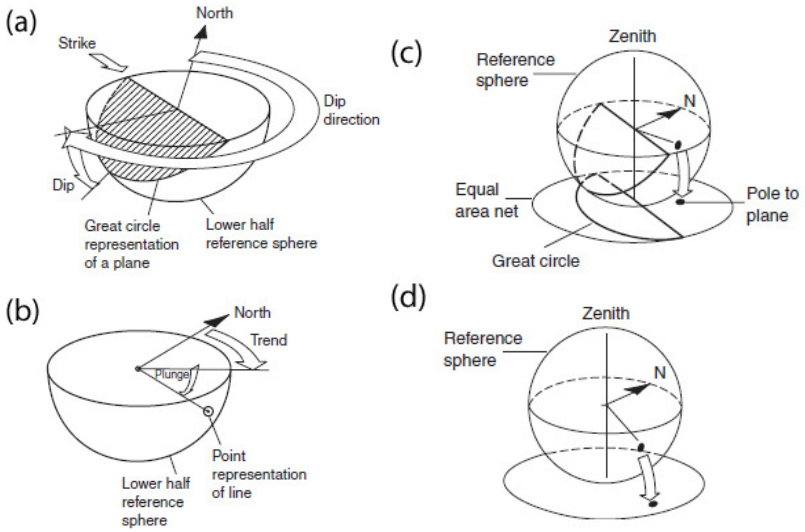

Figure 3.2 – Stereographic projections

3.1.2 Spacing

The spacing of adjacent discontinuities governs the size of intact rock blocks, influencing also the mechanical behaviour (failure modes and deformability),

permeability, and seepage characteristics (ISRM, 1981). The spacing of adjacent discontinuities has been acquired along a scanline and with the photogrammetric software ShapeMetrix^{3D}. The results are presented as mean and standard deviation for each joint set. The spacing description follows the suggested terminology of ISRM (1981) presented in Table 3.1.

Description	Spacing
Extremely close spacing	< 2 cm
Very close spacing	2-6 cm
Close spacing	6-20 cm
Moderate spacing	20-60 cm
Wide spacing	60-200 cm
Very wide spacing	200-600 cm
Extremely wide spacing	>600 cm

Table 3.1 – Spacing terminology

3.1.3 Persistence

Discontinuity persistence and the way in which a discontinuity terminates, in solid rock or at another discontinuity, determines the degree to which intact rock is involved in a failure process (ISRM, 1981). The persistence of the discontinuities has been described in the field and estimated along a scanline and with the software ShapeMetrix^{3D}. The results are presented as mean and standard deviation for each joint set. The trace lengths are described according to ISRM Suggested Methods (1981). The description terminology is presented in Table 3.2.

Description	Persistence
Very low persistence	< 1 m
Low persistence	1-3 m
Medium persistence	3-10 m
High persistence	10-20 m
Very high persistence	>20 m

Table 3.2 – Persistence terminology

Additionally to persistence, the termination type of each discontinuity has been acquired along the scanline. The terminology in this case is: “X” for unknown termination, “R” for termination in rock, and “D” for termination in another discontinuity. The terminology is illustrated in Figure 3.3.

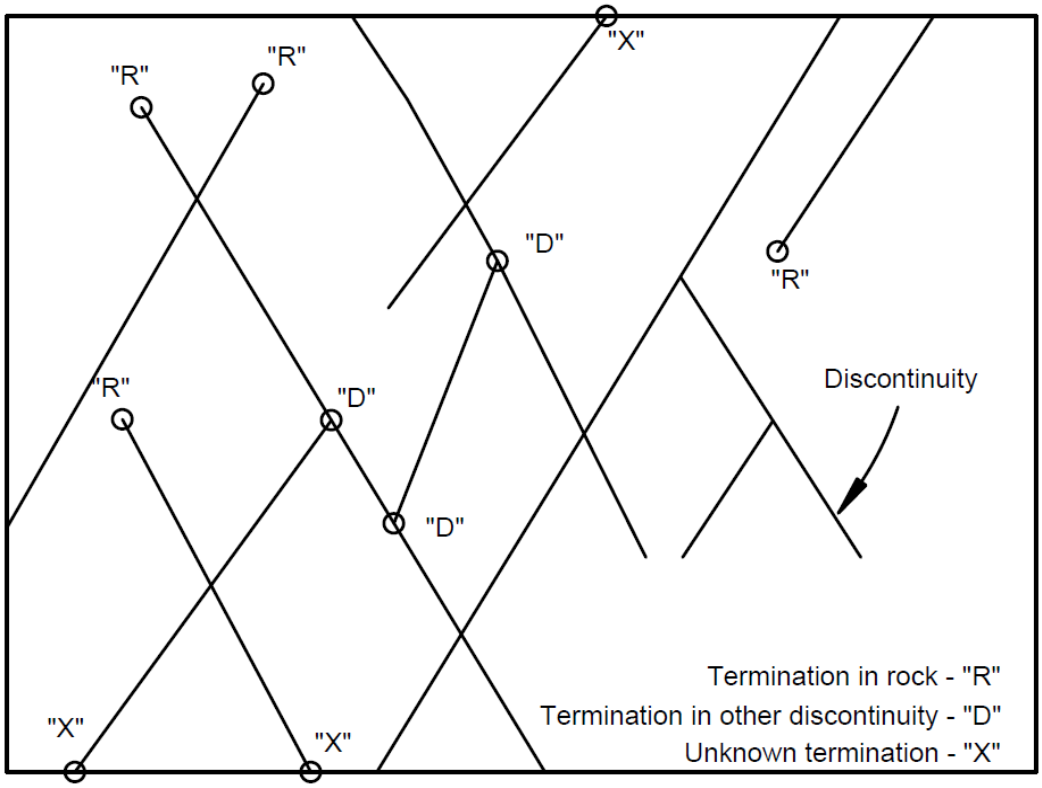

Figure 3.3 – Termination type terminology

3.1.4 Roughness

Wall roughness is an important component of the shear strength of discontinuities, especially for unfilled joints. Its importance decreases with increasing aperture, filling thickness and degree of previous displacement (ISRM, 1981). Large scale (1 to 10 meters) roughness has been described for the rock mass characterization. The descriptive terms and typical roughness profiles used for the characterization are presented in Figure 3.4. To estimate the shear strength of the discontinuities, small scale (10cm) roughness has also been acquired. These measurements are given by the Joint Roughness Coefficient (JRC) from Barton and Choubey (1977). Figure 3.5 illustrates the typical profiles and related JRC values.

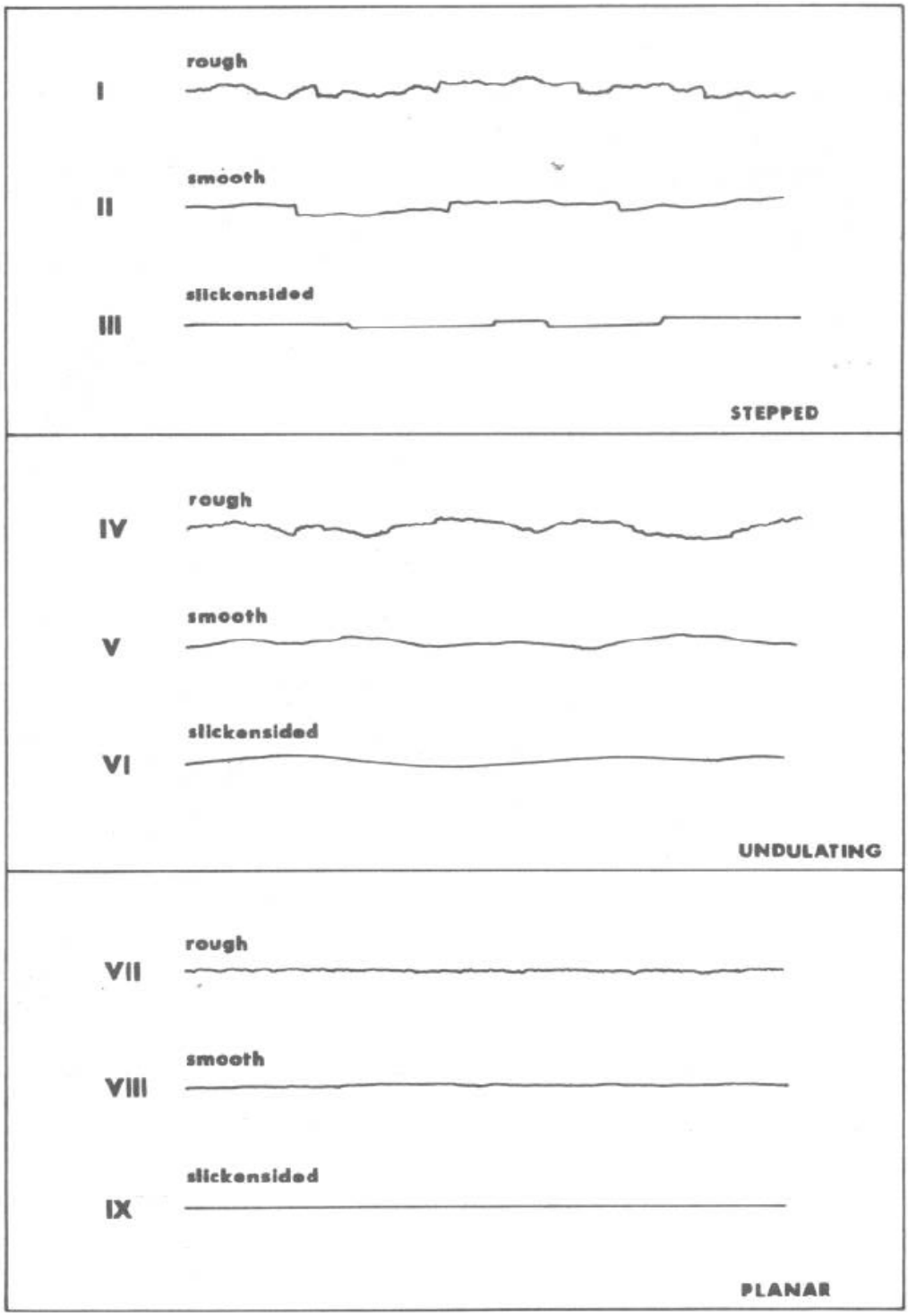

Figure 3.4 – Typical roughness profiles and nomenclature. Horizontal and vertical scale 1 to 10 metres (ISRM, 1981).

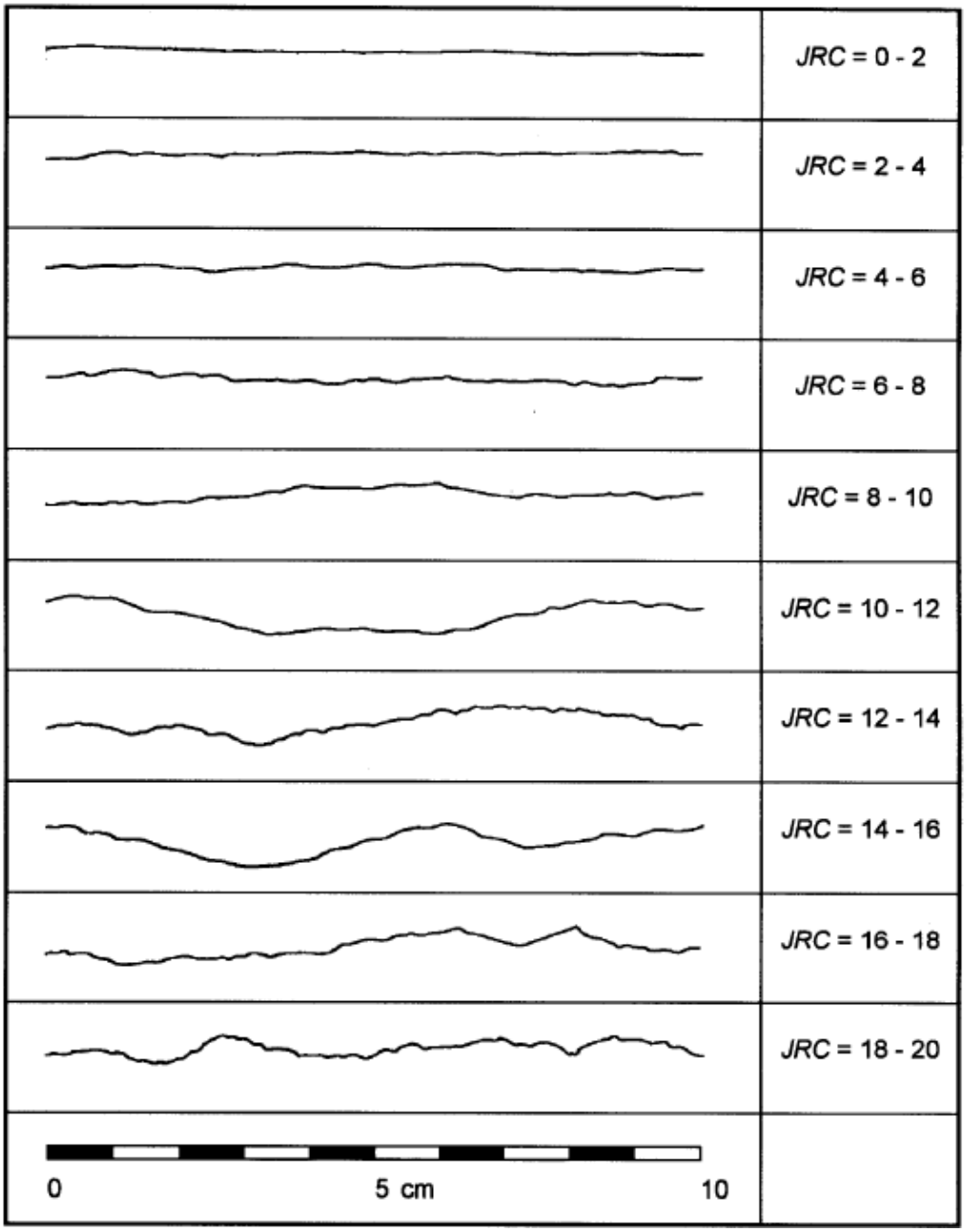

Figure 3.5 – Roughness profiles and respective JRC values (Barton and Choubey, 1977)

3.1.5 Wall strength

An important component of shear strength and deformability of a discontinuity is the compressive strength of the rock of its walls, especially if the walls are in direct contact (unfilled joint) (ISRM, 1981). Weathering (and alteration) affects wall strength, and is therefore an essential part of the description of wall strength (ISRM, 1981). The ISRM Suggested Methods (1981) provide tables for the description/estimation of these parameters. Table 3.3 presents descriptive terms for weathering grades, and Table 3.4 for wall strength.

Term	Description	Grade
Fresh	No visible sign of rock material weathering: perhaps slight discoloration on major discontinuity surfaces.	I
Slightly weathered	Discoloration indicates weathering of rock material and discontinuity surfaces. All the rock material may be discoloured by weathering and may be somewhat weaker externally than its fresh condition.	II
Moderately weathered	Less than half of the rock material is decomposed and/or disintegrated to a soil. Fresh and discoloured rock is present either as a discontinuous framework or as corestones.	III
Highly weathered	More than half of the rock material is decomposed and/or disintagreted to a soil. Fresh or discoloured rock is present either as a discontinuous framework or as corestones.	IV
Completely weathered	All the rock material is decomposed and/or disintegrated to soil. The original mass structure is still largely intact.	V
Residual soil	All the rock material is converted to soil. The mass structure and material fabric are destroyed. There is a large change in volume, but the soil has not been significantly transported.	VI

Table 3.3 – Weathering grade of rock material (ISRM, 1981)

Grade	Description	Field identification	Approx. range of uniaxial compressive strength (MPa)
S1	Very soft clay	Easily penetrated several inches by fist	< 0,025
S2	Soft clay	Easily penetrated several inches by thumb	0,025 – 0,05
S3	Firm clay	Can be penetrated several inches by thumb with moderate effort	0,05 – 0,10
S4	Stiff clay	Readily indented by thumb but penetrated only with great effort	0,10 – 0,25
S5	Very stiff clay	Readily indented by thumbnail	0,25 – 0,50
S6	Hard clay	Indented with difficulty by thumbnail	>0,50
R0	Extremely weak rock	Indented by thumbnail	0,25 – 1,0
R1	Very weak rock	Crumbles under firm blows with point of geological hammer, can be peeled by a pocket knife	1,0 – 5,0
R2	Weak rock	Can be peeled with a pocket knife with difficulty, shallow indentations made by firm blow with point of geological hammer	5,0 – 25
R3	Medium strong rock	Cannot be scraped or peeled with a pocket knife, specimen can be fractured with single firm blow of geological hammer	25 – 50
R4	Strong rock	Specimen requires more than one blow of geological hammer to fracture it	50 – 100
R5	Very strong rock	Specimen required many blows of geological hammer to fracture it	100 – 250
R6	Extremely strong rock	Specimen can only be chipped with geological hammer	>250

Table 3.4 – Strength grade of rock material (ISRM, 1981)

3.1.6 Aperture

Aperture affects several rock properties such as shear strength, deformability, and water conductivity. Aperture is defined as the perpendicular distance separating the walls of an open discontinuity, and is distinguished from width of a filled discontinuity (ISRM, 1981). Therefore, it has also been described. The terminology used is presented in Table 3.5.

Aperture	Description	
< 0,1 mm	Very tight	"Closed" features
0,1 – 0,25 mm	Tight	
0,25 – 0,5 mm	Partly open	
0,5 – 2,5 mm	Open	"Gapped" features
2,5 – 10 mm	Moderately wide	
>10mm	Wide	
1 – 10 cm	Very wide	"Open" features
10 – 100 cm	Extremely wide	
>1m	Cavernous	

Table 3.5 – Aperture descriptive terms (ISRM, 1981)

3.1.7 Filling

"Filling is the term for material separating the adjacent rock walls of discontinuities" (ISRM, 1981). The filling description includes the nature of the material, width of the discontinuity and filling strength. Filling material has been described when present. Filling strength has been described using terms presented in Table 3.4.

3.1.8 Seepage

The prediction of groundwater behaviour may give advance warning of instability or construction difficulty (ISRM, 1981). Seepage has been reported when present, in the case of flow the quantity would be reported.

3.1.9 Block size

"The block size is an extremely important indicator of rock mass behaviour" (ISRM, 1981). The mechanical behaviour of the rock mass under given stress conditions is determined by the block size and shear strength properties between adjacent blocks (ISRM, 1981). The rock mass has been described by the terms presented in Table

3.6 to give an estimation of block shapes. Table 3.7 presents descriptive terms to the qualitative and quantitative estimation of block size according to the volumetric joint count (J_v).

Term	Description
Massive	Few joints or very wide spacing
Blocky	Approximately equidimensional
Tabular	One dimension considerably smaller than the other two
Columnar	One dimension considerably larger than the other two
Irregular	Wide variations of block size and shape
Crushed	Heavily jointed to "sugar cube"

Table 3.6 – Block size and shape relative description (ISRM, 1981)

Description	J_v (joints/m³)	Block size
Very large blocks	< 1,0	Over 8 m³
Large blocks	1 – 3	0,2 – 8 m³
Medium-sized blocks	3 – 10	0,008 – 0,2 m³
Small blocks	10 – 30	0,0002 – 0,008 m³
Very small blocks	>30	Less than 0,0002 m³

Table 3.7 – Block size relative description for J_v (ISRM, 1981)

3.2 Block Theory

Several analytical methods are available to evaluate rock slope instabilities. Among them, block theory was chosen to perform the stability analysis of the plunge pool walls of Ricobayo. The method was published by Goodman and Shi in 1985. The following resumes the most important aspects of the theory and was completely extracted from the book "*Block Theory and its Application to Rock Engineering*" (1985).

3.2.1 Concept

The objective of block theory is to find and describe the most critical blocks around an excavation, and to establish their support requirements (Goodman, 1989). Original block theory takes just translational failure modes into account. A series of simplifying assumptions were adopted by the authors (Goodman and Shi, 1985), and are briefly listed:

- All joint surfaces are assumed to be perfectly planar;
- Joint surfaces are assumed to extend entirely through the volume of interest;
- Blocks are assumed to be rigid;
- The discontinuities and free faces are assumed to be determined as input parameters.

3.2.2 Types of Blocks

A block is determined by the intersection of a particular set of discontinuities. Criteria have been established for the relative importance of blocks (Goodman and Shi, 1985). Figure 3.6 illustrates the block types according to block theory.

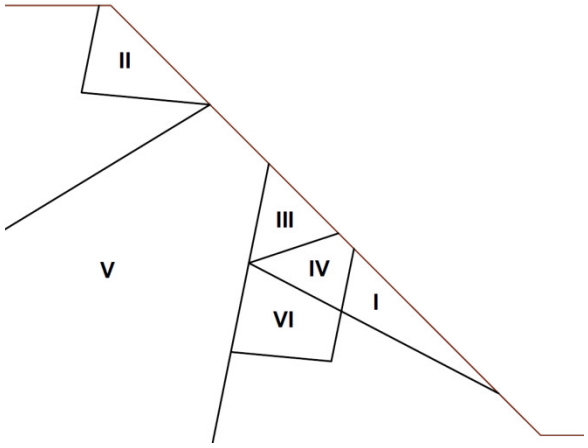

Figure 3.6 – Block types

Block type VI is a special case called “joint block”. Such a block is formed just by joint surfaces and has no face on the excavation perimeter. Block type V possesses a free face, but it is infinite unless new cracks are formed, what by definition is not covered by block theory. Type IV is finite, but it is not removable. There is no direction where it can move without pushing into adjacent rock mass. These blocks are called “tapered” (Goodman, 1989).

Remaining blocks are *finite* and *removable*. To differentiate them stability must be evaluated. Type III is safe under the action of gravity, even without friction. Type II is safe with enough friction; these are called “potential key blocks”. Blocks of type I are not just removable but also oriented in an unsafe manner in relation to the acting forces; these blocks are called “key blocks” (Goodman, 1989).

A system to distinguish the block types is provided by Goodman and Shi (1985). The first step is to separate removable (Types I, II and III) from non-removable blocks (Types IV, V and VI) by means of Shi's theorem of removability. Then the distinction between types II and III is performed by analysing the direction of sliding and falling tendencies given the direction of the resultant force (a "mode analysis"). Finally a limit equilibrium analysis (LEA) defines the key blocks and their support requirements (Goodman, 1989).

3.2.3 The block pyramid

The concept of the block pyramid is fundamental to understand the following aspects of block theory. First, the idea of half-spaces must be introduced. Without any complex mathematical mention a half-space is a region delimited by a plane. A point in space will then be related to this plane as located above or underneath it. These regions are defined as the upper and lower half-spaces, respectively. The upper half-space will be denoted U or 0, and the complementary lower half-space as L or 1. A real block bounded by n nonparallel surfaces is formed by the intersection of upper and lower half-spaces of joints corresponding to each of its faces (Goodman and Shi, 1985). Recalling the example used by Goodman and Shi (1985), a block might be formed by $U_1U_2U_3L_4L_5$ (upper half-spaces of planes 1, 2 and 3, as well as lower half-spaces of planes 4 and 5). Each plane is shifted to pass through a common origin. The half-spaces of the shifted planes $U_1^0U_2^0U_3^0L_4^0L_5^0$ (the superscript O indicates that the plane in question passes through the origin) will create a pyramid, the "block pyramid" (BP), illustrated in Figure 3.7.

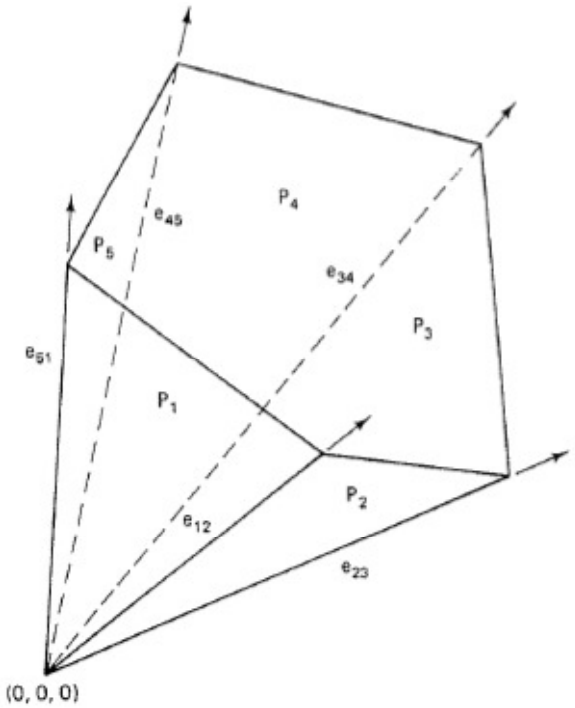

Figure 3.7 – Block pyramid (Goodman and Shi, 1985)

3.2.4 Theorem of finiteness – Shi's theorem

The theorem of finiteness or Shi's theorem states (Goodman and Shi, 1985):

"A convex block is finite if its block pyramid is empty. Conversely, a convex block is infinite if its block pyramid is not empty."

An "empty" pyramid is one that has no edges. The following examples are based on two-dimensional examples used by Goodman and Shi (1985) to illustrate finiteness. In Figure 3.8, two blocks are illustrated. Block A is an infinite block formed by a free face and two joint planes. The block is determined by the intersection of half-spaces U_1, L_2, and L_3. A block pyramid is determined by shifting the half-spaces as required. BP_A is presented directly underneath the block. Since there is a region common to these three half-spaces the block pyramid is not empty, and block A is infinite according to the theorem.

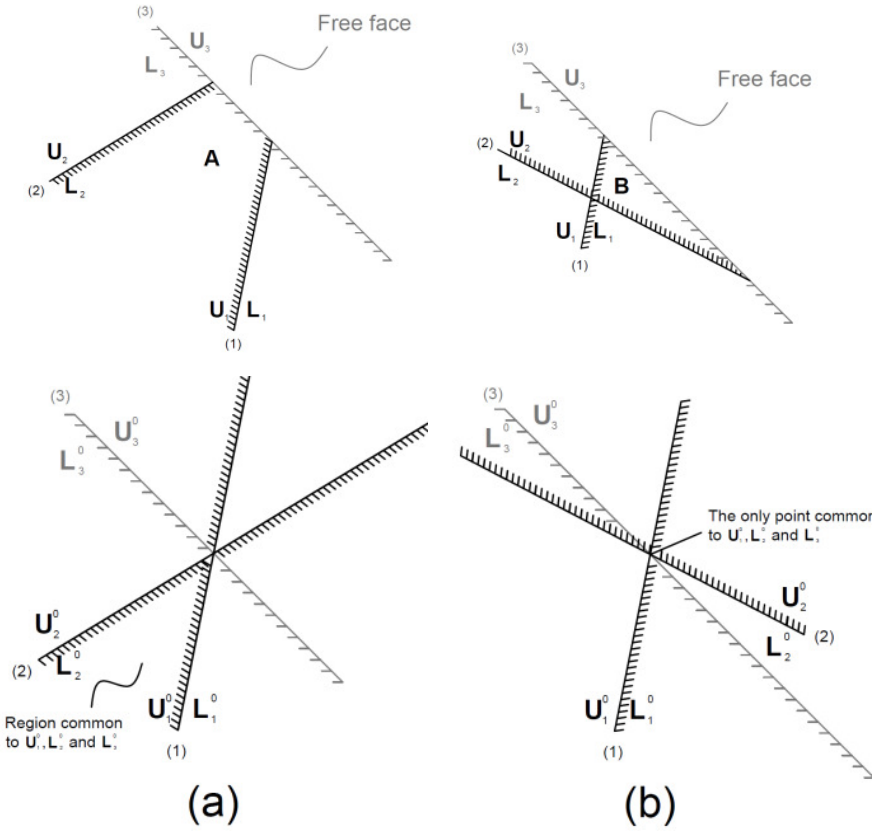

Figure 3.8 – Block finiteness in 2D – based on Goodman and Shi (1985)

Same procedure is followed for block B, but in this case the block shows to be finite using Shi's theorem. The region common to L_1^0 and U_2^0 has no points in common with the region defined by L_3^0, except for the origin itself. There is no edge to the BP_B $L_1^0 U_2^0 L_3^0$, which is therefore "empty".

In the previous examples, one will remark that the block pyramid is defined by free-surface half-spaces and joint-plane half-spaces. The joint-plane subset of half-spaces is designated *joint pyramid* (JP) and the excavation half-spaces as the *excavation pyramid* (EP) (Goodman and Shi, 1985). The block pyramid is defined as the intersection of the joint pyramid and the excavation pyramid for a particular block (Goodman and Shi, 1985):

$$BP = JP \cap EP \qquad \textbf{Eq. 3.1}$$

According to Shi's Theorem, a block will be finite if and only if

$$JP \cap EP = \emptyset \qquad \textbf{Eq. 3.2}$$

Defining the space pyramid (SP) as the complementary to EP (Goodman and Shi, 1985):

$$SP = \sim EP \quad \textbf{Eq. 3.3}$$

Then Eq. 3.2 can also be stated as (Goodman and Shi, 1985): A block is finite if and only if its joint pyramid is entirely contained in the space pyramid, that is, if and only if

$$JP \subset SP \quad \textbf{Eq. 3.4}$$

Equation 3.4 can be easily applied using stereographic projections. In the projection a joint pyramid (JP) will plot as a region delimited by portions of great circles representing planes. The JP's will be identified by a string of digits (0/1, U or L respectively) according to the half-spaces building the JP. Same can be done for the free faces, and the SP will be identified. JP's plotting entirely within the SP will form finite blocks.

3.2.5 Block Removability

The removability of a finite convex block depends on its shape relative to the free faces (Goodman and Shi, 1985). Goodman and Shi (1985) established the necessary and sufficient conditions for the removability of finite blocks through the following theorem:

"A convex block is removable if its block pyramid is empty and its joint pyramid is not empty. A convex block is not removable (tapered) if its block pyramid is empty and its joint pyramid is also empty."

The theorem states that a block determined by a series of joint planes and free surfaces is tapered if the joint-plane half-spaces alone already determine a finite block (Goodman and Shi, 1985).

To illustrate the theorem a two-dimensional example adapted from the work of Goodman and Shi (1985) is presented. In Figure 3.9, two blocks defined by joint

planes and a free surface are presented. Block A is determined by half-spaces $L_1U_2U_3L_4$, where plane 4 is the free face. The JP of this block is shown in Figure 3.9 (a), and is formed by $L_1^0U_2^0U_3^0$. As shown, there is a common region to the shifted half-spaces, therefore JP_A is not empty. The BP $L_1^0U_2^0U_3^0L_4^0$ in this case is empty. According to the theorem, block A is removable. JP_A is not empty and BP_A is empty.

Block B is determined by half-spaces $U_1L_2U_3L_4$. Its joint pyramid is formed by $U_1^0L_2^0U_3^0$, the only point in common to the shifted half-spaces is the origin itself. JP_B is therefore empty, and BP_B is also empty. In this case the theorem states that block B is non removable, therefore "tapered".

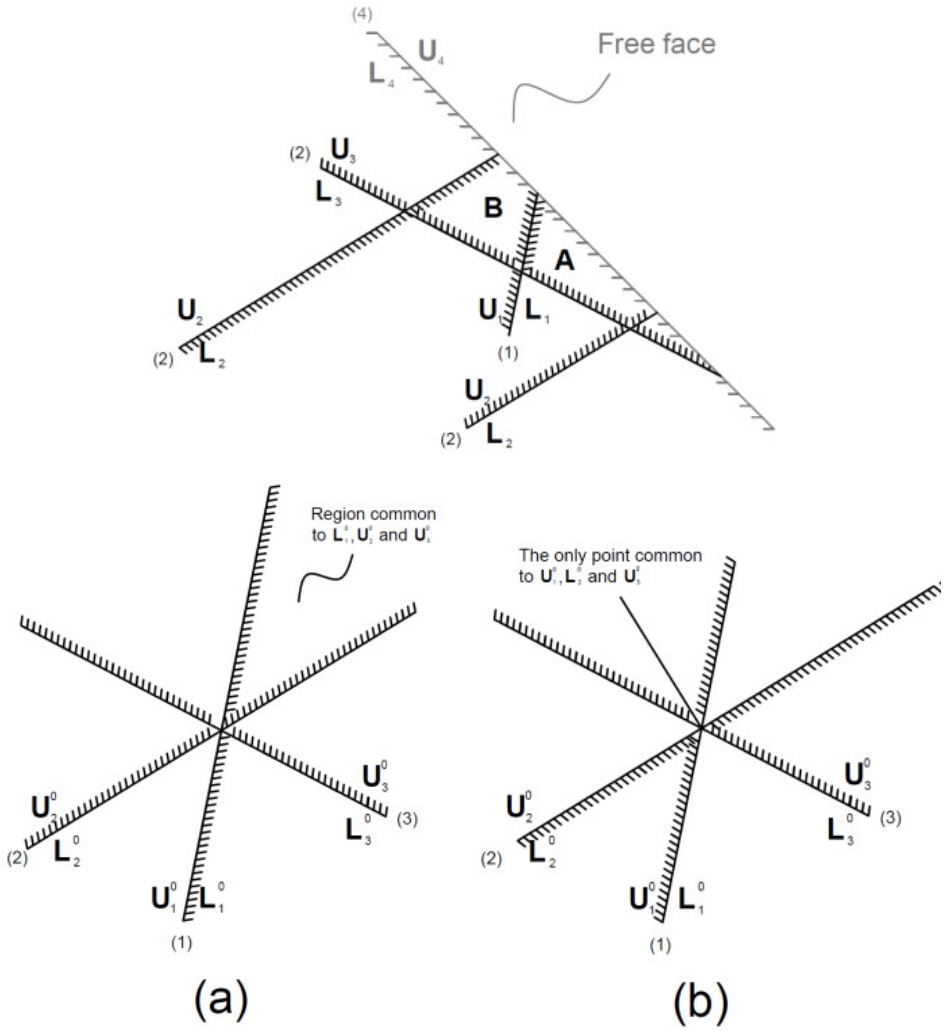

Figure 3.9 – Block removability in 2D – based on Goodman and Shi (1985)

Again the theorem is applicable on stereographic projections. Lines and planes can be represented in the stereographic projection but not points, except those that happen to lie over the reference circle (Goodman and Shi, 1985). A finite block is

non-removable if its JP is empty; an empty joint pyramid is one that has no edges. If it lacks an edge, it cannot be represented on the stereographic projection. Therefore, the regions absent from the stereographic projection are the JP's corresponding to finite blocks. When these blocks are cut by a free face, the resulting block will be tapered and therefore non-removable from the rock mass (Goodman and Shi, 1985).

3.2.6 Kinematics and stability of removable blocks

Until now methods to establish the finiteness and removability of blocks have been presented. In order to establish priority to blocks that will not be stable unless support is provided kinematics and stability must be analysed. Blocks of types I (Key block), II (potential key block) and III (stable block) are the ones addressed here. To distinguish stable blocks from potential key blocks a kinematic analysis where the direction of the resultant force is known or assumed is enough. A sliding equilibrium analysis is necessary to distinguish potential from real key blocks.

3.2.6.1 System of forces and equilibrium condition of a block

Figure 3.10 presents the system of forces acting on a block. There are three force components acting:

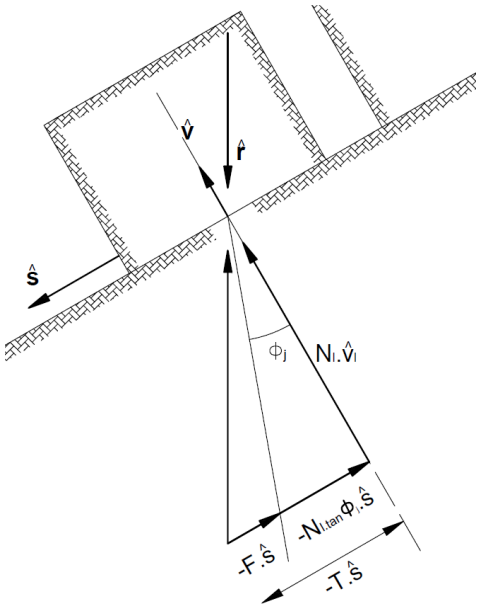

Figure 3.10 – System of forces acting on a block – adapted from Goodman and Shi (1985)

1. The resultant N of the normal reactions on the sliding planes. The normal reactions are (Goodman and Shi, 1985):

$$N = \sum_{l} N_l . \hat{v}_l \qquad \textbf{Eq. 3.5}$$

where $\hat{v}_l$ is a unit vector normal to joint plane l, directed into the block. No tensile strength is considered across the joint plane, therefore, $N_l \geq 0$.

2. The resultant T of the tangential forces acting on the sliding direction. Since no tensile strength is assumed across the joint, this resultant will be a frictional force (estimated with the Mohr-Coulomb strength model) plus a ficticious force, $-F\hat{s}$, which is added to bring the block to limiting equilibrium (Goodman and Shi, 1985). F is the magnitude of the force and $\hat{s}$ the unit vector that indicates the sliding direction. When F is positive, the block tends to slide unless artificial support is added. A negative value of F implies that the block is safe from sliding. The resultant of the tangential forces is (Goodman and Shi, 1985):

$$T = \sum_{l} N_l . tan\varphi_l + F \qquad \textbf{Eq. 3.6}$$

3. The active resultant force r, which includes all other forces acting upon the block, including for example weight, seepage forces or external water pressure (Goodman and Shi, 1985).

The equilibrium condition for a potential or real key block, ignoring rotation and assuming motion without acceleration (limiting equilibrium), is (Goodman and Shi, 1985):

$$r + \sum_{l} N_l \hat{v}_l - T\hat{s} = 0 \qquad \textbf{Eq. 3.7}$$

with $T > 0$ and $N_l \geq 0$. A consequence of the theorem of removability is that the sliding direction $\hat{s}$ of the removable block belongs to the JP of the block, that is (Goodman and Shi, 1985):

$$\hat{s} \subset JP \quad \textbf{Eq. 3.8}$$

3.2.6.2 Modes of sliding

Relationships have been established to connect the direction of sliding with the direction of the resultant force on an incipiently sliding block. Together with kinematics and a specific direction of the resultant force these rules permit the establishment of the sliding mode, if any, applicable to each JP (Goodman and Shi, 1985).

Lifting

Lifting is a failure mode in which all block faces will open. Since there are no face contacts, no normal reactions will be available ($N_l = 0$), and the sliding direction $\hat{s}$ cannot be contained in any joint plane (Goodman and Shi, 1985). The equilibrium condition in this case is:

$$r = T\hat{s} \quad \textbf{Eq. 3.9}$$

for a key block or potential key block, $T \geq 0$. Therefore, the sliding direction will be the same as the resultant direction (Goodman and Shi, 1985):

$$\hat{s} = \hat{r} \quad \textbf{Eq. 3.10}$$

For lifting the sliding direction $\hat{s}$ must be contained inside the JP but not in its boundary (Goodman and Shi, 1985).

Single plane sliding

In this failure mode the block slides along one of its faces. The sliding direction $\hat{s}$ is the orthographic projection of r on plane i, the sliding plane; and it is only parallel to the sliding plane (Goodman and Shi, 1985).

$$\hat{s} = \hat{s}_i \quad \textbf{Eq. 3.11}$$

Where

$$\hat{s}_i = \frac{(\hat{n}_i \times r) \times \hat{n}_i}{|\hat{n}_i \times r|} \quad \textbf{Eq. 3.12}$$

and $\hat{n}_i$ is the upward normal vector to plane *i*. In this case all joint planes except plane i will open and the sliding direction will belong to the intersection of the JP with plane i ($\hat{s} \in JP \cap P_i$) (Goodman and Shi, 1985)

Wedge sliding

This is the case where a block slides along the edge defined by two planes, P_i and P_j. Sliding will occur along the line of intersection in the direction which makes an acute angle with the direction of the active resultant r (Goodman and Shi, 1985).

$$\hat{s} = \hat{s}_{ij} = \frac{\hat{n}_i \times \hat{n}_j}{|\hat{n}_i \times \hat{n}_j|} sign\left((\hat{n}_i \times \hat{n}_j) \cdot r\right) \quad \textbf{Eq. 3.13}$$

The sliding belongs to the sliding edge, mathematically $\hat{s} \in JP \cap P_i \cap P_j$.(Goodman and Shi, 1985).

3.2.6.3 Kinematic conditions for lifting and sliding

Kinematic conditions necessary to identify the JP corresponding to a given sliding direction are presented in this section. This procedure allows a “mode analysis”, which determines the JPs corresponding to every sliding direction (Goodman and Shi, 1985). For a removable block, it follows that (Goodman and Shi, 1985):

$$\hat{s} \in JP \quad \textbf{Eq. 3.14}$$

Lifting. For lifting $\hat{s}$ is not parallel to any plane P_l. Defining $\hat{v}_l$ as the normal directed into the block, for each plane l of the block (Goodman and Shi, 1985):

$$\hat{s} \cdot \hat{v}_l > 0 \quad \textbf{Eq. 3.15}$$

Single plane sliding. For a block to slide along a plane P_i, the sliding direction $\hat{s}$ must be parallel to P_i (Goodman and Shi, 1985). Then:

$$\hat{s} \cdot \hat{v}_l > 0, for\ all\ l, l \neq i \quad \textbf{Eq. 3.16}$$

and

$$r \cdot \hat{v}_i \leq 0 \quad \textbf{Eq. 3.17}$$

Wedge sliding. For sliding along the intersection between planes i and j, the sliding direction $\hat{s}$ must be parallel to both planes i and j (Goodman and Shi, 1985). Then:

$$\hat{s} \cdot \hat{v}_l > 0, for\ all\ l, l \neq i\ or\ j \quad \textbf{Eq. 3.18}$$

$$\hat{s}_i \cdot \hat{v}_j \leq 0 \quad \textbf{Eq. 3.19}$$

$$\hat{s}_j \cdot \hat{v}_i \leq 0 \quad \textbf{Eq. 3.20}$$

where $\hat{s}_i$ and $\hat{s}_j$ are the orthographic projections of r on planes P_i and P_j, respectively.

3.2.6.4 Factor of safety

The differentiation between potential and real key blocks can be made using the safety factor of an incipiently sliding block. The factor of safety of a rock block is defined as (Hoek and Bray, 1981):

$$FS = \frac{resisting\ forces\ (R)}{driving\ forces\ (D)} \quad \textbf{Eq. 3.21}$$

Using the presented equilibrium equations it is possible to calculate the resisting and driving forces acting upon a rock block and consequently its factor of safety. In terms of factor of safety, key blocks are defined as blocks that possess a safety factor lower than 1. Development and proof of these equations will not be presented here and can be seen in the work of Goodman and Shi (1985).

Resisting forces

The resisting forces in the case of rock blocks are frictional forces, as already mentioned, and will be estimated in this work using the strength model of Mohr-Coulomb without consideration of cohesion, such that:

$$R = \sum_{l} N_l . tan\varphi_l \qquad \textbf{Eq. 3.22}$$

Lifting

In the case of lifting, there are no normal forces acting upon any of the JP planes. The resisting forces system can be written as:

$$R = 0 \qquad \textbf{Eq. 3.23}$$

Single plane sliding

For plane sliding, just one plane, P_i, will maintain contact and the force system is (Goodman and Shi, 1985):

$$R = N_i . tan\phi_i \qquad \textbf{Eq. 3.24}$$

Where:

$$N_i = |\hat{n}_i \cdot r| \qquad \textbf{Eq. 3.25}$$

For the special case where gravity acts alone upon the block the equation yields (Goodman and Shi, 1985):

$$R = W . \cos\alpha_i . tan\phi_i \qquad \textbf{Eq. 3.26}$$

Where α_i is the dip of plane P_i, and W the weight of the block.

Wedge sliding

In this case sliding occurs along the intersection of planes P_i and P_j, and all the other planes will open ($N_l = 0, for\ l \neq i\ or\ j$). The force system may be written as (Goodman and Shi, 1985):

$$R = N_i tan\phi_i + N_j tan\phi_j \quad \textbf{Eq. 3.27}$$

with $N_i \geq 0$, $N_j \geq 0$. Where:

$$N_i = \frac{\left|\left(r \times \hat{n}_j\right) \cdot \left(\hat{n}_i \times \hat{n}_j\right)\right|}{\left|\hat{n}_i \times \hat{n}_j\right|^2} \quad \textbf{Eq. 3.28}$$

$$N_j = \frac{\left|\left(r \times \hat{n}_i\right) \cdot \left(\hat{n}_i \times \hat{n}_j\right)\right|}{\left|\hat{n}_i \times \hat{n}_j\right|^2} \quad \textbf{Eq. 3.29}$$

Driving forces

The driving forces are defined as the component of the active resultant force, r, in the sliding direction (Goodman and Shi, 1985:

$$D = r \cdot \hat{s} \quad \textbf{Eq. 3.30}$$

Lifting

For lifting the equation may be rewritten as $D = |r|$, since the sliding direction is the same as the direction of the active resultant (Goodman and Shi, 1985).

Single plane sliding

In the case of sliding in a single plane, P_i, Eq. 3.30 can be developed and the driving force is (Goodman and Shi, 1985):

$$D = |\hat{n}_i \times r| \quad \textbf{Eq. 3.31}$$

If gravity acts alone upon the block, the equation yields (Goodman and Shi, 1985):

$$D = W.\sin\alpha_i \quad \textbf{Eq. 3.32}$$

Wedge sliding

Eq. 3.30 can also be developed for the case of wedge sliding along the intersection line of planes P_i and P_j, and yields (Goodman and Shi, 1985):

$$D = \frac{\left|r \cdot \left(\hat{n}_i \times \hat{n}_j\right)\right|}{\left|\hat{n}_i \times \hat{n}_j\right|} \quad \textbf{Eq. 3.33}$$

3.2.7 Probabilistic approach

A probabilistic analysis is a systematic procedure to examine the effect of the variability of each parameter on slope stability (Wyllie and Mah, 2004). By the random generation of the analysis parameters following a given probability distribution function (PDF), the safety factors of several blocks can be evaluated and probabilistically presented as a probability of failure, which represents the probability at which a block may fail. In this matter the method depends on the ability to accurately model the probability distribution of the design parameters (Wyllie and Mah, 2004). For this Master Thesis the Monte Carlo technique has been chosen, and the probabilities of failure are calculated using the software *Swedge and RocPlane (RocScience).* The Monte Carlo technique is an iterative procedure that can be summarized in four steps as presented by Wyllie and Mah (2004), Figure 3.11:

1. Estimate probability distributions for each of the variable input parameters,
2. Generate random values for each parameter,
3. Calculate the values of the driving and resisting forces and determine if the resisting force is greater than the driving force (if FS>1),
4. Repeat the process N times (N>100) and determine the probability of failure P_f from the ratio:

$$P_f = \frac{N - M}{N} = \frac{N_f}{N_T} \quad \textbf{Eq. 3.34}$$

where M is the number of times the resisting force exceeded the driving force (FS>1) (Wyllie and Mah, 2004).

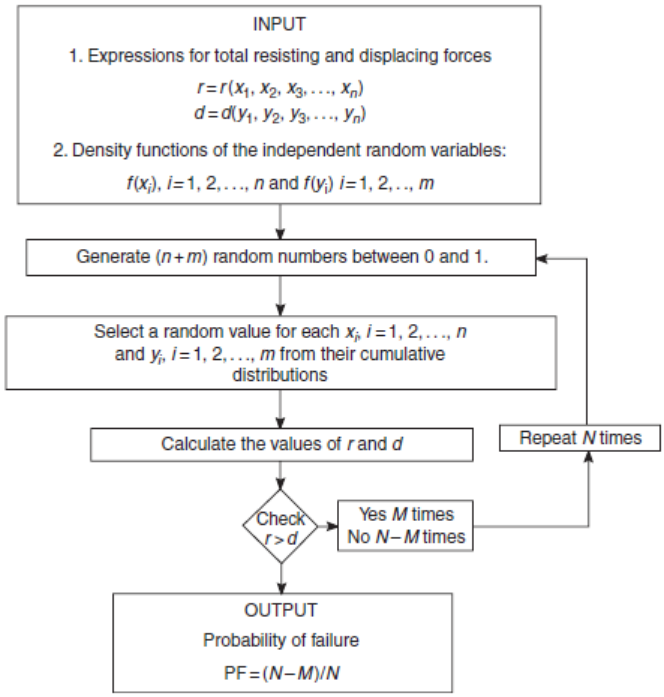

Figure 3.11 – Flow chart for Monte Carlo simulation to calculate probability of failure of a slope (Athanasiou-Grivas (1980), extracted from Wyllie and Mah (2004))

The probability of failure may be redefined as the product of the probability of kinematic (P_{km}) and kinetic (P_{kn}) instabilities according to Park (2005) and Einstein (1996), so that:

$$P_f = P_{km} \times P_{kn} \qquad \textbf{Eq. 3.35}$$

Where:

$$P_{km} = \frac{N_m}{N_T} \qquad \textbf{Eq. 3.36}$$

$$P_{kn} = \frac{N_f}{N_m} \qquad \textbf{Eq. 3.37}$$

N_m is defined as the number of iterations that create a kinematically admissible block (removable), N_f is the number of failed blocks, and N_T the total number of iterations. The advantage of this method is the separation of two distinct phenomena: removability and statics. Failure of a block may be more closely understood, and the controlling factor easily identified. This method will be well discussed in Chapter 7, where the stability analyses are carried out using this philosophy.

3.3 Software

3.3.1 Sphaira and Fracman

The orientation data was statistically treated using the software Sphaira and Fracman. The software Sphaira assumes, for a set of orientation data, a circular Fisher distribution. The parameters calculated are the centre of gravity of the measurements for a given confidence limit, the cone of confidence, spherical aperture, and the Fisher constant k. The cone of confidence defines a region in which the true vector of gravity is located with a probability given by the confidence limit, and the spherical aperture defines a region in which 68% of data are scattered, quantifying the spread of orientations around the mean value. The confidence limit used in this Master Thesis is 99%. The software Fracman has been used to draw the probability contours and rose diagrams.

3.3.2 ShapeMetrix^{3D}

ShapeMetrix^{3D} (3G Software & Measurement) is a photogrammetric software used to measure geological/geotechnical parameters of rock and terrain surfaces from 3D metric images. The software uses a stereoscopic image pair to construct a 3D model, as illustrated in Figure 3.12. The image stereopairs of the outcrops analysed in this work were acquired using a calibrated digital camera. From the stereoscopic image pair a three-dimensional image was computed using the software SMX Reconstructor. To scale the 3D-model a range pole with known distance between targets has been placed in front of the analysed outcrop. The model must be referenced, which was accomplished by measuring the azimuth of two targets placed within the range of overlapping of the photos. The analyses have been performed using the software JMX Analyst. In this work the software was used for orientation, spacing and persistence measurements.

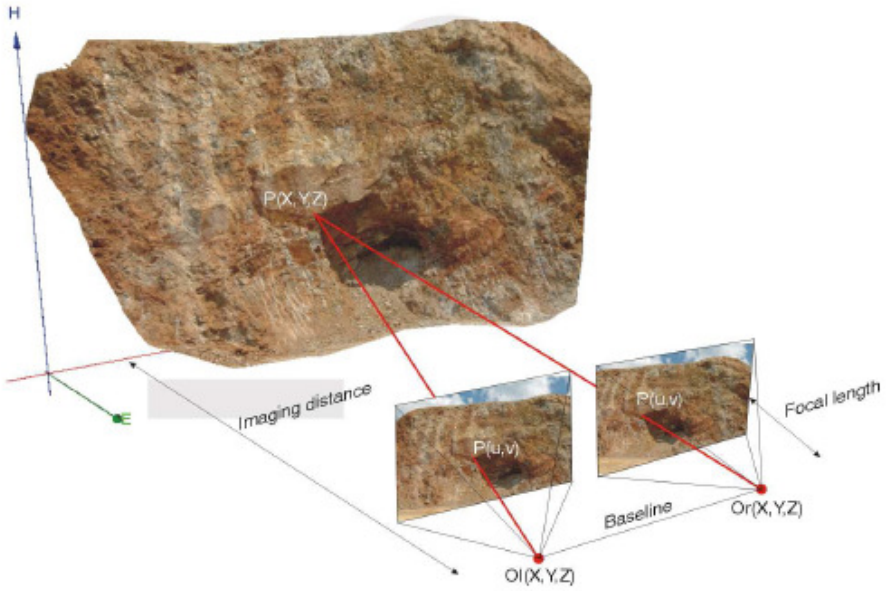

Figure 3.12 - Principle of the three-dimensional surface measurement. The three-dimensional point P(x,y,z) is reconstructed based on the intersection of two image rays (red), which go from the origins, O_l (left) and O_r (right), through a common point P(u,v). The procedure is repeated for a dense grid and a 3D model is formed from this point cloud. The base line and the camera standpoints do not have to be surveyed (3G, 2011).

3.3.3 RisCAN PRO

The site around the Ricobayo plunge pool was also scanned with a RIEGL 3D laser scanner during the field campaign in February 2011. Using the software RisCAN PRO a triangulated 3D model of the site was developed based on the point cloud obtained from the laser scanner. Orthogonal images of the 3D model were used for the development of maps for presentation and extraction of relevant information. The 3D model was generated as a false color elevation model; this procedure enables the presentation of elevation data also in 2D maps.

3.3.4 ArcMap

ArcMap (ESRI) is a GIS (Geographic information system) based software used for the acquisition, processing, organization, analysis, and presentation of geographic data. The maps for this Master Thesis have been developed, georeferenced and analyzed in this GIS environment.

3.3.5 Swedge and RocPlane

Swedge and RocPlane (RocScience) are two types of software which permit quick and interactive evaluation of stability of sliding wedges and planes, respectively. The software is programmed using concepts of block theory and is suitable for deterministic and also probabilistic analysis (RocScience, 2011).

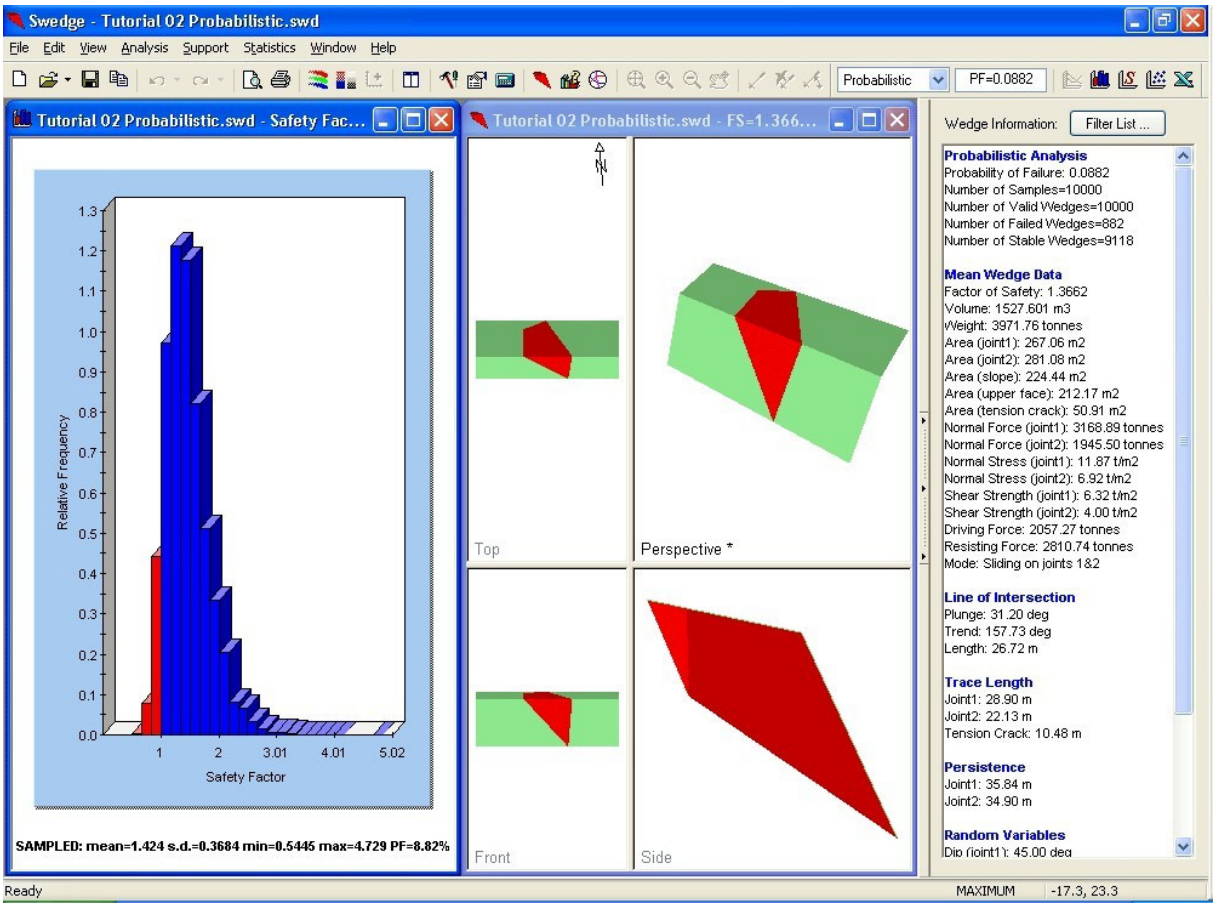

Figure 3.13 – Swedge probabilistic analysis (RocScience, 2012)

4 The Ricobayo Dam

The Ricobayo dam is located in the province of Castilla y León in northwestern Spain at the Esla River, a tributary of the Duero River. The geographic location is depicted in Figure 4.1, and the general characteristics of the dam are summarized in Table 4.1.

Reservoir :	Capacity	1200 hm^3
	Surface Area	58,55 km^2
	Normal operating level	684 m
	Probable maximum flood level	684,60 m
Drainage basin:		16023 km^2
Dam:	Crown length	270 m
	Crown elevation	685 m
	Height	99 m
Spilling capacity:	Surface spillway	4650 m^3/s
	Tunnel	874 m^3/s
Power generation:		
Ricobayo I:	Installed capacity	133 MW
	Mean energy production	637,30 GWh/yr.
	Max. flow	240 m^3/s
Ricobayo II:	Installed capacity	150 MW
	Mean energy production	264 GWh/yr. *
	Max. flow	210 m^3/s
Mean annual precipitation		771 mm
Q_{500}	500-yr flood event	6800 m^3/s

* Design value

Table 4.1 – General characteristics of Ricobayo Dam – Iberdrola S.A.

Construction of the dam started in 1929 and was completed in 1933. After completion of the dam, construction of the power house commenced. Power plant operation started two years later, in 1935. In Figure 4.2 the general project layout is depicted. The overall system includes a gravity dam (1), an integrated powerhouse (2) at the dam toe, and an independent surface spillway (3) along the left abutment (Guía Técnica, 1997).

Figure 4.1 – Geographic location of the Ricobayo Dam

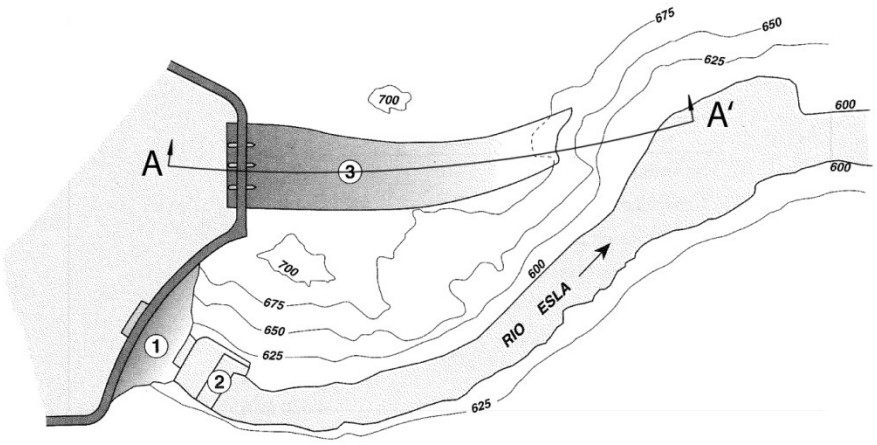

Figure 4.2 – General plan, 1933 (Guía Técnica, 1997).

4.1 Original spillway description

The spillway was designed as a long channel, intended to conduct the spilling flow in an optimal direction back to the river; minimizing back water effect which could cause loss of hydraulic height and eventual flooding at the power house (Del Aguila, 1933). The flow regime in the spillway channel has been studied by Del Aguila (1933). These model studies for the floodgate outlet indicated a flow regime which could vary from sub-critical, with fully open gates, to super-critical in case of partial opening. No detailed information about the real flow velocities over the spillway during the 1930's has been found. According to the Guía Técnica de Seguridad de Presas (1997), the flow velocities in the spilling channel were relatively low.

As illustrated in Figure 4.3, the original spillway structure was composed of a conducting platform, excavated directly in natural terrain at elevation 670m; a flood gate (1), comprising four gates 20,80m wide x 10,60m high, separated by concrete pillars of 3m width; and a spilling channel (2) excavated directly in rock, with over 400 m length. The water flow was conducted from the spilling channel back to the river over the natural slope at the end of the channel (Guía Técnica, 1997).

The performance of the spillway and initial scour was apparently influenced by the flow regime of the Esla River, construction and the rock mass conditions present in situ.

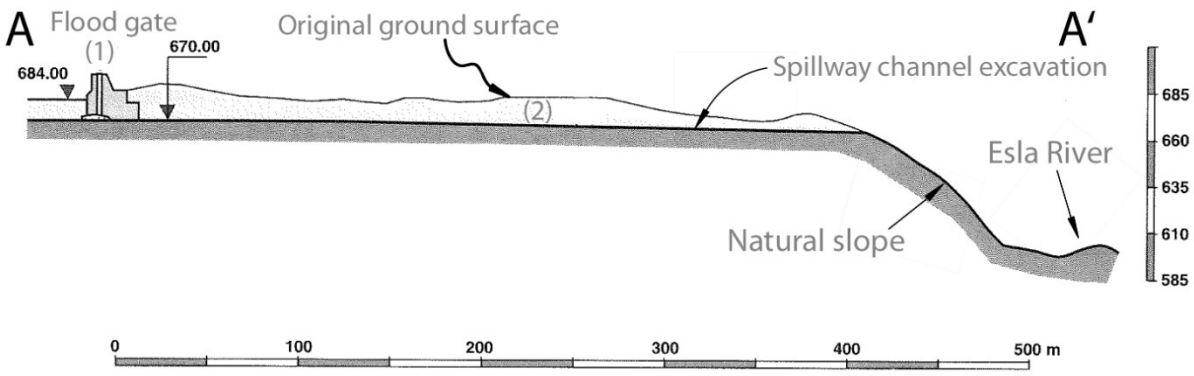

Figure 4.3 - Longitudinal profile A-A' of the original spillway (Guía Técnica, 1997)

The Esla River flow regime is extremely irregular (Figure 4.4); the peak flows are generally produced at the end of winter, coinciding with heavy rainfalls and snow melting at the river basin. The ratio between the 500 year flow (6800m³/s) and the average flow (144m³/s) is over 47 (Guía Técnica, 1997). In dry periods the flow reaches 5m³/s. Another factor that strongly restrained operation and may have affected the initial scour evolution, was the dam construction. It was realized leaving out a central gap, which was closed in 1933. After that, the reservoir was filled and construction of the power house started. The excess flow was thus directed entirely to the spillway. Operation of the spillway was planned if necessary, what occurred at the end of the same year (1933) (Guía Técnica, 1997).

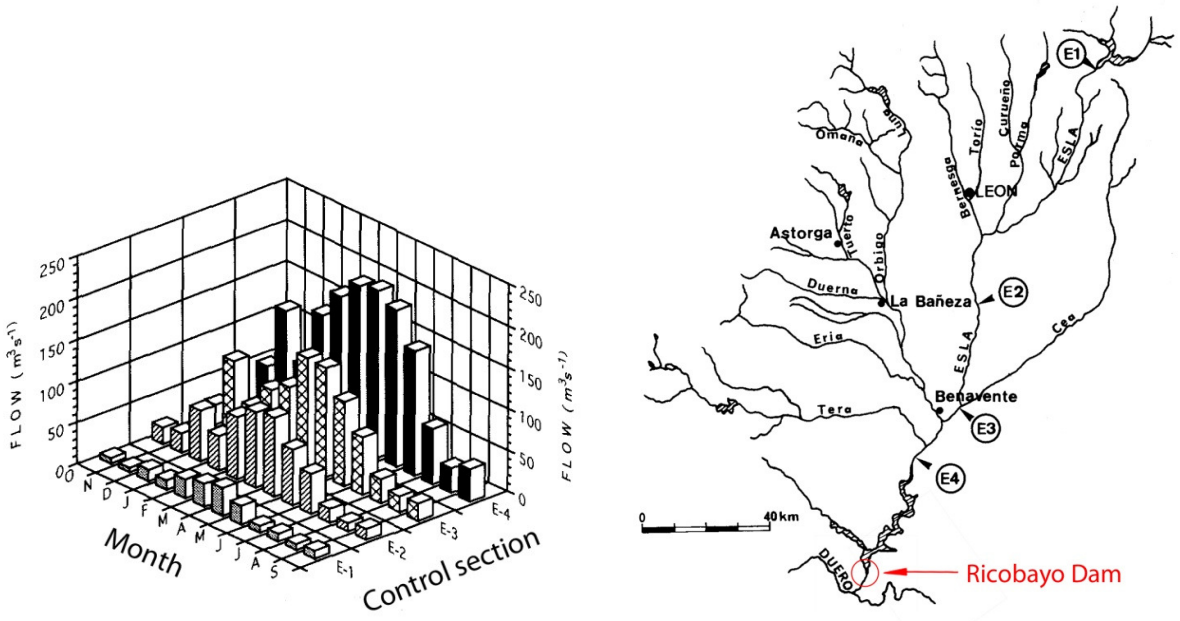

Figure 4.4 – Esla River flow regime – mean flow (1980-1989) at control sections E1-4 (Fernández-Aláez et al.,1992)

Rock mass conditions and its relation to scour are the main theme of this work and will be discussed in the following chapters. Undoubtedly, the rock mass was not as resistant to erosion as assumed in the original design.

4.2 Scour events 1934-1939

From the end of December 1933, when it was put into operation, to June 1934 the spillway was constantly in use. Initially a flow of about 100m³/s was measured (Guía Técnica, 1997). Figure 4.5 illustrates the first days of operation. Scour process can already be observed, indicated by deposition of eroded material at the toe of the slope. The initial formation of the gorge at the final section of the channel is also shown.

Figure 4.5 – Initial spillway operation (27/12/1933), and after first phase of the second erosion period (23/01/1934) – Iberdrola S. A.

In January of 1934 the first large scour event took place (scour event 1, SE1), modifying the frontal slope (Guía Técnica, 1997 and Iberduero S.A.). Gorge excavation may be observed in Figure 4.5. The water flow over this period did not exceed 1200 m³/s (Guía Técnica, 1997). According to documented observations, the erosion process did not occur continuously but rather in a periodic character: very

concentrated at time, and followed by periods of relative stability (Guía Técnica, 1997).

The water flow produces drag forces and pressure fluctuations within the discontinuities. These phenomena, along with the shear strength reduction in presence of water and erosion of the slope toe, may have triggered massive scour events.

The events of January were followed by a period of stability until the middle of March, when a renewed scour occurred (scour event 2, SE2) (Guía Técnica, 1997). Figures 4.6 and 4.7 show the development of scour event 2 (end of March 1934). The length of the head cutting is remarkable, with the knick point migrating about 150m toward the reservoir, and the spillway gorge deepened by 30-40m (Guía Técnica, 1997).

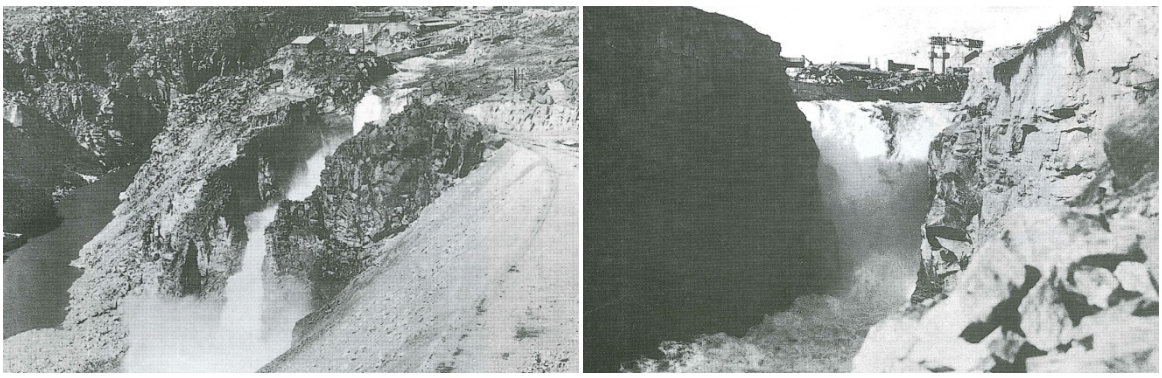

Figure 4.6 – Spillway situation during second scour event (21 and 23/03/1934) (Guía Técnica, 1997)

Figure 4.7 shows the poor stability of the gorge's right wall, and the first signs of instability underneath the concrete guide wall. It is also remarkable the water front position (head wall), compared to Figure 4.6. The photograph from 21/03/1934 shows the head wall position far away from the concrete guide wall, while in 26/03/1934 the head wall is already situated along the concrete guide wall.

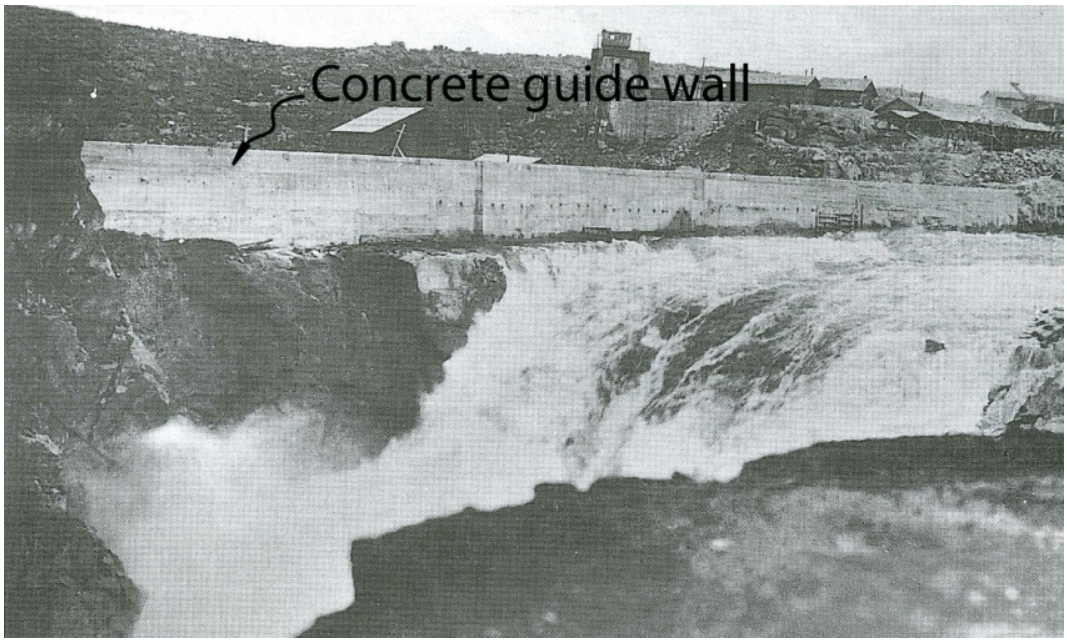

Figure 4.7 – Right wall situation in 26/03/1934 (Guía Técnica, 1997).

Spillway remediation works commenced in June of 1934 (Guía Técnica, 1997). The spillway condition can be observed in Figure 4.8. The remediation included (Guía Técnica, 1997):

- Protection of the spillway and head wall by concrete lining;
- Modification of the concrete guide wall by curving toward the interior of the channel. This was intended to keep the impinging jet as far as possible from the right wall of the gorge;
- Protection of the right wall of the gorge by concrete lining;
- Construction of a check dam at the spilling gorge, intended to elevate the water level within the gorge, creating a water cushion to dissipate hydraulic energy.

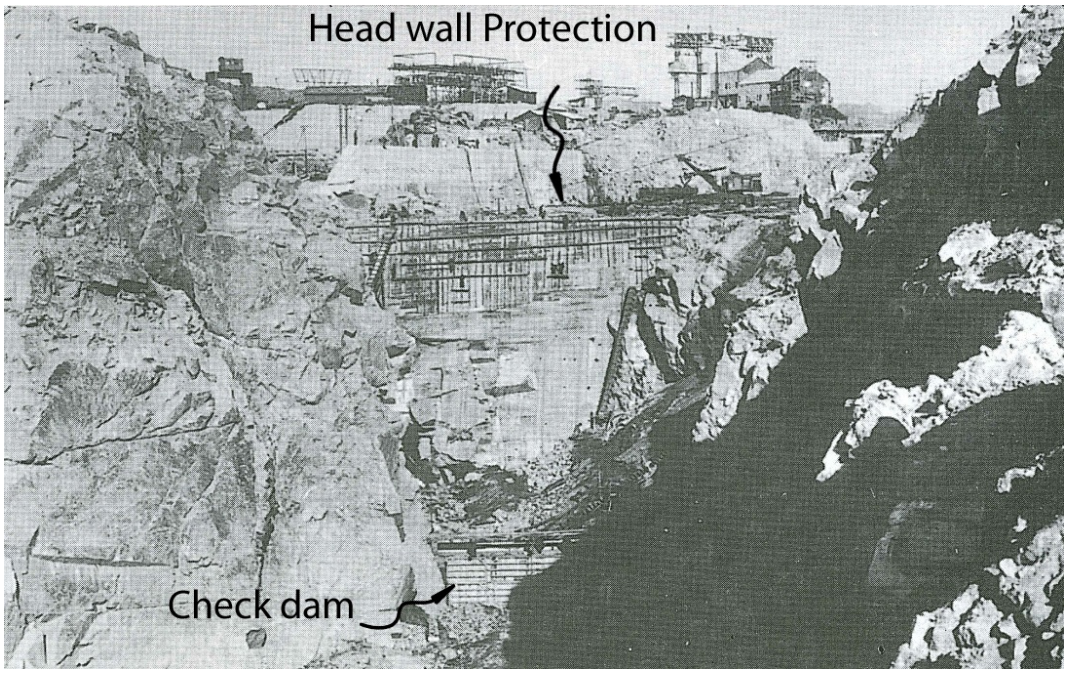

Figure 4.8 – Remediation works of 1934 (Guía Técnica, 1997)

Spillway flows started again at the end of 1934, and permanently continued until June of 1935 (Guía Técnica, 1997). Figure 4.9 depicts spillway conditions during this time period.

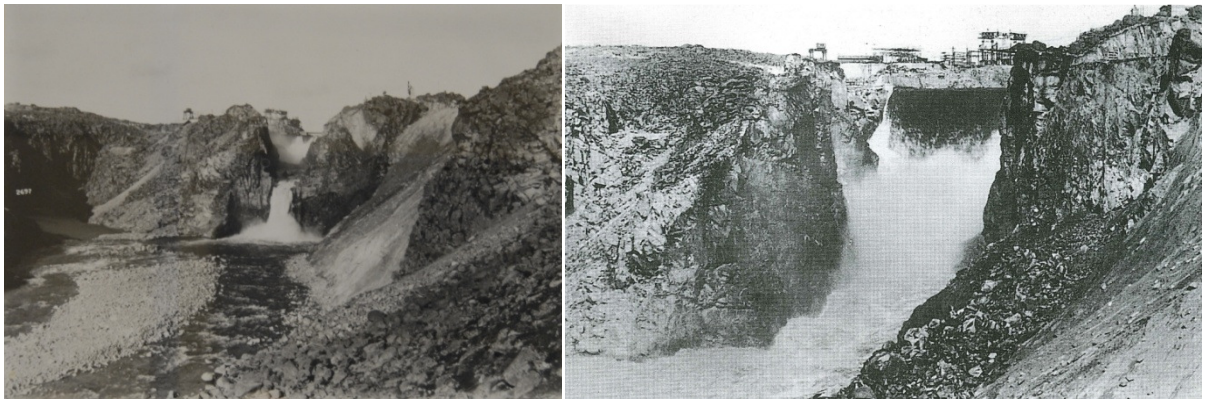

Figure 4.9 – Spilling gorge before (24/01/1935) and after third scour event (05/03/1935) (Guía Técnica, 1997)

In March of 1935 another scour event took place (scour event 3, SE3) (Guía Técnica, 1997). It started with the rupture of the check dam, with consequent loss of the water cushion. It affected mainly the right wall of the developing plunge pool and its depth, which increased from elevation 630m to 608m (Guía Técnica, 1997 and Iberduero S.A.). This situation is illustrated in Figure 4.9, wherein the magnitude of the erosion and its consequences may be observed. According to the Guía Técnica de

Seguridad de Presas (1997), the peak flow registered at the Bretó station upstream was about 1900m³/s on 02/03/1935. Annandale (2005) and a report from Iberduero S.A. mention a peak flow of 1000m³/s over the spillway.

During the summer of 1935, new remediation works were conducted, including (Guía Técnica, 1997):

- Modification of the impinging jet by cutting down the spillway outlet. The aim was to move the jet impact zone as far away as possible from the head wall;
- Construction of a gabion wall at the river channel to avoid deposition of eroded material at the main river bed; protecting the power house from back water effects.

Remediation works are illustrated in Figure 4.10.

Figure 4.10 – Detail of the spillway after first phase of the fourth scour event in 04/02/1936 (Iberdrola S.A.)

The remediation measures proved completely ineffective. In 1936, spillway flows caused new head cutting (Figure 4.11), completely destroying the head wall protection built in 1934, deepening and significantly enlarging the plunge pool (scour event 4, SE4). The gabion wall was completely buried as can be observed in the

Figure 4.12 (Guía Técnica, 1997). Annandale (2005) reports a peak flow of 1280 m^3/s and assesses the consequent bottom scour at 30m.

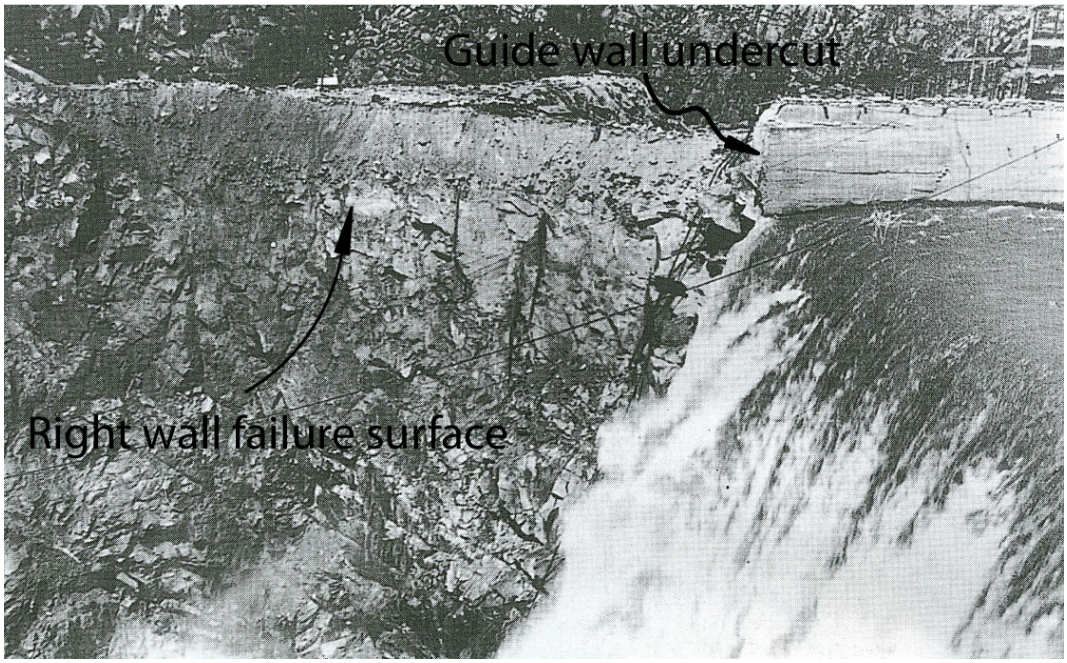

Figure 4.11 – Right wall in 28/04/1936 – (Guía Técnica, 1997)

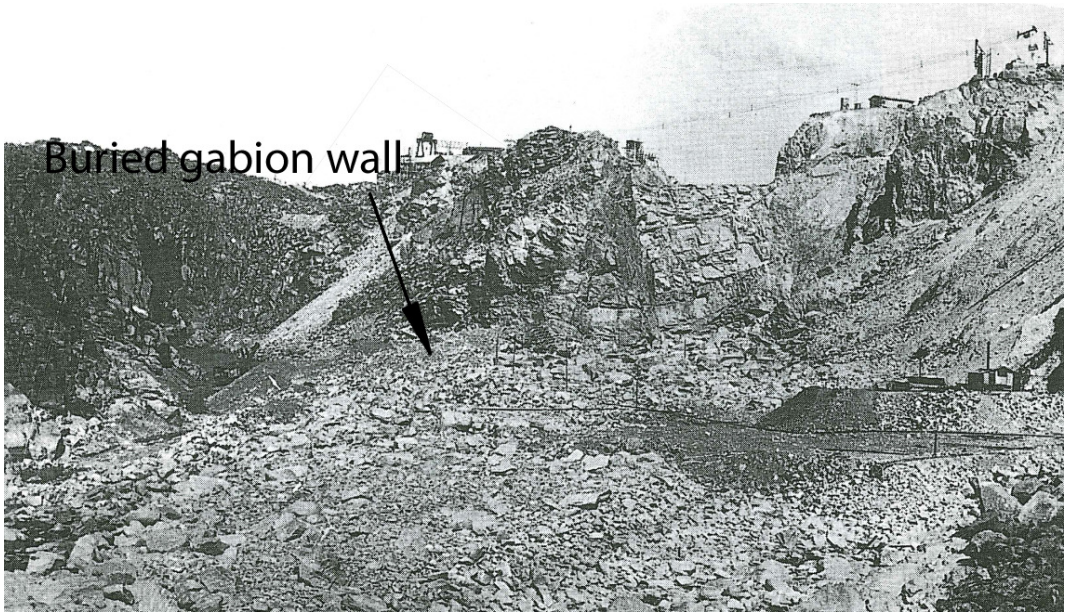

Figure 4.12 – Plunge pool situation in 21/10/1936 (Guía Técnica, 1997)

The power house operation, which began at the end of 1935, allowed (limited) regulation of the reservoir level, providing some ability to avoid spillway flows. Nonetheless, another head cutting event occurred in 1939 (scour event 5, SE5). This scour was not as intense as previous events, damaging mainly the spillway outlet.

Annandale (2005) reports a peak flow reaching 3230 m³/s. Figure 4.13 graphically summarizes the scour evolution from 1934 through January, 1939. No documentation of remediation measures between scour events 4 and 5 has been found.

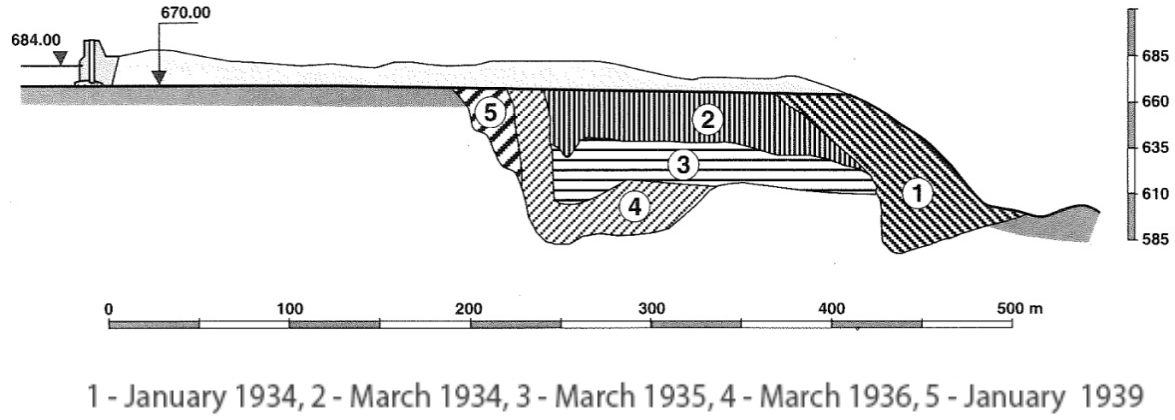

Figure 4.13 – Scour evolution, 1933 to 1939 (Guía Técnica, 1997)

4.3 Scour consequences

The scour consequences were not only adverse for the spillway structure, but also on power house operation (Guía Técnica, 1997).

Eroded material deposited in the main river channel caused a significant back water effect, causing difficulty to operate during flood periods. To minimize back water effects, a bypass tunnel and a defence dam were constructed, as depicted in Figure 4.14. The tunnel intake was built upstream of the eroded debris and the outlet more than a kilometre downstream. These measures minimized the back water and wave transmission upstream toward the power house (Guía Técnica, 1997).

A spilling tunnel, with a capacity of 874m³/s, was built along the left flank of the river to provide an alternate flow path during the final spillway remediation works. The tunnel was put into operation in January of 1939 (Guía Técnica, 1997).

4.4 Spillway remediation in the early 1940's

To finally control the spillway scour, a major reformulation of the spillway design was considered. From many options, a transformation of the scour hole into an

engineered plunge pool was chosen - taking advantage of the water volume inside to dissipate the energy of the falling jet (Guía Técnica, 1997).

This alternative did not require major earth work, but allowed an adaptation of the existing topography to the required modifications of the jet issuance, of the plunge pool (fit) and construction of the exit channel (Emissary) (Guía Técnica, 1997). The remediation works are illustrated in Figure 4.14, Figure 4.15 and Figure 4.16. The locations of the former check dam and gabion wall are depicted. The positions of the studied plunge pool walls are also indicated.

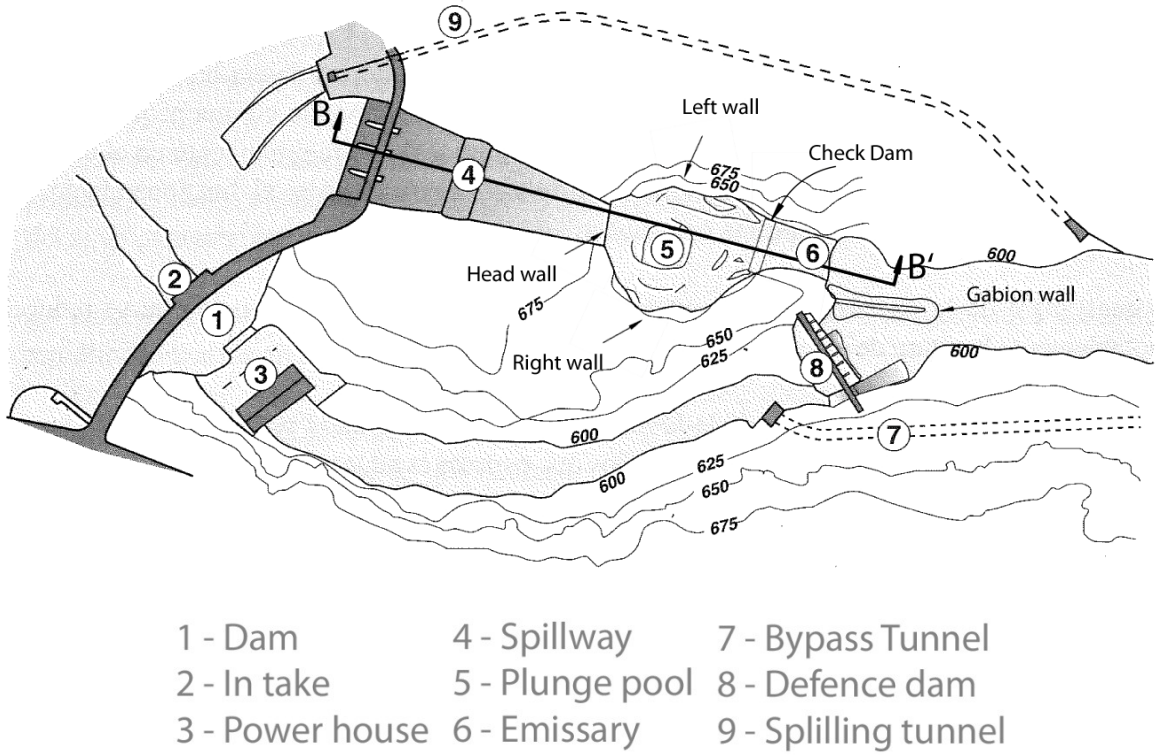

1 - Dam 4 - Spillway 7 - Bypass Tunnel
2 - In take 5 - Plunge pool 8 - Defence dam
3 - Power house 6 - Emissary 9 - Splilling tunnel

Figure 4.14 – Plan view of the plunge pool (Guía Técnica, 1997)

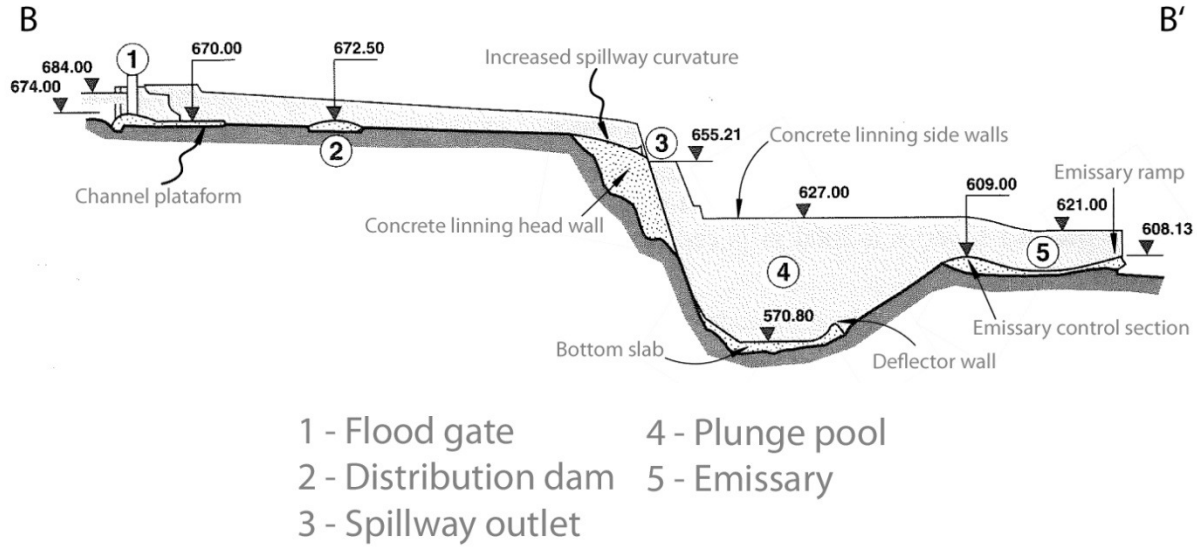

Figure 4.15 – Longitudinal profile B-B' of the plunge pool (Guía Técnica, 1997)

The details and functions of the remediation are summarized below (Guía Técnica, 1997):

- The initial 92m long section of the spillway has a flat bottom (level 670m), 4m lower than the closing level of the flood gate, ending on a 2.5 m high "bump", which forms a small distribution device. Its purpose is the distribution of the flow over the whole area of the channel, even if the flood gates operate asymmetrically;
- Downstream of this distribution dam supercritical flow is induced, reducing the water level and consequently the necessary height of the channel side walls;
- Aeration of the impinging jet is assured by air presence underneath the jet;
- The head and plunge pool side walls are protected by concrete lining, thicker at the head wall because of its irregularity and greater exposure to scour;
- Increased vertical curvature of the final section of the spillway, increasing the velocity, thus throwing the impinging jet away from the head wall. The bottom of the plunge pool is protected by a reinforced concrete slab of 0.8-1.5m thickness (reinforcement: ϕ32mm, at 25 cm centres);
- Protection of the head- and sidewalls by avoiding direct impact of high velocity flows originating from the impact of the jet in the plunge pool. This was achieved by deflector walls built at the bottom slab, which reorient and conduct the flow to the exit channel (Emissary);
- A control section is established at the entrance of the emissary; inducing supercritical flow within, reducing water level and consequently the side wall

heights of the Emissary. The Emissary channel ends in a ramp, directing the jet away from the toe of the structure.

- The rock mass was also anchored: the lower levels and bottom slab with injected passive anchors of 10,5m length with steel bars of ϕ40mm, and the higher levels with passive anchors of 5,5m length with steel bars of ϕ32mm.

Figure 4.16 shows the deflector walls and the emissary.

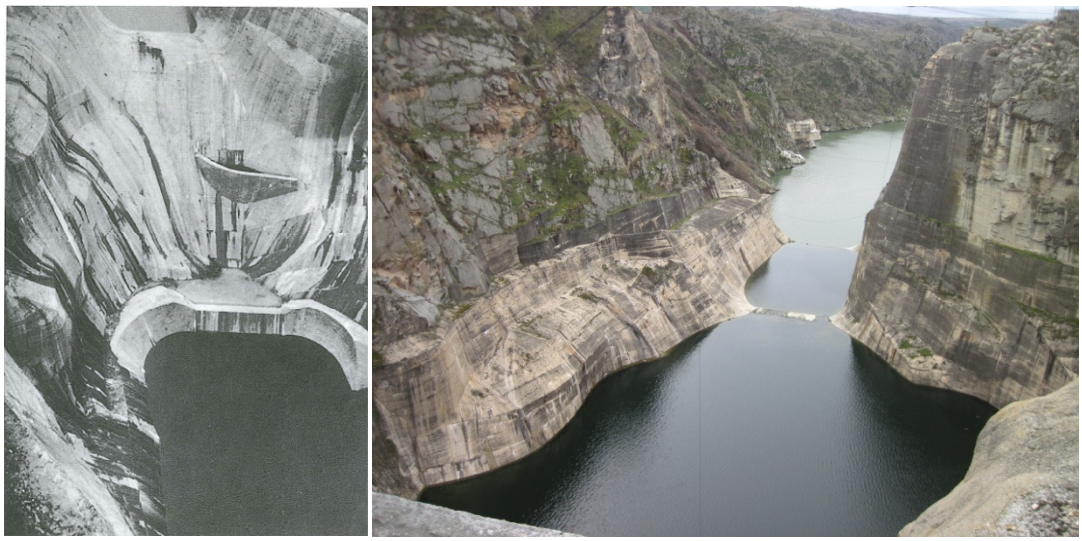

Figure 4.16 – Deflector walls and emissary (Guía Técnica, 1997)

4.5 Scour event of 1962 and modification of the spillway outlet

The plunge pool functioned satisfactorily until 1962. Inspections performed in 1953 and 1961 found signs of surface erosion of the concrete, presumably due to revolving blocks within the plunge pool, see Figure 4.17. The erosion exposed the reinforcement in some parts, mainly at the toe of the right wall, but no signs of failure were evident (Iberduero S.A., 1961).

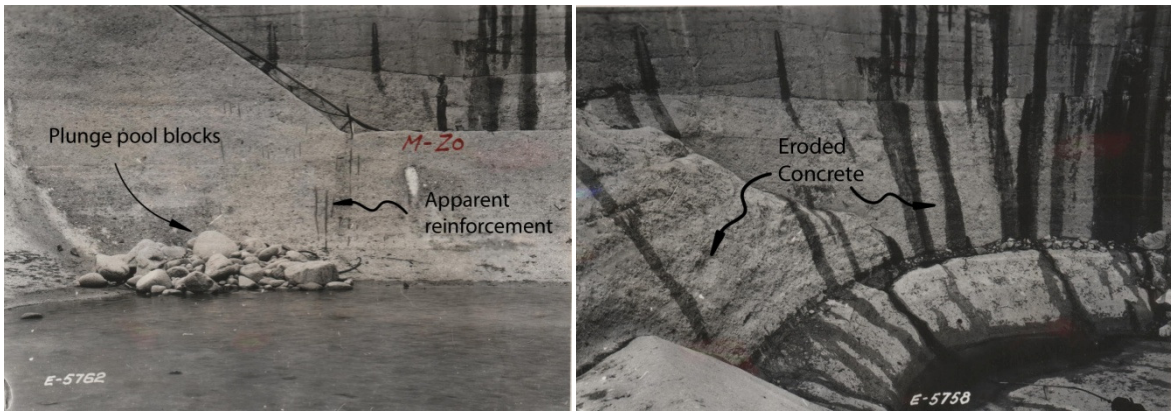

Figure 4.17 – Concrete erosion observed in 1961 (Iberduero S.A., 1961).

In 1962, an extraordinary spillway flow of about 5000 m^3/s occurred. After this event, inspections revealed that the plunge pool bottom slab had been completely uplifted, together with one side of the deflector walls (Guía Técnica, 1997).

The problem was studied in scaled hydraulic models, and was mitigated by the construction of flow splitters at the spillway outlet. The aim was to divide the jet, augment initial turbulence, improve aeration, and enlarge the impact zone. These factors increase the energy dissipation capacity and significantly diminish the pressures at the plunge pool bottom. The splitters were constructed in 1962. Since then, the spillway has performed well, even with flows of about 3000 m^3/s in some occasions, without any sign of further erosion.

Figure 4.18 – Splitters at the spillway outlet (Annandale, 2005)

5 Regional Geology

The Ricobayo dam, body and spillway, is founded over a granitic rock mass called the Ricobayo Massif. This Batholith is located close to the northern boundary of the Central Iberian zone of the Variscan Iberian Massif. The morphology is conditioned by NW-SE Variscan structures, especially the Villadepera antiform, the Alcañices synform, and a regional shear zone called the Villalcampo shear zone (Fernández-Turiel, 1990).

Composed basically of two-mica granitoid with variable facies, the Ricobayo Batholith also presents small dioritic bodies of which the largest is the Moveros, located NW of the massif (González Clavijo et al., 1991).

Studies of the metamorphic contact aureole show that intrusion occurred after the second phase of the Variscan deformation (González Clavijo et al., 1991). These granitoids are seen as syntectonic with the third phase of the Variscan Orogeny, which resulted in a generalized orientation of their minerals and shear structures (especially at the northern part) (Fernández-Turiel et al., 1990).

5.1 Geological setting

The Ricobayo Massif is an approximately 150 km² granitic intrusion that outcrops in the SW part of the Alcañices synform, which is a late Variscan structure located in the north-western Iberian Massif (González Clavijo and Catalán, 2002). This part of the Iberian Massif has been divided into four zones, according to geological characteristics (Figure 5.1): the parautochthonous Cantabrian (CZ), West Asturian-Leonese (WALZ) and Central Iberian (CIZ) zones; as well as the allochthonous Galicia-Trás-os-Montes (GTMZ) (Escuder Viruete, 1998).

During Variscan convergence, the evolution of the orogenic wedge, built by stack of these units, controlled the compressive deformation and its migration over the time from the innermost zones of the Central Iberian zone to the foreland of the Cantabrian zone. The suture is located in the western part of the belt, in the GTMZ, and is identified by the presence of ophiolitic rocks in the Cabo Ortegal, Ordenes, Bragança, and Morais complexes (Figure 5.1) (Escuder Viruete, 1998).

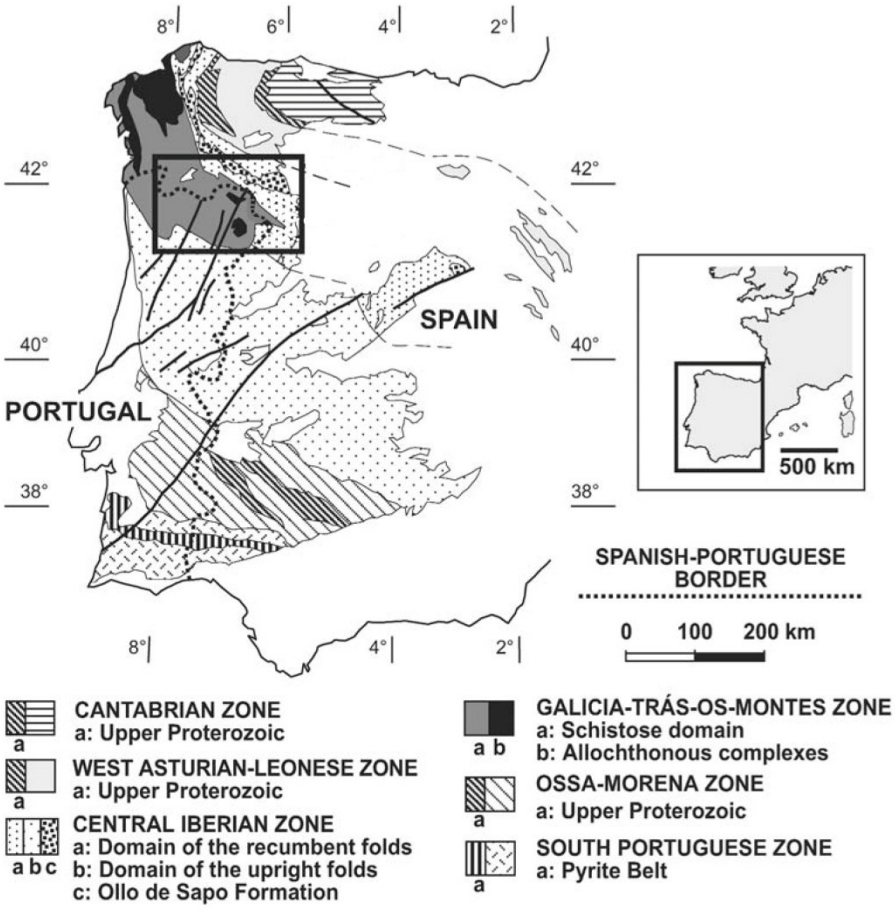

Figure 5.1 - Iberian Massif zones – (González Clavijo and Catalán, 2002).

The CIZ is part of the Iberian autochthon. Its stratigraphic sequences were deposited, in spite of recumbent folding and thrusting, over the same basement in which they are now. It is believed that the CIZ zone was situated at the northern passive margin of Gondwana, and most of its Paleozoic sedimentary sequences were deposited in this environment (González Clavijo and Catalán, 2002).

In Spain mostly metasedimentary rocks with subordinate volcanic rocks occur. In Portugal, a stack of allochthonous units is present including ophiolites and far-travelled terrains. The allochthonous units, such as Bragança and Morais, were thrust over the lower allochthon, a metasedimentary unit known as the schistose domain, and the parautochthon. The ensemble was subsequently placed onto the Paleozoic sedimentary cover of Gondwana (González Clavijo and Catalán, 2002).

Allochthonous complexes together with the lower allochthonous are encompassed by the GTMZ. The lower allochthon occurs below the suture marked by the ophiolites,

and is viewed as part of the Gondwana margin, but occupying a marginal position relative to that of the CIZ (González Clavijo and Catalán, 2002).

A thrust marks the limit between the CIZ and the GTMZ; it brought both zones into contact during the Variscan compression. This boundary is one of a complex of imbricate thrusts with varying displacements (González Clavijo and Catalán, 2002).

5.2 Stratigraphy

The region is characterized by a metasedimentary sequence ranging from late Vendian to Devonian ages. According to González Clavijo and Catalán (2002), the sequence may be divided into three main parts: (1) pre-Ordovician to earliest Ordovician, (2) Ordovician and (3) Silurian-Devonian.

- **Pre- Ordovician to lowermost Ordovician sequence (>488 Ma)**

This is the oldest stratigraphic sequence; it crops out in an antiformal structure (Villadepera Antiform) in the southern part of the area (Figure 5.2). The sequence is composed by two nonfossiliferous units, the Villalcampo Schists and the Villadepera Gneisses (González Clavijo and Catalán, 2002).

- **Ordovician sequence (488 – 433 Ma)**

This sequence consists of four different formations. The two lower formations (Santa Eufemia and Peña Gorda Formations) are characterized by quartzites, whereas the upper parts (Villaflor and Campillo Formations**)** are dominantly characterized by slates (González Clavijo and Catalán, 2002).

- **Silurian-Devonian sequence (433 – 359 Ma)**

Silurian and Devonian deposits occur mainly in allochthonous units (Figure 5.2). At the base of the Silurian succession, along its carbonaceous slates, an important decollement fault and several imbricates developed. This sequence is composed of four different formations. The Manzanal del Barco Formation is characterized by gray to black slates; the Almendra Formation is composed by rhythmic alternations of limestones and gray slates; the San Vitero Formation, which has a flysch character; and the Rábano Formation composed mainly of gray and greenish slates (Figure

5.2). A structural unit called Río Duero represents the autochthon, and has been described above (González Clavijo and Catalán, 2002).

5.3 Structural geology

No pre-Variscan structures have been mentioned in the literature other than an unconformity at the base of the Santa Eufemia Formation (Lower Ordovician) (Fernández-Turiel (1985) and González Clavijo and Catalán (2002)).

Variscan deformation in the area is characterized by internal deformation, metamorphism, and granitic intrusion. It is typical of an internal part of the orogen, but also depicts some structures typical of foreland thrust belts (González Clavijo and Catalán, 2002).

The area was affected basically by three deformation phases. First and second events (D_1 and D_2) produced recumbent folds and thrusts directed to the northeast. Associated deformation structures range from ductile to brittle. These sub-horizontal structures were subsequently affected by upright folds (D_3) and sub-vertical transcurrent ductile shear zones developed. This nomenclature is used to facilitate the correlation with other areas with the Iberian Massif (Escuder Viruete (1998), Fernández-Turiel (1985) and González Clavijo and Catalán (2002)).

5.3.1 Folds and faults

During the first deformation event (D_1), recumbent folds of several scales developed. They have an approximate N120°E attitude, sub-horizontal axis, and vergence to the northeast (Figure 5.2). An axial planar cleavage (S_1) is widely developed in the area. The intersection lineation between bedding and S_1 displays a northwest-southeast attitude, and is parallel to D_1 fold axes (axial-planar cleavage, dip 30°-60° to the SW) (Escuder Viruete (1998), Fernández-Turiel (1985) and González Clavijo and Catalán (2002)).

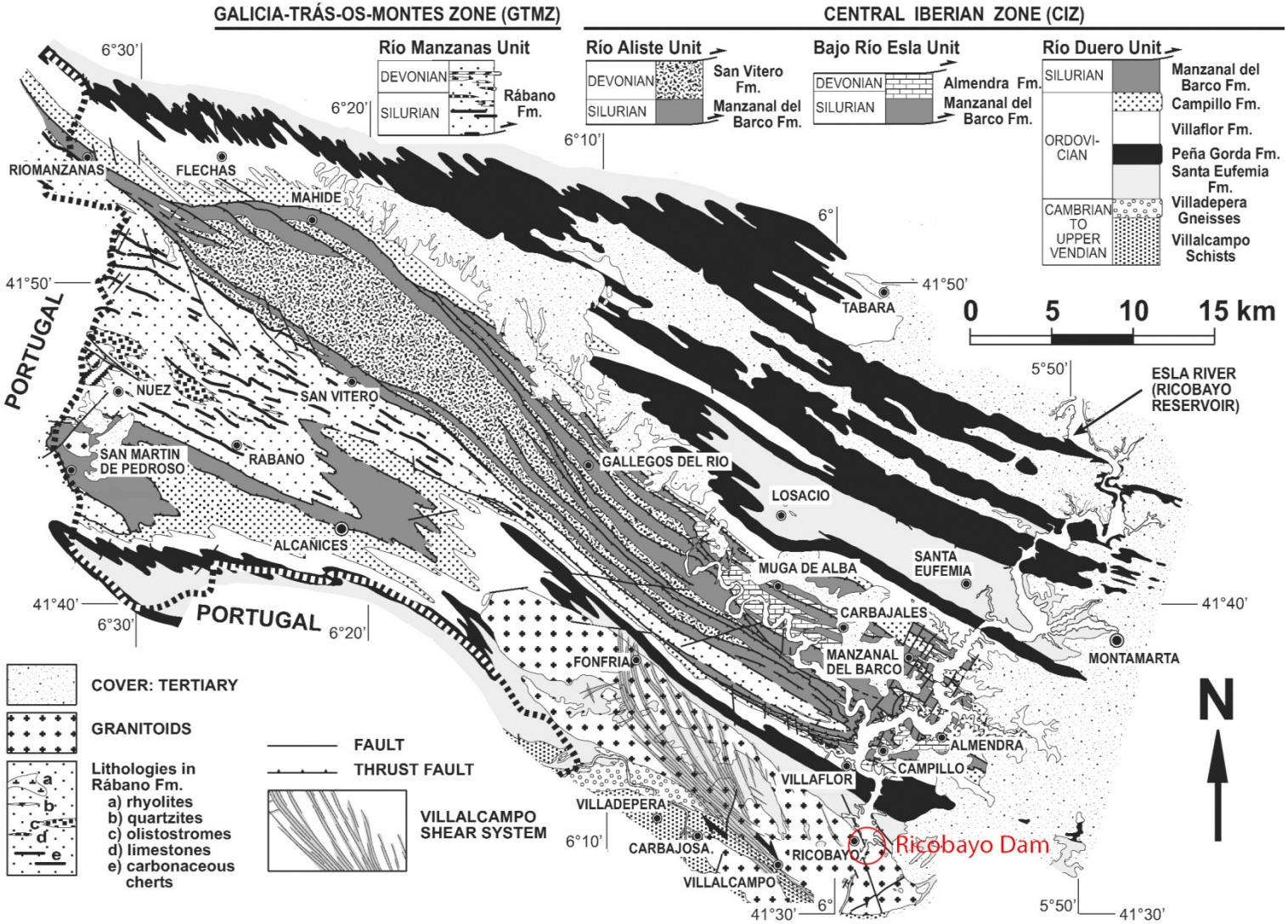

Figure 5.2 – Geological map of the area - González Clavijo and Catalán (2002).

Tectonic thrusting developed three main allochthonous sheets and numerous imbricates. These structures, common in north-western Iberia, have been ascribed to the second deformation phase (D_2). D_1 structures are to a large extent overprinted by D_2 fabrics and structures. Their importance for the emplacement of allochthonous complexes has been pointed out in the literature (Escuder Viruete (1998) and González Clavijo and Catalán (2002)).

Thrust deformation displaced only the Silurian and Devonian sequences; the others stayed as the autochthon. The main faults separate structural units (Figure 5.2), merging downward and dipping to the southwest into a floor thrust, which is actually a decollement developed at the base of the Manzanal del Barco and Rábano Formations (González Clavijo and Catalán, 2002).

The geometry of these imbricates suggest thrusting toward the northeast, which matches the asymmetry of D_1 folds and indicates a tectonic transport toward the external zones (CZ) during recumbent folding and thrusting (González Clavijo and Catalán, 2002).

Fault gouge with centimetre thickness is common at the thrust surfaces, but ductile shear bands also developed. These fault rocks have a strong S_2 tectonic foliation. Ductile fault rocks (phyllonites) are mainly developed at the basal decollement, depicting a stretching lineation (L_2) trending NW-SE in a sub-horizontal manner. These evidences suggest two distinct and near perpendicular directions of motion of the basal decollement: to the SE-directed mass transport, parallel D_1 and D_3 fold axes, and the NE-directed motion, normal to fold axes (Escuder Viruete (1998) and González Clavijo and Catalán (2002)).

Third Variscan deformation (D_3) produced open folds trending NW-SE. This deformation event rotated the limbs of D_1 folds to which they are homoaxial, and folded D_2 thrusts (Figure 5.2) (Escuder Viruete (1998) and González Clavijo and Catalán (2002)).

Folds are open to tight and define a set of NE-vergent antiforms and synforms, of which the largest is the Alcañices synform. An associated cleavage (S_3) developed axial planar to the folds. Its character varies according to the material affected. The prevailing type is a crenulation cleavage, developed more or less over the previous cleavages (Escuder Viruete (1998) and González Clavijo and Catalán (2002)).

Steeply dipping ductile shear bands also affect the area; the Villalcampo shear system. It is a sub-vertical dextral shear system with N130°E general trend. The Villalcampo shear system consists of several jointed shear bands more than 1 km wide in its central part. To the SE, it develops an extensional duplex, and to the NW it spreads out in a "horse tail" or fan, when reaching the plutonic rocks of Ricobayo, directions vary here from N130-170°E, see Figure 5.2 (González Clavijo et al. (1991) and González Clavijo and Catalán (2002)).

Shear zones are easily seen affecting the granitic massif, but may be also encountered in schists and gneisses. A variety of deformation structures were caused by shearing. The most common are type I S-C mylonitic deformation, but well foliated mylonites are also present. General movement of the main shear band is reported as sub-horizontal. Mylonitic lineation plunges over 10° just in the final parts of the "horse tail", where it reaches 24° SE. This behaviour is associated with extensional deformation within the fan, and may be explained as the formation of a negative flower structure. A dextral movement with relative active displacement of 3-4 km has been estimated, and the shear system is believed to be of late D_3 formation (González Clavijo et al. (1991) and González Clavijo and Catalán (2002)).

Conjugated second-order sinistral shear bands are found inside the "horse tail", and to its western part. They are sub-vertical, varying in trend from N70°-110°E. All the area west of the Esla River within the Ricobayo granite presents filled veins, mainly with quartz. They have been interpreted as extensional veins of the main shear system since they are mainly perpendicular to mylonitic foliation (González Clavijo et al. (1991) and González Clavijo and Catalán (2002)).

Late sub-vertical faults are also documented, the most important are either parallel to the main NW-SE structure or nearly normal to it (NE-SW). The latter group is

especially well developed around the Ricobayo Reservoir. These late faults exert important control on the present fluvial system (González Clavijo and Catalán, 2002).

According to Fernández-Turiel (1985), the granitic bodies may be divided in two structural domains, taking as reference the presented foliation. The domain with one foliation covers a larger area. It depicts a relative constant strike (N120°E); similar to the axial planes associated with the third phase of deformation (S_3), and the fold axes (D_3). The other domain presents two foliations. These rocks with S-C planes are concentrated within the northern part of the Ricobayo Batholith, and probably restricted to the Villalcampo shear zone. The S-planes are directed N120°E and are sub-vertical, coinciding with the previously described foliation. The C-planes are also sub-vertical, but directions vary between N130°-170°E. The average angle between them is about 20° and they tend to coincide when approaching shear bands (Fernández-Turiel, 1985).

5.4 Metamorphism and Plutonism

During the Variscan Orogeny, the area underwent regional metamorphism of intermediate pressure (M_1). M_1 is low grade (below biotite isograd) in most of the area, but reaches medium grade around the Villapera antiform. High-grade metasediments and anatexites were produced in a second regional metamorphic event (M_2). Granitic intrusions, most of them synkinematic to D_3, produced contact (thermal) metamorphism on their host rocks and imprinted also themselves by dynamic metamorphism related to transcurrent shearing (González Clavijo and Catalán, 2002).

Granitic intrusions are represented by two main bodies: the Ricobayo two-mica granitoid and the Carbajosa leucogranite (Figure 5.2). The Ricobayo Massif is larger. It is composed of a wide variety of facies: coarse and fine-grained two mica granitoid, biotitic granite with cordierite, leucogranite with garnet and sillimanite, and amphibole-bearing diorite. It is an elongated body trending NW-SE with roughly the same trend as D_3 folds, but overprints them. The Carbajosa leucogranite is smaller but presents the same elongated characteristic. These intrusions present a common aureole of thermal metamorphism (M_3) (González Clavijo and Catalán, 2002).

6 Rock mass characterization

The rock mass was characterized during a field campaign in February of 2011. The rock is composed of medium to coarse grained granitoid, with gray colour when fresh, and varying from light red to light brown when weathered. The rock mass is blocky to tabular, discontinuities are highly persistent and mostly planar with some roughness. Minor seepage is present at the surface, but no groundwater flows have been observed in existing underground excavations (tunnels).

6.1 Orientation and joint set determination

Based on field observations and statistical studies of the acquired data, five joint sets have been recognized. As observed in the field the most dominant sets are sub-vertical, and a gently dipping set striking roughly NE-SW.

Figure 6.1 – Granitoid rocks outcropping at Ricobayo Dam

The joint structure was mapped in the field with a geological compass and also with the photogrammetric software ShapeMetrix^{3D}. The results are presented in Figures 6.2 to 6.7, and Table 6.1 summarizes joint set orientation statistics.

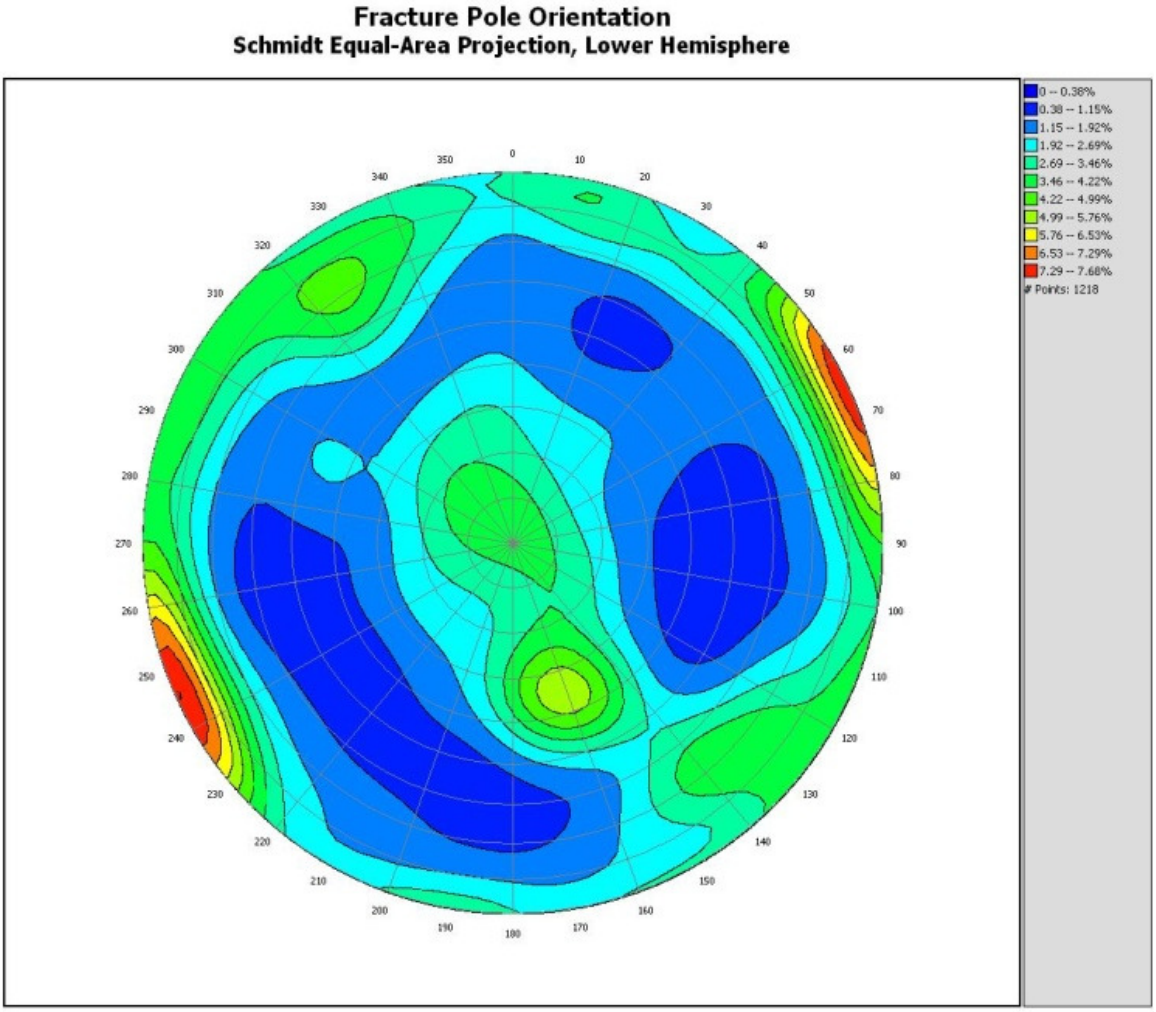

Figure 6.2 – Probability contours of all measured data (1218 measurements)

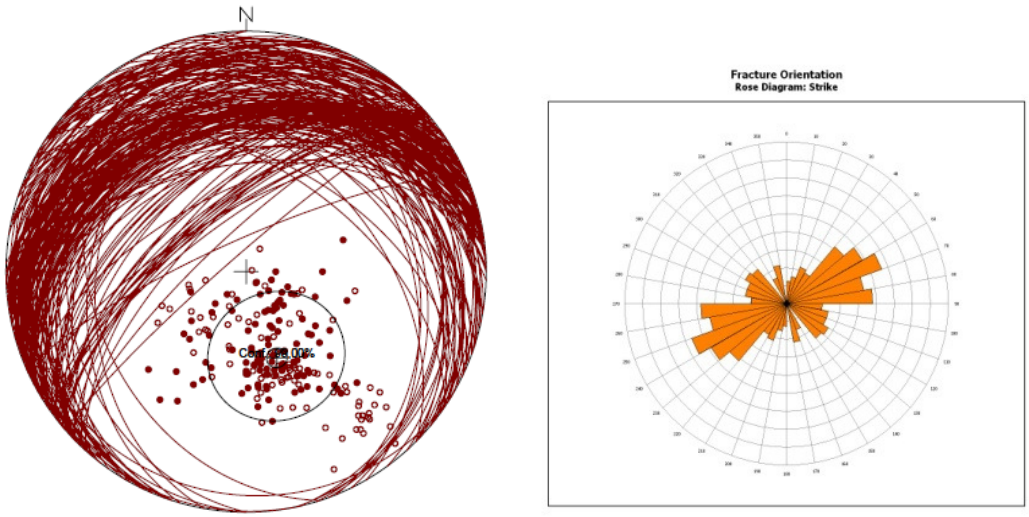

Figure 6.3 – Statistical analysis of structural orientation data – Joint set 1 (212 measurements)

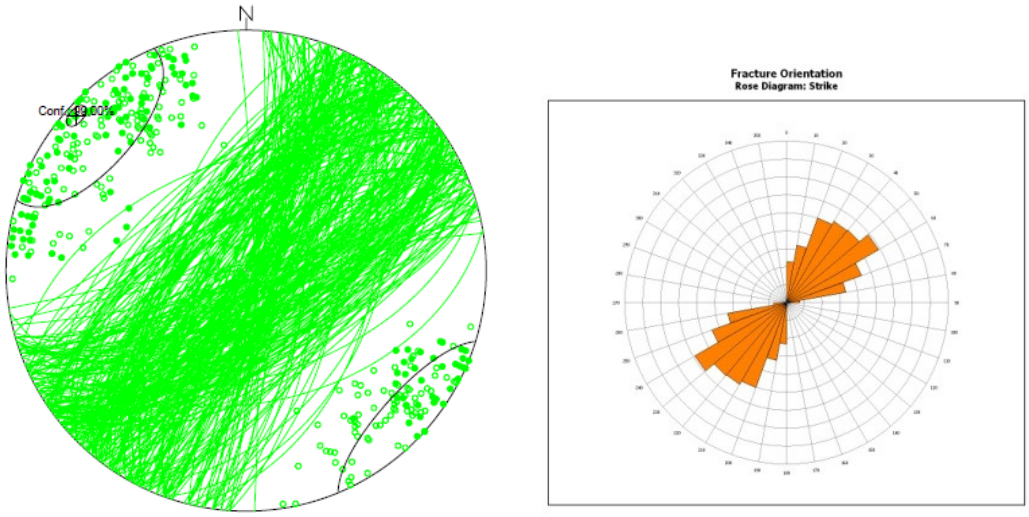

Figure 6.4 – Statistical analysis of structural orientation data – Joint set 2 (324 measurements)

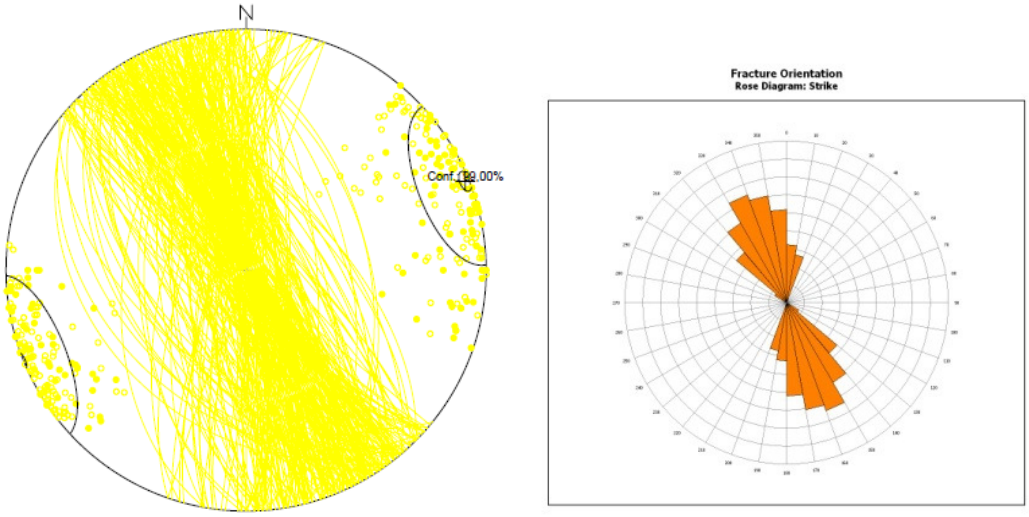

Figure 6.5 – Statistical analysis of structural orientation data – Joint set 3 (315 measurements)

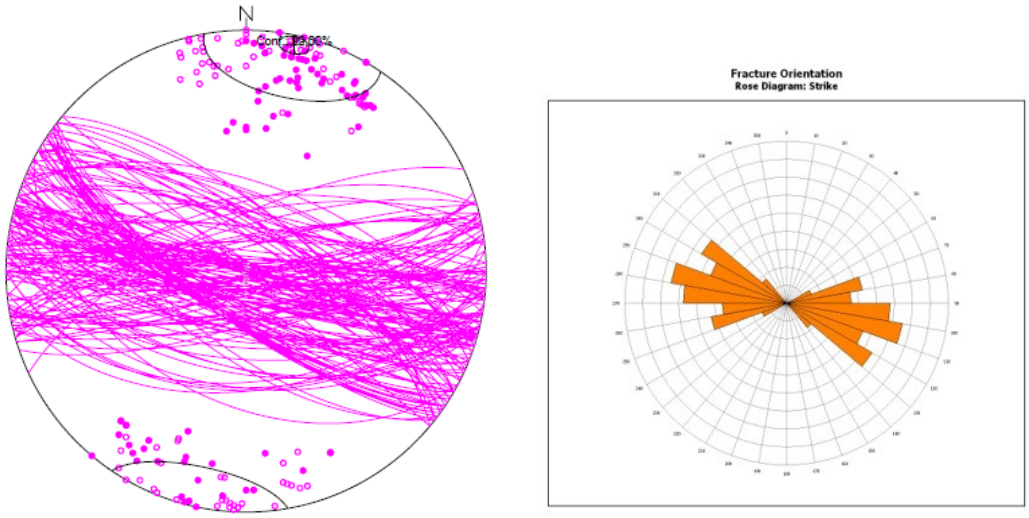

Figure 6.6 – Statistical analysis of structural orientation data – Joint set 4 (162 measurements)

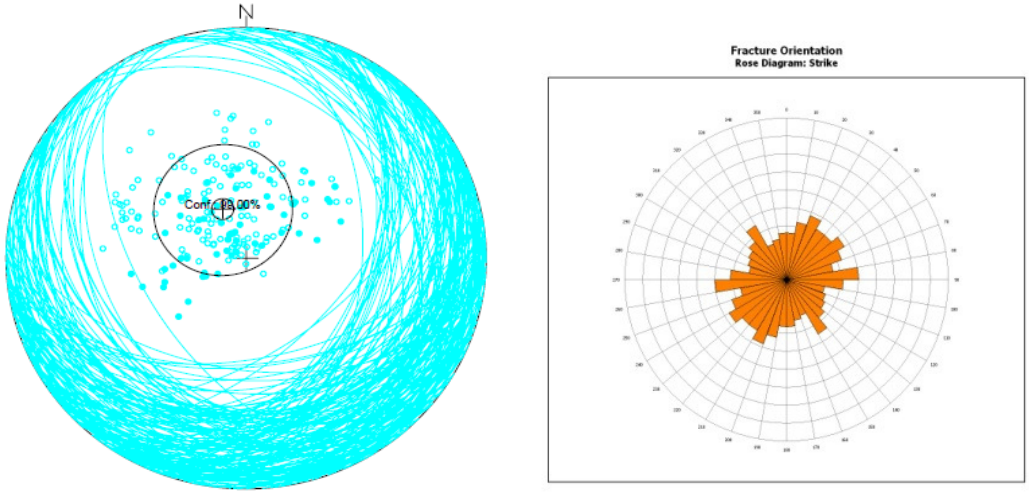

Figure 6.7 – Statistical analysis of structural orientation data – Joint set 5 (191 measurements)

Figure 6.8 presents the mapping results geographically. Based on this information the rock mass structure around the plunge pool is basically homogeneous. For this reason, the data was statistically evaluated as an entire data set.

Joint Set	Dip [°]	Dip direction [°]	Cone of confidence [°]	Spherical aperture [°]	Fisher parameter *k*	Number of measurements
J1	31	340	3	23	13,46	212
J2	85	132	3	26	10,66	324
J3	88	248	3	21	15,75	315
J4	85	192	4	22	13,59	162
J5	19	155	4	23	12,63	191

Table 6.1 – Summary of joint set statistics

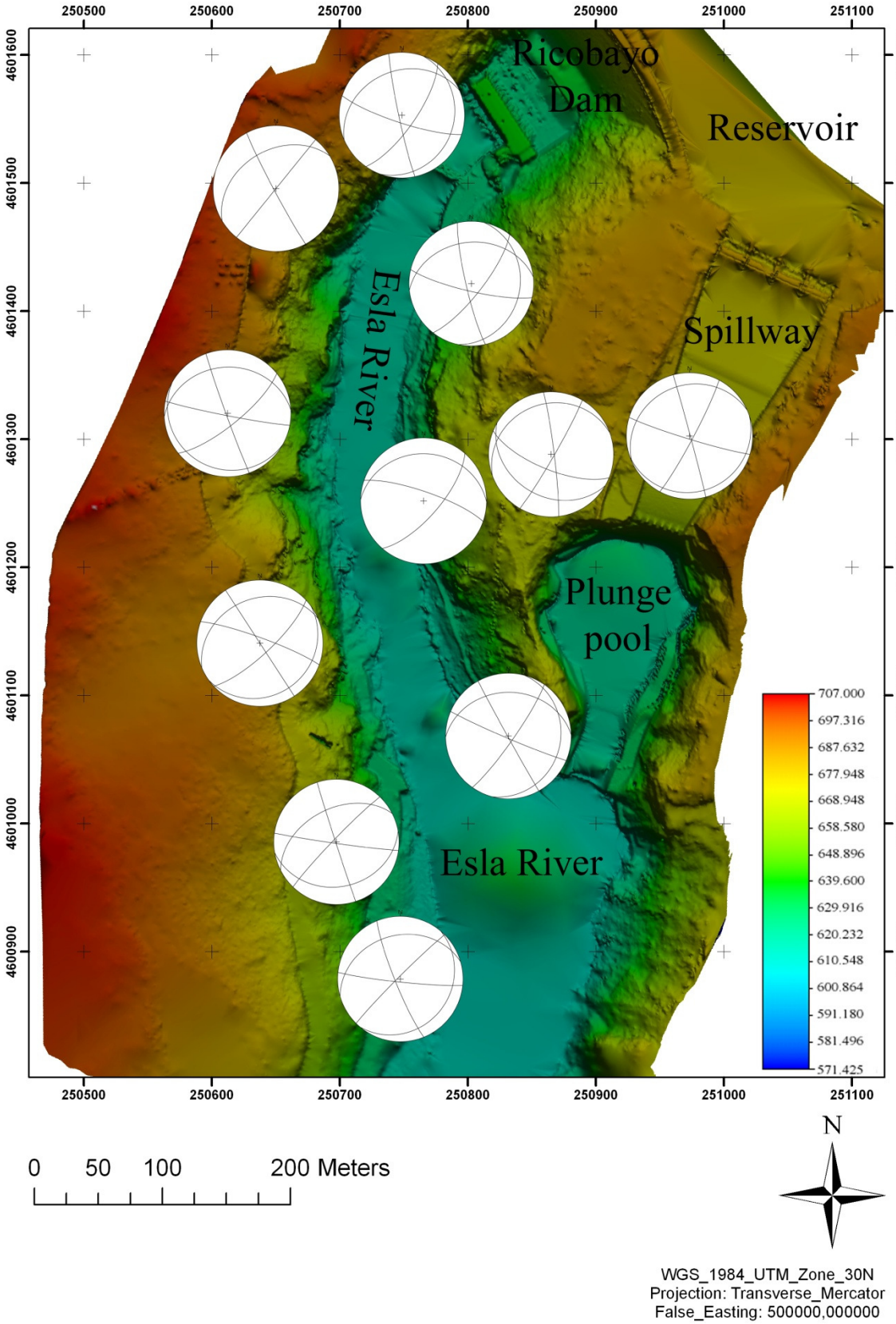

Figure 6.8 - Geographic distribution of joint orientation measurements (Base map: False colour elevation model and stereographic projections: LHRC)

6.2 Spacing

The spacing of adjacent discontinuities has been acquired in the field, as already mentioned, along a scanline and digitally using ShapeMetrix^{3D}. Average joint spacing may be described as wide (60-200cm) to very wide (200-600cm), with measurements concentrated in the wide interval. Statistical summary of spacing measurements performed is presented in Table 6.2.

Joint set	Spacing [m]					
	ShapeMetrix^{3D}			Scanline		
	Mean	Standard deviation	Number of measurements	Mean	Standard deviation	Number of measurements
J1	1,3	0,5	60	-	-	1
J2	1,3	0,8	62	0,7	0,4	11
J3	1,9	1,0	81	0,3	0,2	5
J4	1,2	0,5	37	0,7	0,5	8
J5	0,9	0,4	77	0,8	0,2	3

Table 6.2 – Statistical summary of joint spacing

6.3 Persistence

Trace length measurements have been performed along the scanline and with ShapeMetrix^{3D}, the statistical summary of the acquired data is presented in Table 6.3. Joint trace lengths are typically in the range of 1 to 3m and may be described according to ISRM (1981) as low persistent; nevertheless, joint planes are much more penetrative, as observed in the field. Trace length is highly influenced by the size of the planar exposure where persistence is acquired. Since quantitative measurements have been performed along a road cut with heights around 5m (exceptionally higher) results may be constrained. A qualitative description in larger exposures along the margins of the Esla River downstream of the dam led to persistence ranges from 10-20 meters (high persistence according to ISRM, 1981), and some traces of joint set 1 exhibit extremely high persistence exceeding 20 meters.

Joint set	Trace length [m]					
	ShapeMetrix^{3D}			Scanline		
	Mean	Standard deviation	Number of measurements	Mean	Standard deviation	Number of measurements
J1	1,7	1,0	60	-	-	1
J2	1,6	0,9	62	1,9	1,5	11
J3	2,1	1,4	81	2,3	1,5	5
J4	1,3	0,6	37	1,6	1,6	8
J5	1,9	0,7	77	2,8	1,9	3

Table 6.3 – Statistical summary of trace length

Joint termination type has been acquired along the scanline; the results without set discrimination are presented in Figure 6.9. The reported terminations are representative of the upper termination of the respective joint; the scanline was positioned close to the ground floor, so that no lower terminations could be observed. As suggested by ISRM (1981), the termination data is presented in the form of the termination index (T_r), for semi-trace evaluation the index is defined as (ISRM, 1981):

$$T_r = \frac{\Sigma R \ \times 100}{\Sigma R + \ \Sigma D + \ \Sigma X} \ [\%]$$

In this case, the termination data acquired yield a termination index of: $T_r = 10{,}7\%$

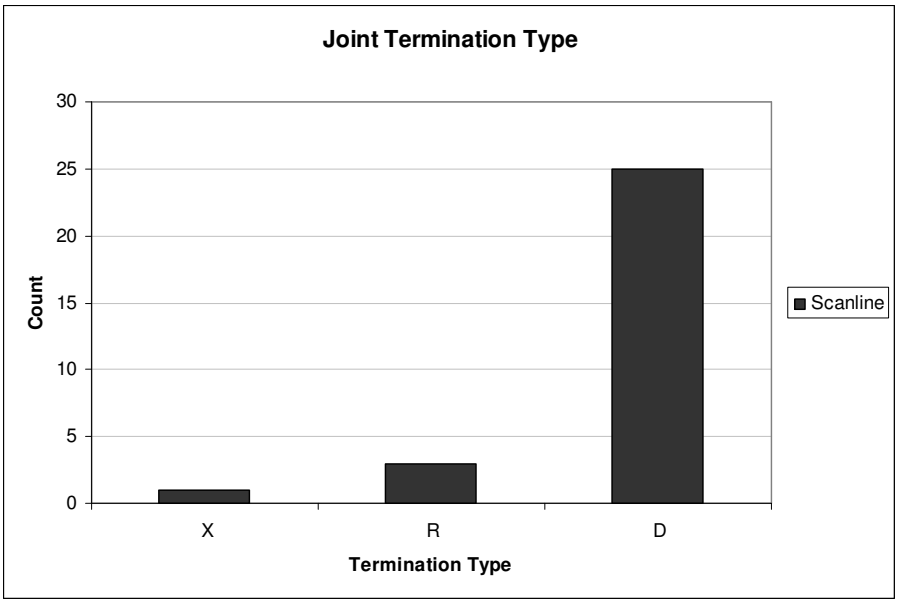

Figure 6.9 – Termination type of all measured data – X: Hidden, R: in intact rock and D: at another joint (28 measurements)

6.3.1 Lineament studies and Trace maps

To assist the study of joint persistence, two trace maps have been developed around the Ricobayo plunge pool. Figure 6.10 illustrates the location of the trace maps. The trace maps have been developed over freely taken photographs and possess just a relative scale. Nonetheless, this qualitative information supports the statement that discontinuity persistence is higher than measured in outcrops. The trace maps and the respective photographs are presented in Figures 6.11 and 6.12. As observed, joint traces are longer than 3 meters, ranging generally from medium (3-10m) to high (10-20m) persistence for all joint sets. In the case of joint set 1, higher persistence was observed and discontinuity traces are observed in map scale (1:1000). Analysis of topographic maps together with field observations led to the development of a map where large lineaments are documented. The map is presented in Figure 6.13, note that two features present characteristics of steep planes and are sub parallel to set 2.

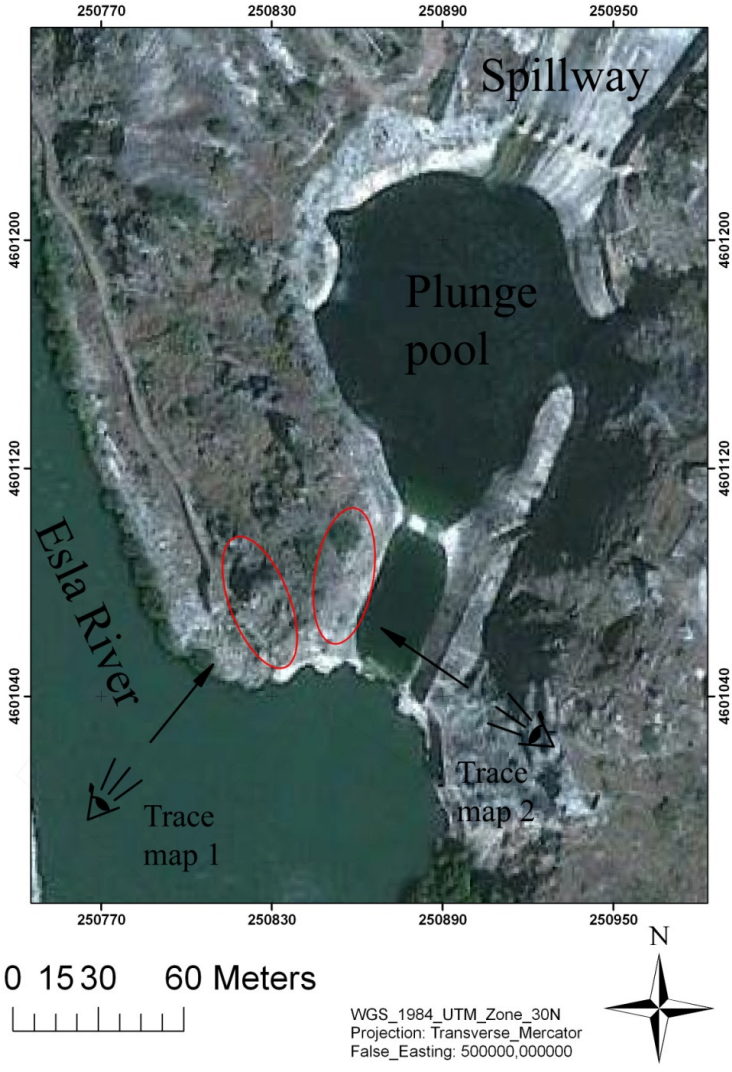

Figure 6.10 – Trace map locations

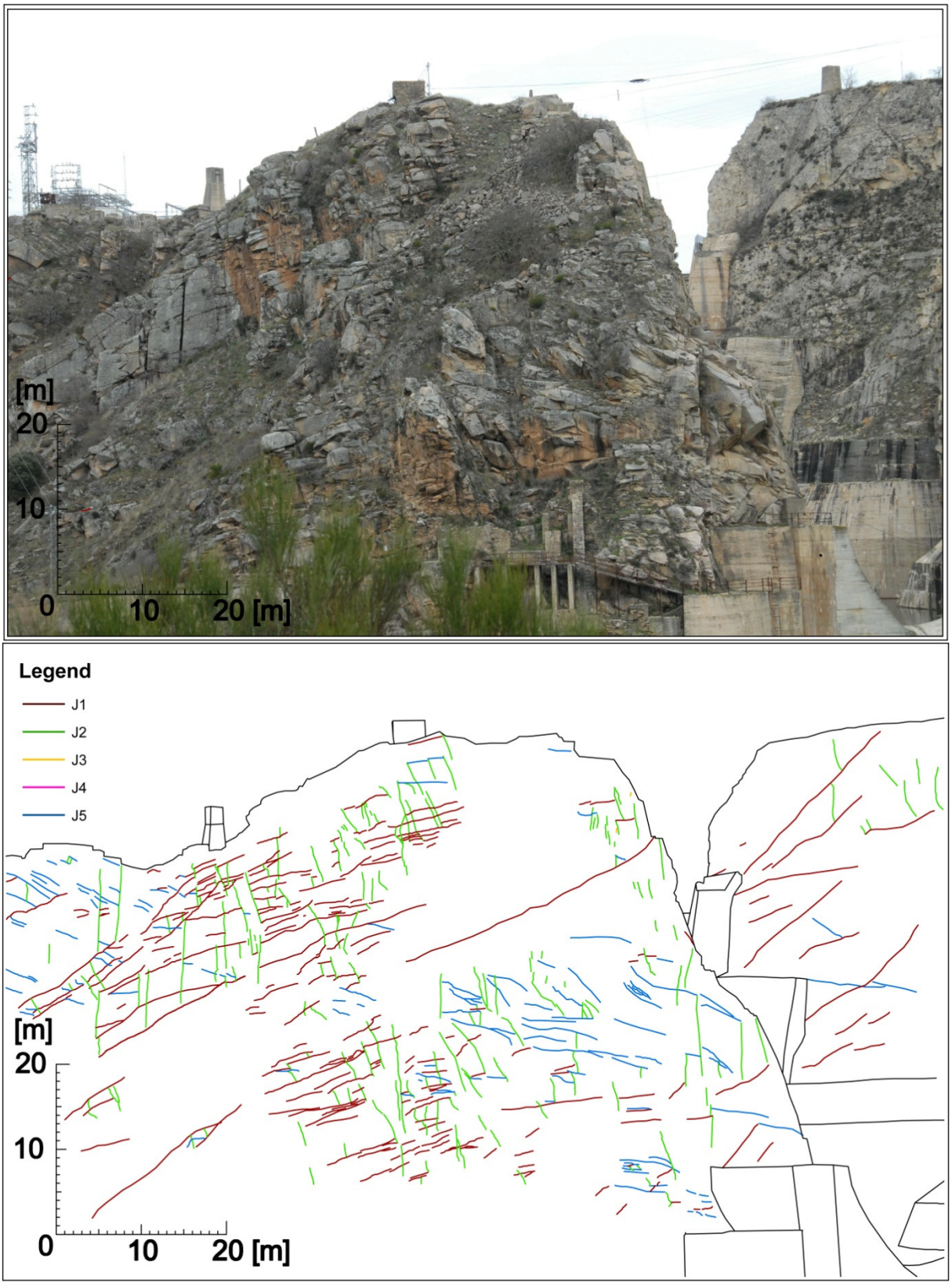

Figure 6.11 – Trace map 1 – Photo (above) and derived trace map (below)

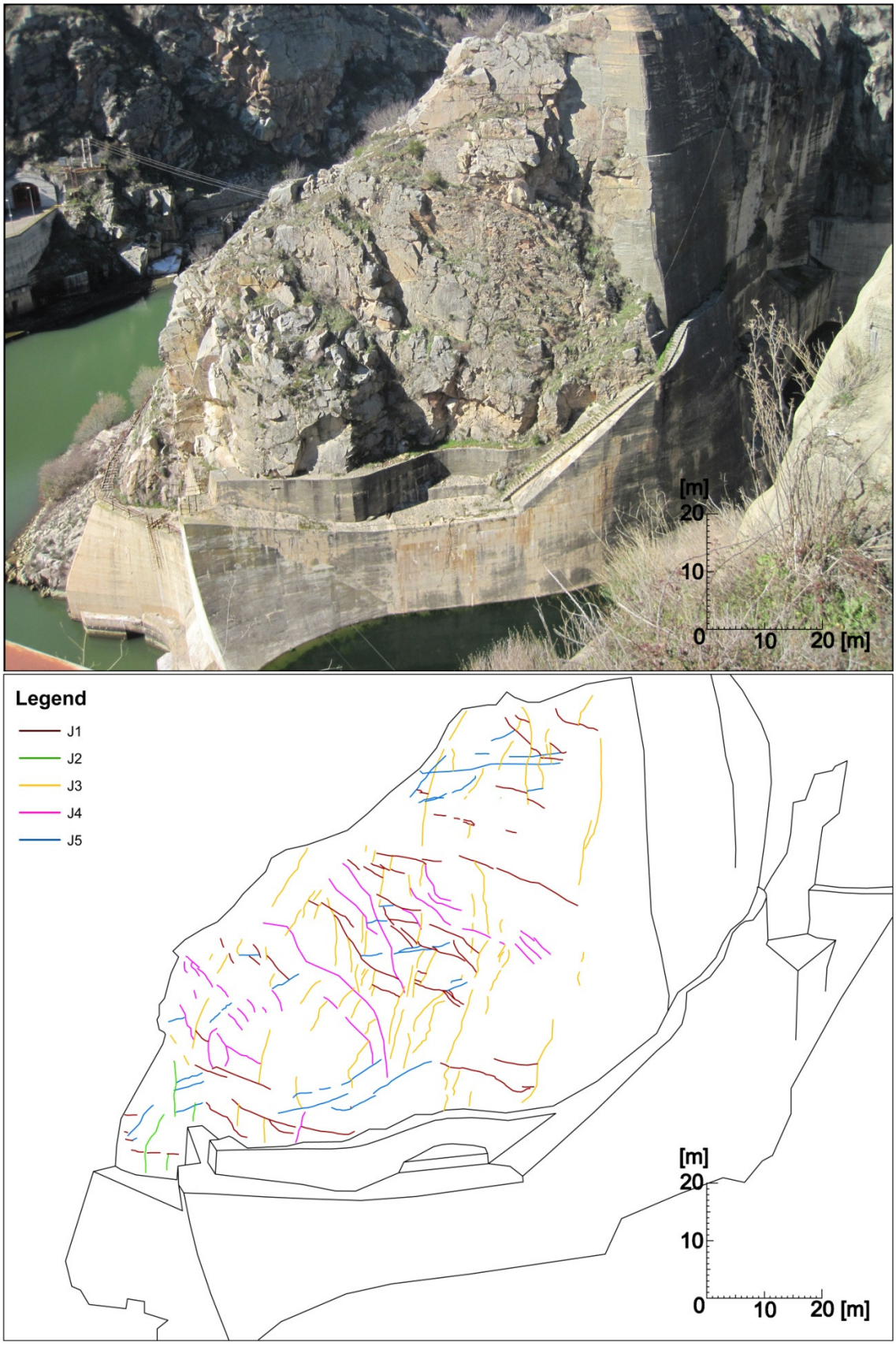

Figure 6.12 – Trace map 2 – Photo (above) and derived trace map (below)

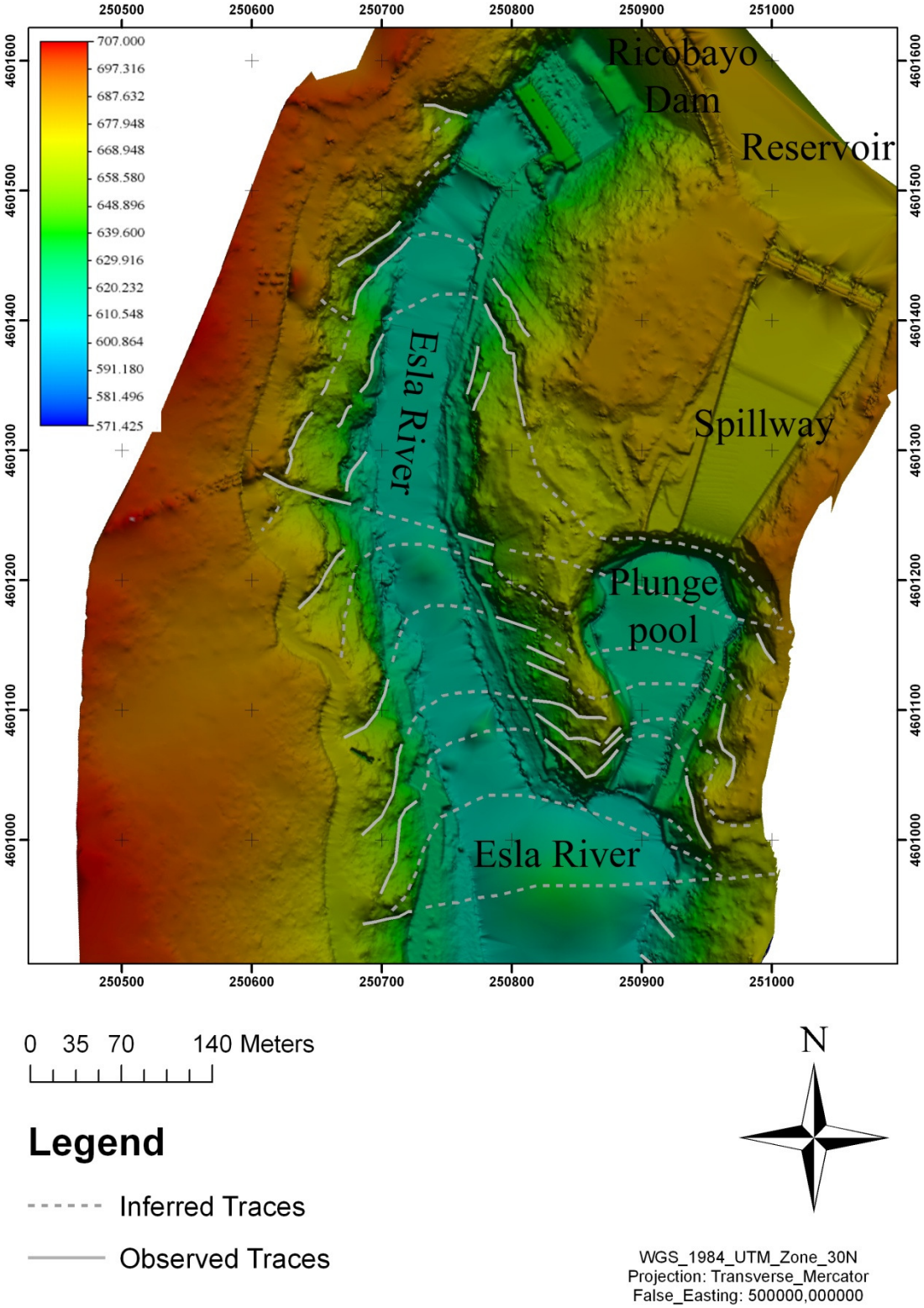

Figure 6.13 – Major lineaments interpreted from the topography and field data (Base map: False colour elevation model)

6.4 Roughness

The joint surfaces are mainly planar to undulating (ISRM, 1981). Joint sets 2, 3, 4, and 5 present some roughness, and set 1 is slickensided. The small scale (10cm) joint roughness coefficient (JRC) varies slightly from set to set, with frequency peaks usually between 4 and 10, see Figure 6.15. The JRC histograms for each joint set are presented in Figures 6.15 to 6.19, the summary of the measurements statistics is shown in Table 6.4.

Figure 6.14 – Set 1 slickensides

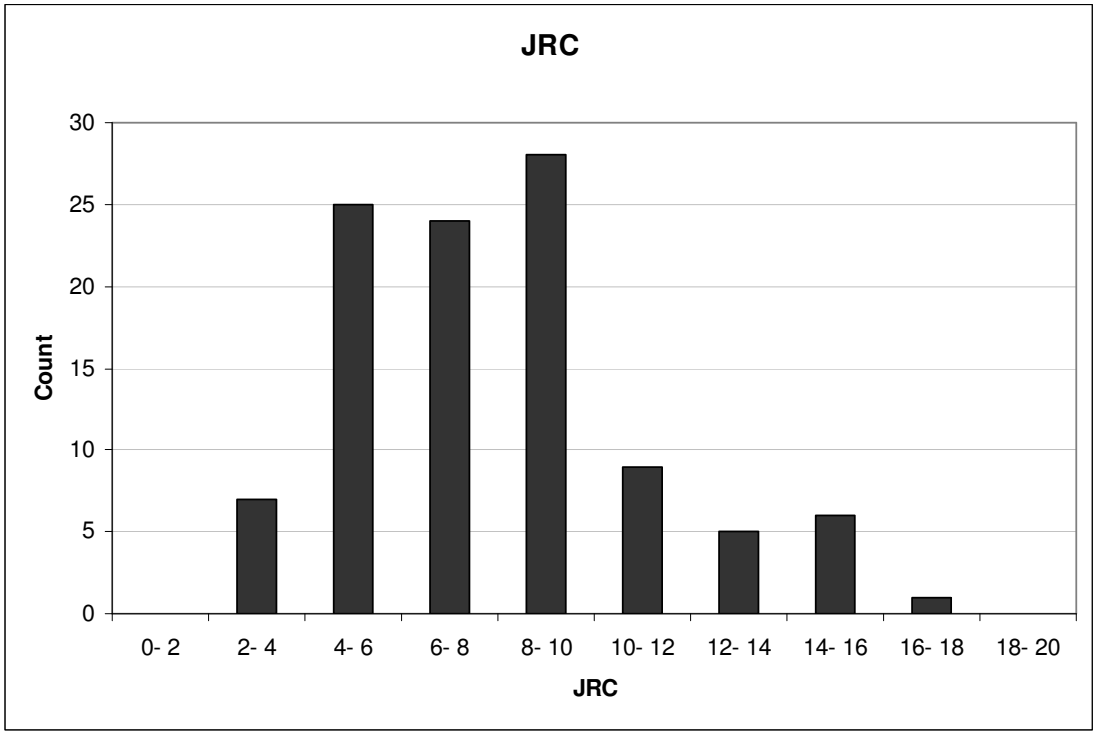

Figure 6.15 – JRC histogram of all measured joint surfaces (104 measurements)

Joint set	JRC [-]		
	Mean	Standard deviation	Number of measurements
J1	9	3	16
J2	8	4	32
J3	8	3	20
J4	7	3	29
J5	8	2	10

Table 6.4 – JRC statistical summary

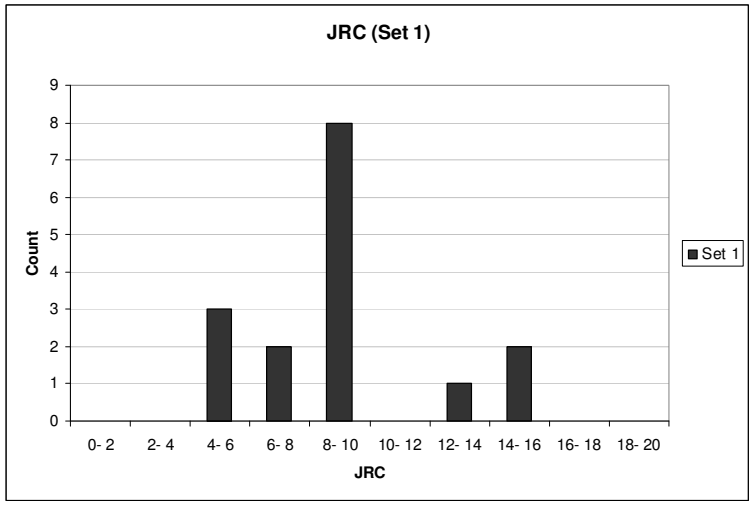

Figure 6.16 – JRC histogram – Set 1 (16 measurements)

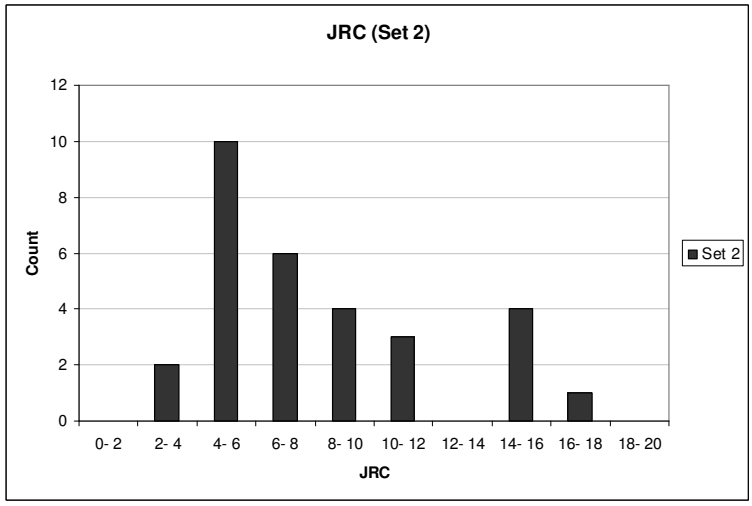

Figure 6.17 - JRC histogram – Set 2 (32 measurements)

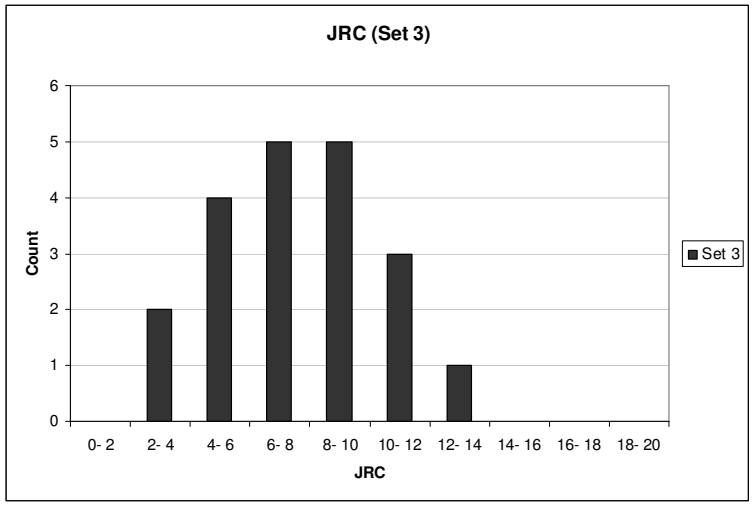

Figure 6.18 - JRC histogram – Set 3 (20 measurements)

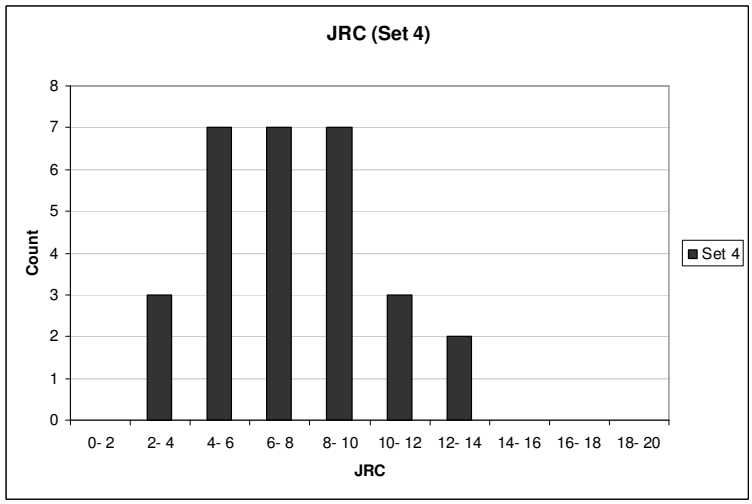

Figure 6.19 - JRC histogram – Set 4 (29 measurements)

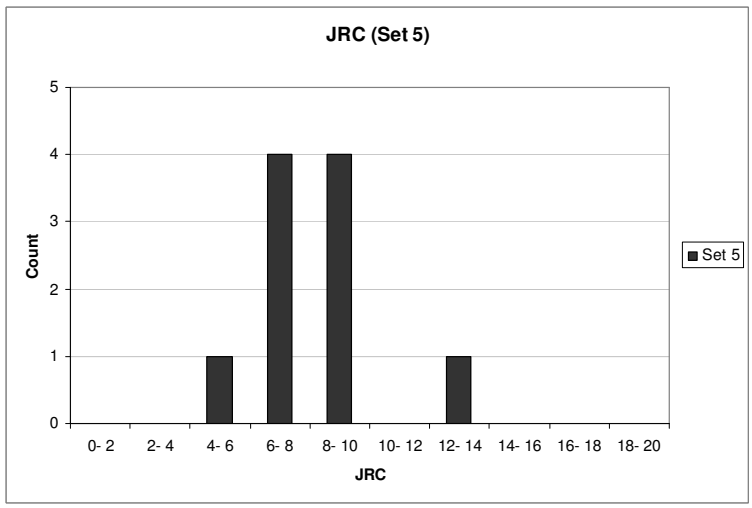

Figure 6.20 – JRC histogram – Set 5 (10 measurements)

6.5 Wall strength

The intact rock unconfined compressive strength (UCS) was reported ranging from 79 to 128 MPa, with mean value of 100 MPa, according to the geotechnical report for the construction of Ricobayo II (Iberduero S.A). The granitoid rocks comprising the discontinuity walls are described as strong to very strong (ISRM, 1981), see Figure 6.21. When weathered, the rock is much weaker, reaching strength index values R0, mainly along highly weathered discontinuities.

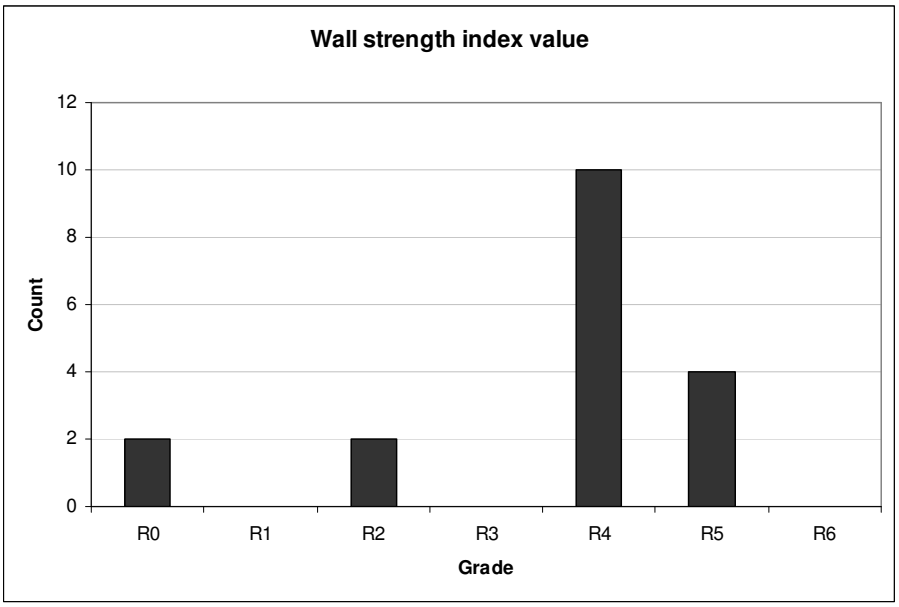

Figure 6.21 – Estimated wall strength index values

Weathering grades ranging from III to IV have been reported up to 15m depth and grade II is reported below this level (Iberduero S.A.). Field observations on weathering grades of the discontinuities usually indicated ranges up to 5m for grades III or higher. Weathering grade II prevails throughout the site and in depth, see Figure 6.22. A typical weathering situation along discontinuities close to the surface is illustrated in Figure 6.23. Stronger weathering has been observed along discontinuities under influence of water seepage and surface streams, see Figure 6.24.

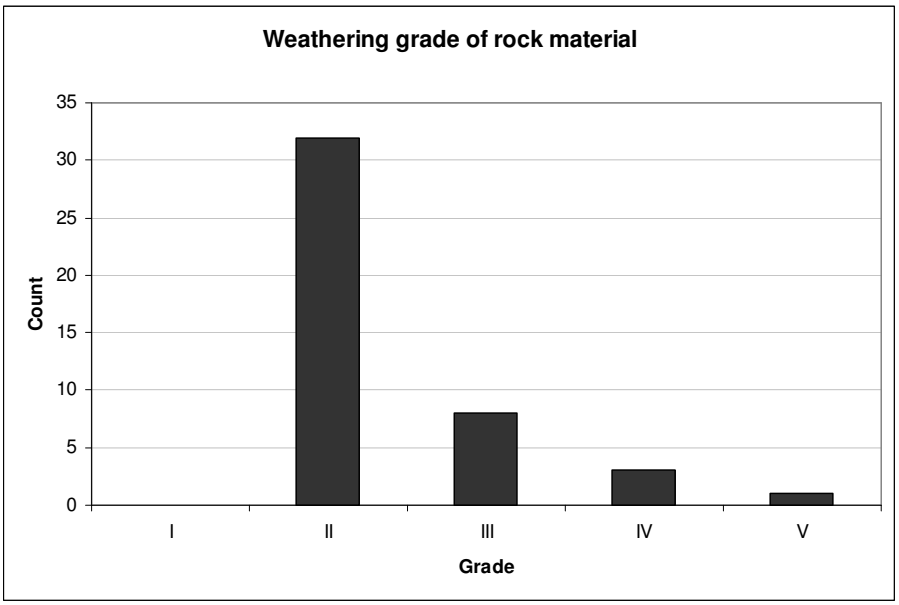

Figure 6.22 – Estimated weathering index values

Figure 6.23 – Typical weathering situation close to the surface and along discontinuity plane

Weathering grades indicate that rock material may be somewhat weaker externally than its fresh condition (ISRM, 1981); nonetheless, field description for the rock wall strength indicate, as already mentioned, that joint compressive strength (JCS) is approximately the same as for the reported for the intact rock (ISRM, 1981). For that reason further analysis will be performed using a JCS value equal to the UCS reported by Iberduero S.A. and used for the design of Ricobayo II.

Figure 6.24 – Strong weathering observed along wet discontinuity planes.

6.6 Aperture

Discontinuities are “gapped” at the surface, description varies from open (0,5-2,5mm) to moderately wide (2,5-10mm). Below ground level the joints are “closed” varying from tight (0,1-0,25mm) to partly open (0,25-0,5mm). Typical aperture conditions at the surface and underground are illustrated in Figure 6.25. In areas with signs of instabilities, where blocks appeared to be moved, joints are “open” and very wide apertures have been observed (1-10cm), see Figure 6.26.

Figure 6.25 – Typical joint plane apertures at the surface and underground

Figure 6.26 – Joint aperture in unstable areas

6.7 Filling

Discontinuities are clean, no filling has been observed underground and in outcrops apart from discontinuities close to the surface where weathering grades are high. In these cases granular material, originated from weathering of the host rock, has been observed and discontinuity width depends on the weathering situation of the particular joint, see Figure 6.23. As already mentioned, this weathering phenomenon has not been observed deeper than 5 meters.

6.8 Seepage

Water is locally present at the surface and some minor streams enter right side of the Esla River, Figure 6.27. Discontinuities may be wet or present minor seepage, but no flow has been observed, not even underground, Figure 6.27.

Figure 6.27 – Water condition observed in winter of 2011

6.9 Block size

Using the sum of the joint frequency of each joint set as an estimate of the joint volumetric count ($J_v = \sum_{i=0}^{n} {}^{1}/_{S_i}$, where S_i is the average joint spacing of joint set i), the measurements along the scanline yield a J_v of 2,8 joints/per m³. The joint frequency along the scanline, taking into account all joint sets, is presented in Figure 6.28. According to ISRM (1981), the estimated J_v is related to large blocks, ranging from 0,2 to 8 m³. The estimated block volume agrees with field observations and reported block sizes encountered inside the plunge pool, but blocks may also be larger. Figure 6.29 illustrates the rock blocks encountered inside the plunge pool in 1934 (Riesco Chueca, 2010) and after a rock fall event in 1961 (Iberduero S.A., 1961), where the estimated block volume was 8 m³.

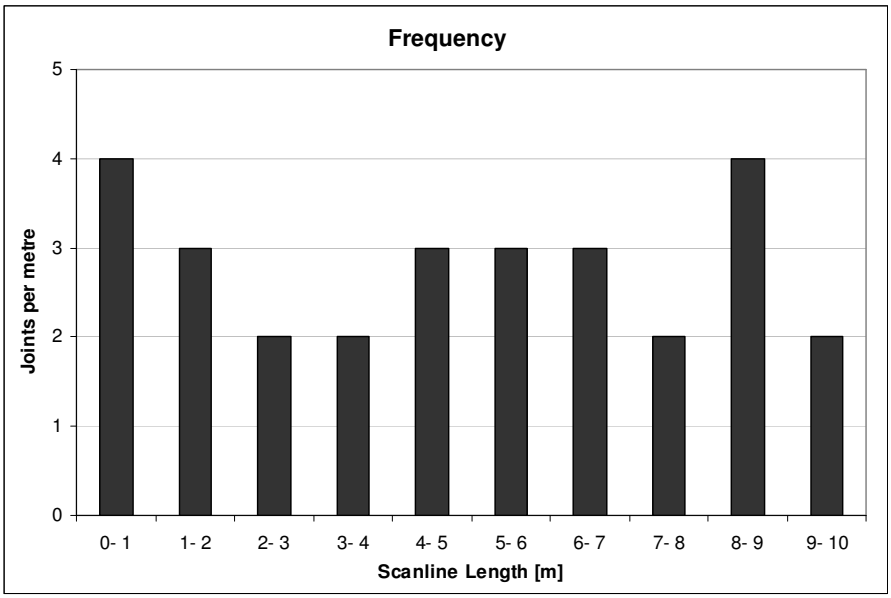

Figure 6.28 – Frequency along Scanline – all sets considered.

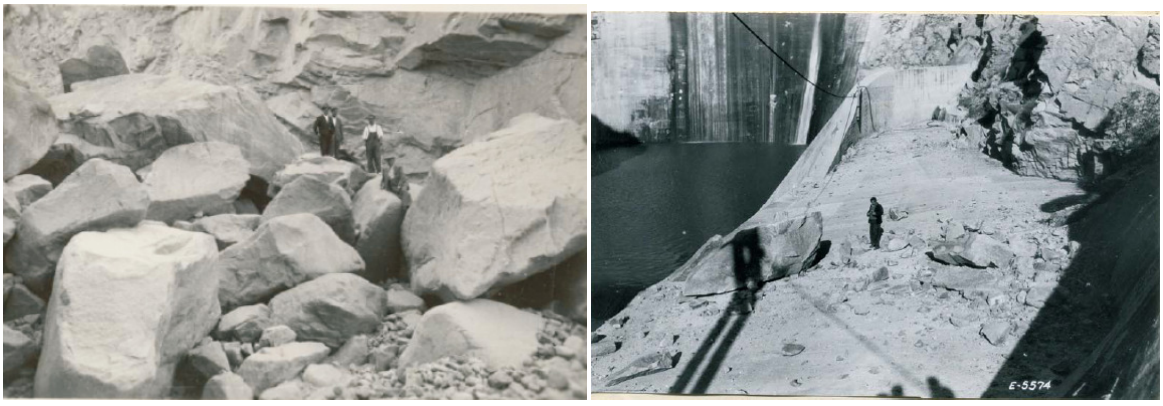

Figure 6.29 – Rock blocks encountered inside the plunge pool, from Riesco Chueca (2010) and Iberduero S.A. (1961)

6.10 Shear strength of discontinuities

The shear strength properties of the discontinuities are estimated using the equation of Barton and Choubey (1977):

$$\Phi_{peak} = \Phi_r + JRC \log_{10}\left(\frac{JCS}{\sigma_n'}\right) \quad \textbf{Eq. 6.1}$$

where: Φ_{peak}: Peak friction angle,

Φ_r: Residual friction angle

JRC: Joint roughness coefficient

JCS: Joint strength coefficient

σ_n': Effective normal stress acting on the joint surface.

To take scale effects into account the parameters JRC and JCS have been corrected according to Barton and Bandis (1982) equations:

$$JRC_n = JRC_0 \left(\frac{L_n}{L_0}\right)^{-0,02JRC_o} \quad \textbf{Eq. 6.2}$$

$$JCS_n = JCS_0 \left(\frac{L_n}{L_0}\right)^{-0,03JRC_o} \quad \textbf{Eq. 6.3}$$

where JRC_0, JCS_0, and L_0 (length) refer to small scale (10cm) measurements and JRC_n, JRC_n, and L_n refer to real block sizes. The calculations are shown in Table 6.5. Some comments are necessary regarding the effective normal stress (σ_n') estimated for the calculation of the peak friction angles. For joint sets 2, 3, and 4 the effective normal stress approaches zero and Eq. 6.3 results in very high friction angles. According to Wyllie and Mah (2004) values exceeding 50° are unreasonable for design purposes, and the authors suggest a useful range of the ratio JCS/σ_n' between 3 and 100. For the mentioned steep joint sets (2, 3, and 4) the ratio was assumed 100, for the remaining joint sets the ratio was estimated varying from 45 to 191. For these cases the ratio was assumed 72. The residual friction angle was assumed 30° based on values for granitic rocks reported by Barton (1973).

	J1		J2		J3		J4		J5	
	Mean	Standard deviation	Mean	Standard deviation	Mean	Standard deviation	Mean	Standard deviation	Mean	Standard deviation
L_0 [cm]	10	-	10	-	10	-	10	-	10	-
JRC_0 [-]	9	3	8	4	8	3	7	3	8	2
JCS_0 [MPa]	100	-	100	-	100	-	100	-	100	-
L_n [cm]	150	-	150	-	150	-	150	-	150	-
JRC_n [-]	5	1	5	1	5	1	5	1	5	1
JCS_n [MPa]	50	12	53	16	56	13	57	14	52	9
JCS_n/σ_n [-]	72	-	100	-	100	-	100	-	72	-
ϕ_r [°]	30	-	30	-	30	-	30	-	30	-
ϕ_{peak} [°]	39	2	40	2	40	2	40	2	39	2

Table 6.5 – Estimated strength parameters of discontinuity sets

The reduction of shear strength in the presence of water has been addressed in the literature. According to Barton (1973), supported by limited data, from an engineering point of view shear strength reduction appears to range between 5 and 30%. In this Master Thesis a reduction of 20% on peak shear strength has been considered to cover water effects on shear strength of rock joints.

7 Stability Analysis

For the study of the slopes around the Ricobayo plunge pool, three free surfaces are assumed. These are the plunge pools side walls, left and right looking downstream, and the head wall, which experienced back erosion. The intent is to analyse the rupture of the side walls, and consequent enlargement of the plunge pool, as well as the possible influence of slope instabilities upon the sudden and quick back erosion process. As already mentioned, historic descriptions of the process describe it as concentrated in time and involving large rock mass volumes. The stability analyses of the walls around the plunge pool are performed deterministically and probabilistically using block theory. The deterministic analysis is performed for a dry condition; removable blocks and their failure modes are graphically identified. The stereographic plots used for the graphic analyses were obtained using a DOS program written by Goodman and Shi (1989), modified to HPGL file output by Dr.Q.Liu (2004). The safety factors are calculated and used for comparison with the results of probabilistic analyses. The probabilistic analyses are performed for constant slope and water pressure conditions (dry and completely filled joints) and variable joint orientation and friction angles using Swedge and RocPlane.

7.1 Input parameters

7.1.1 Slope parameters

The slope directions have been estimated based upon a topographic map from 1937, provided by Iberdrola S.A.. In Figure 7.1, estimated directions are illustrated. Additionally to the wall faces the upper slopes are also considered. The wall faces (slope) are considered to be vertical (90°) and the upper slope flat (0°). These assumptions do not seem unrealistic, as may be observed in historical photographs presented in Chapter 4.

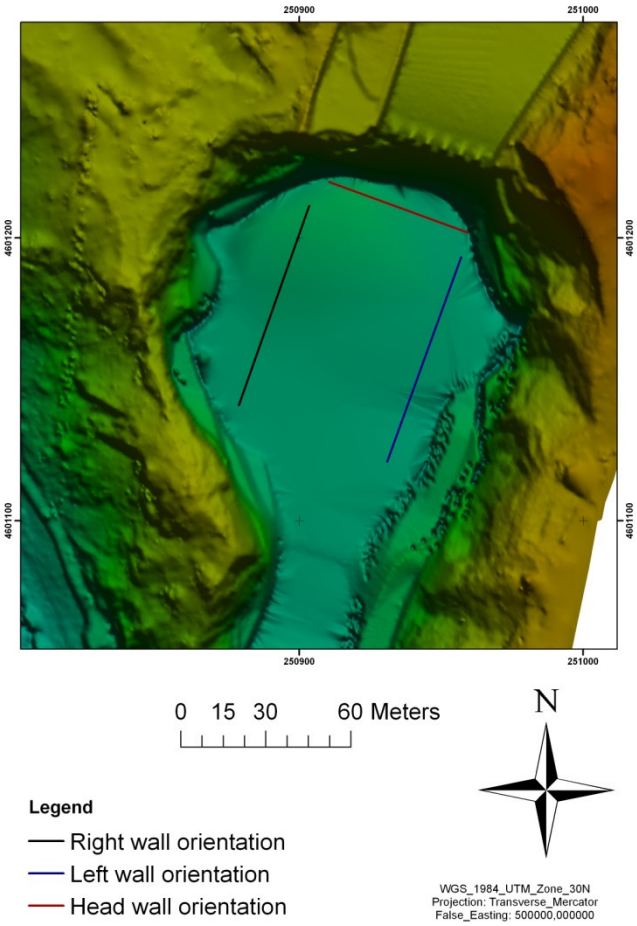

Figure 7.1 – Estimated slope directions

Slope dimensions have been estimated according to the development of the scour process. Scour events 2 (SE2), 3 (SE3), and 4 (SE4) are analyzed. All slope parameters are summarized in Table 7.1. The slope parameters are considered constant for all analyses, deterministic and probabilistic.

	Head wall	Left wall	Right wall
Slope (Dip/Dip dir.)	90°/201°	90°/300°	90°/120°
Upper Slope (Dip/Dip dir.)	0°/201°	0°/300°	0°/120°
Height/Length - SE2	30/70	50/150	30/150
Height/Length – SE3	65/70	85/150	65/150
Height/Length – SE4	85/70	105/175	85/175

Table 7.1 – Slope parameters

7.1.2 Joint parameters

All recognized joint sets are used for stability analyses. The parameters are summarized in Table 7.2.

Joint set		J1	J2	J3	J4	J5	PDF
Orientation	Mean (Dip/Dip dir.)	31°/340°	85°/132°	88°/248°	85°/192°	19°/155°	Fisher
	Fisher constant k	13,46	10,66	15,75	13,59	12,63	
Friction angle	Mean	40°	40°	40°	40°	40°	Normal
	Standard deviation	2°	2°	2°	2°	2°	
Spacing	Mean [m]	1,3	1,3	1,9	1,2	0,9	Constant

Table 7.2 – Joint parameters considered for stability analyses

Joint orientation is assumed to have a Fisher probability distribution. The peak friction angles are similar for all joint sets, and for simplicity are assumed equal. For probabilistic analyses friction is assumed normally distributed with mean value 40° and standard deviation 2°. The friction has been truncated in probabilistic analyses; the relative minimum is the estimated residual friction angle (30°) and the relative maximum 50°. Joint spacing is considered constant, and estimates obtained from photogrammetry are used.

7.1.3 Water

The water force acting on the blocks (sliding wedges and planes) is considered static and constant (even for probabilistic analyses) according to the solution provided by Hoek and Bray (1981). Water table is assumed as a planar surface oriented parallel to the upper slope (RocScience, 2011). Maximum water pressure is considered acting at a point half-way down the line of intersection or sliding plane. Along the edges of the block in contact with the slope faces water pressure is assumed zero. Figure 7.2 illustrates the considered water pressure.

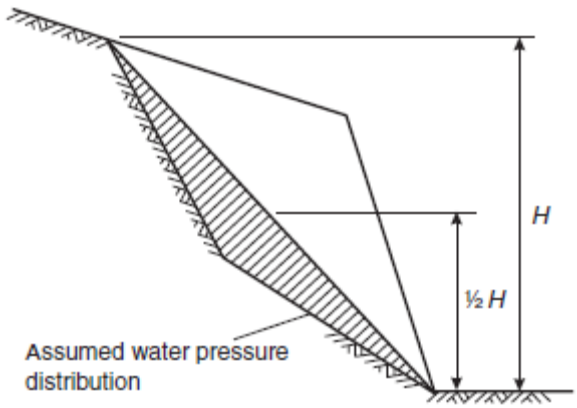

Figure 7.2 – Assumed water pressure distribution (Wyllie and Mah, 2004)

Two extreme situations have been calculated, considering completely dry and completely filled joints, such that $p_{max} = {}^{1}/_{2} \cdot \gamma_w \cdot H$. In this configuration the water pressure distribution is assumed triangular for the case of plane sliding and a tetrahedron in each face of the sliding wedge. The water force resultant is (RocScience, 2011):

- Plane sliding

$$U = \frac{(p \cdot H)^2 \cdot \gamma_w}{4 \cdot sin\alpha} \qquad \textbf{Eq. 7.1}$$

- Wedge sliding

$$U = \frac{1}{6} \sum_{i=1}^{2} p^3 \cdot \gamma_w \cdot H \cdot a_i \cdot \hat{n}_i \qquad \textbf{Eq. 7.2}$$

Where: H = height of the slope
γ_w = unit weight of the water
α = dip of the sliding plane,
p = proportion filled (1 in this case),
a_i = area of i^{th} joint face,
$\hat{n}_i$ = inward normal of i^{th} joint face.

7.1.4 Sampling size

To perform the stability analyses in a probabilistic manner a representative number of iterations must be chosen. It is not clear the number of samples needed for a stable result of the probability of failure. Large samples provide solid results, but are time

consuming, and small samples may result non representative. The sampling size has been studied for all three slope surfaces, but only one failure mode has been arbitrary chosen for the study, failure mode 34. The probability of failure variation with the sample size, for mode 34, is presented in Figures 7.3 to 7.5. Analyses show that a sample size of 50000 iterations is enough to obtain solid values. This sample size has been used for all probabilistic analyses.

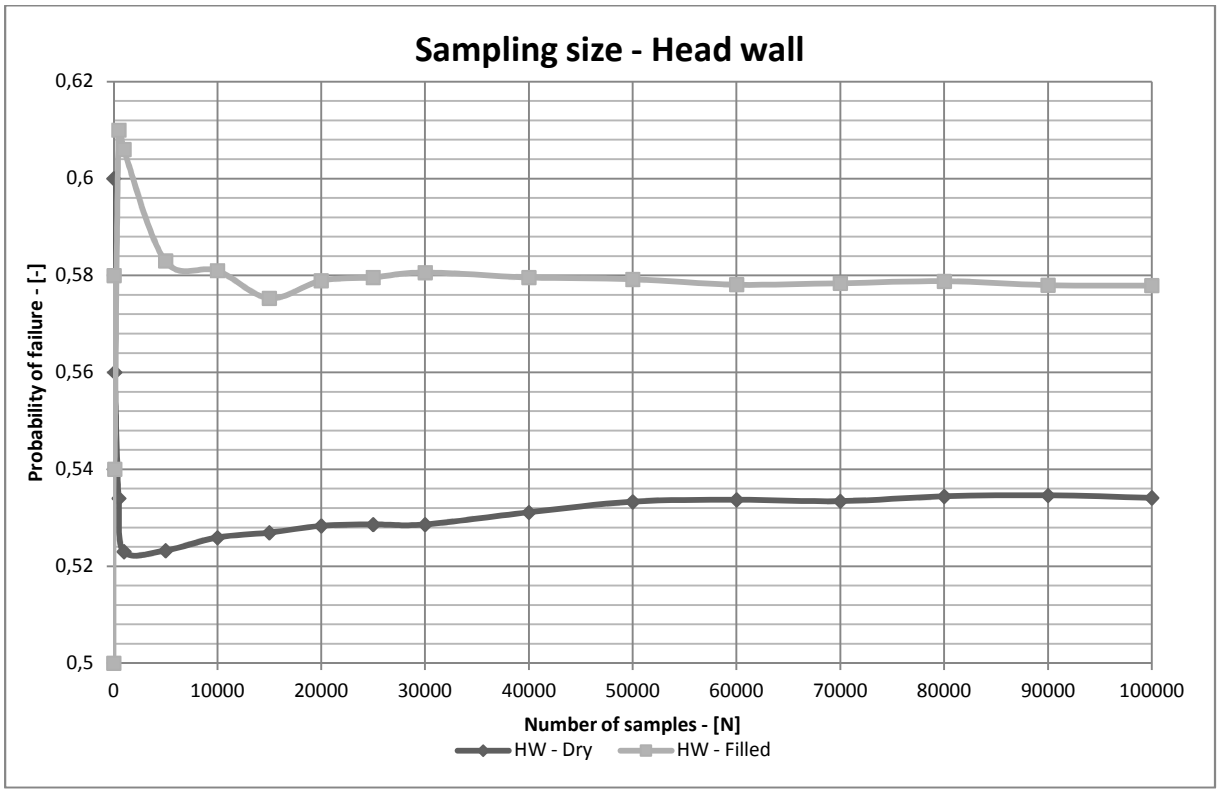

Figure 7.3 – Probability of failure variation with sample size – Head wall

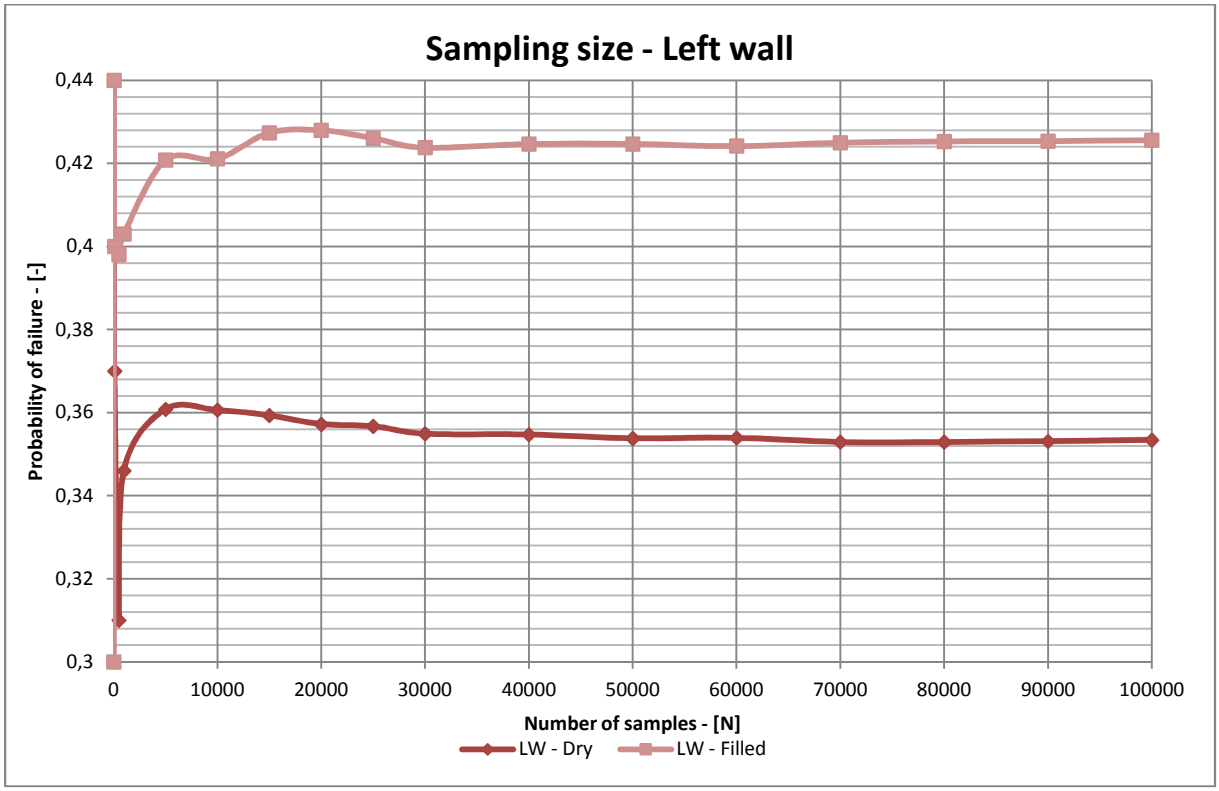

Figure 7.4 - Probability of failure variation with sample size – Left wall

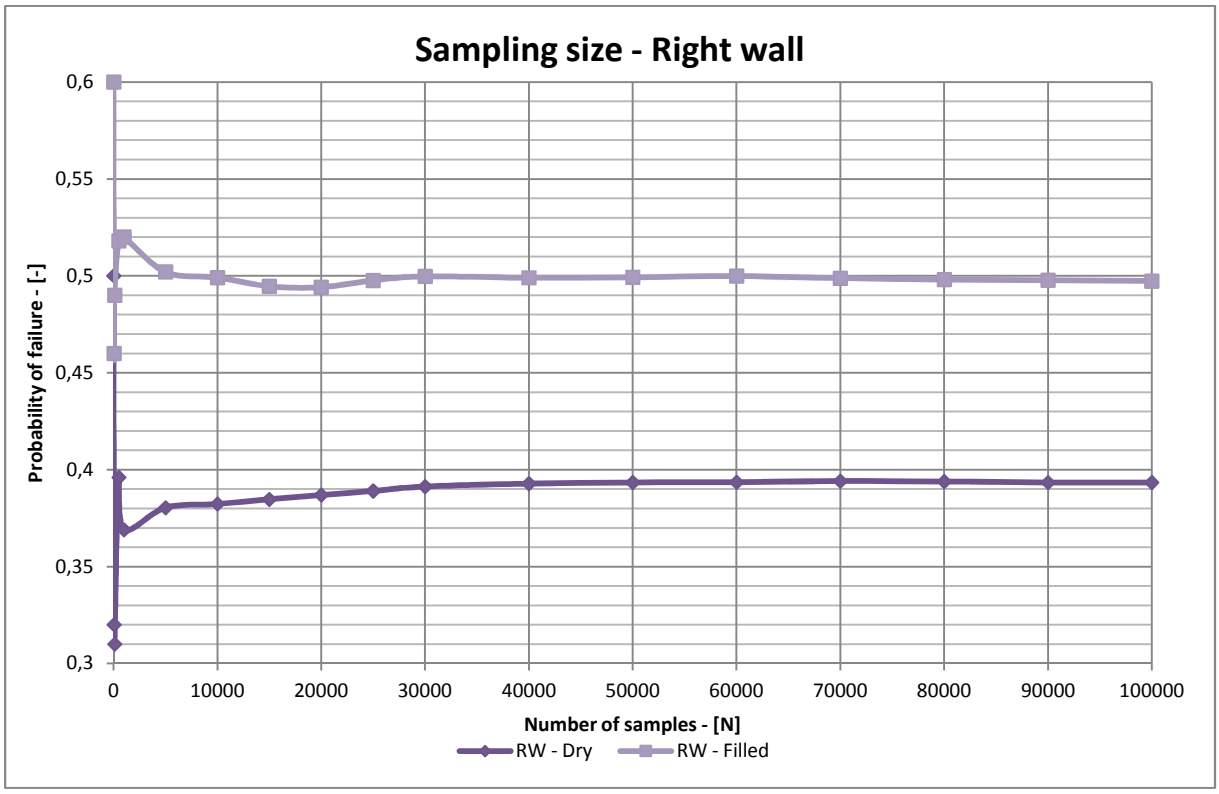

Figure 7.5 - Probability of failure variation with sample size – Right wall

7.2 Head wall

The results of the block theory removability analysis of the head wall, which experienced back migration, are presented graphically in Figure 7.6. Finite removable blocks are shaded, and the free faces are outlined in red together with the indication of the excavation pyramid (EP) which is shaded in brown. In this configuration 12 removable blocks are present. The failure modes related to each removable block when gravity acts alone are graphically presented in Figure 7.7. Results of the removability and mode analyses are summarized in Table 7.3, where the estimated block volumes using block theory formulation constrained by the set spacing are also presented.

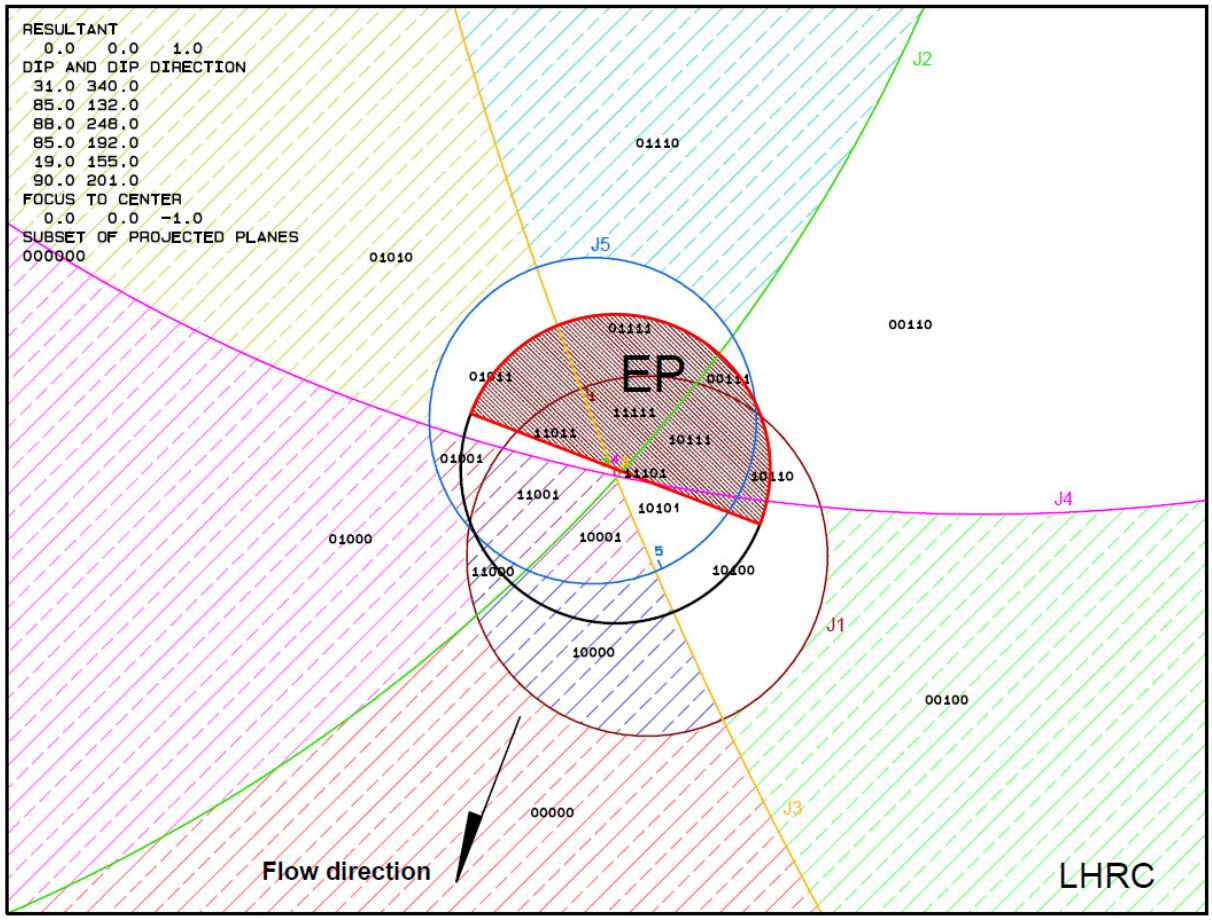

Figure 7.6 – Block removability – Head wall compound slope

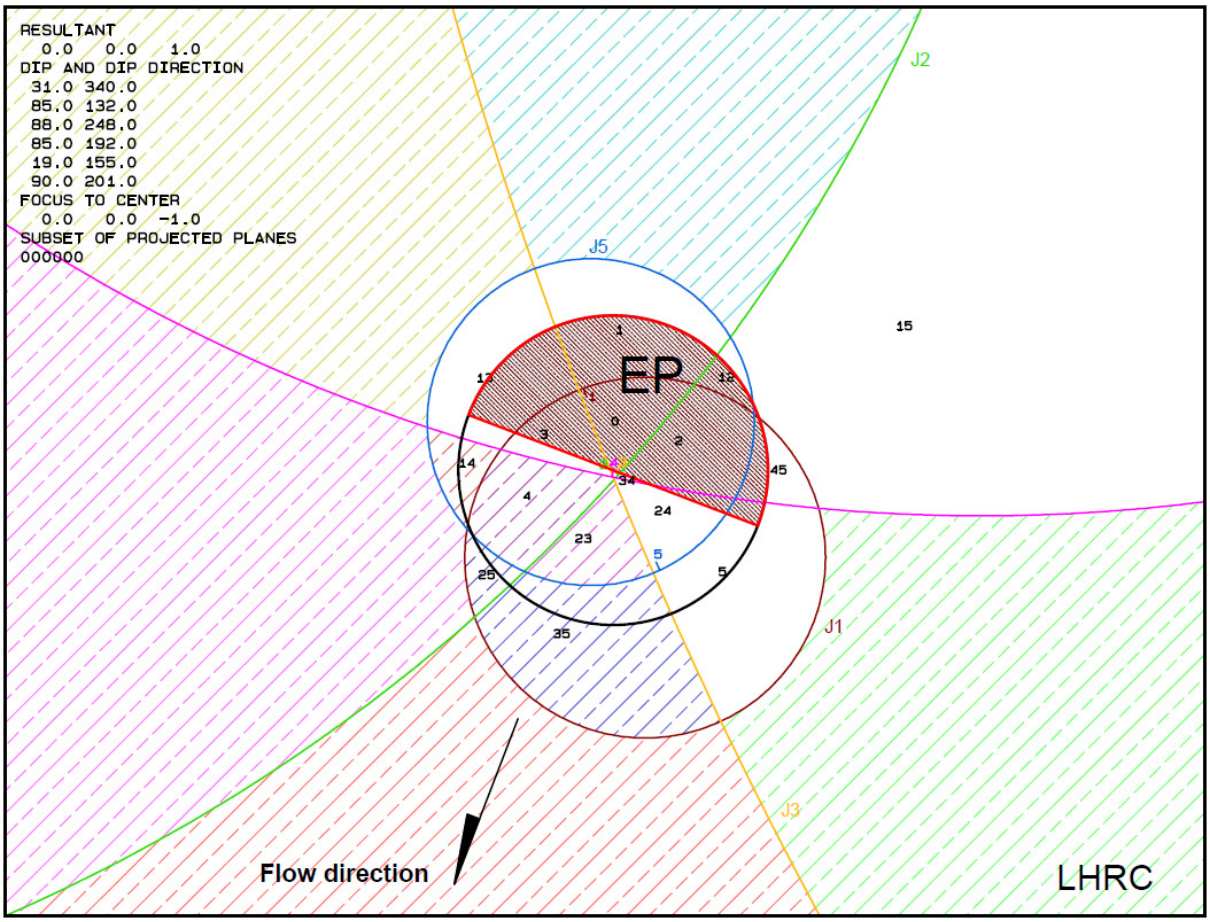

Figure 7.7 – Mode analysis – Head wall compound slope

Removable block	Failure mode	Block volume [m³]
JP00000	-	15,6
JP00010	-	18,4
JP00100	-	29,0
JP01000	-	21,2
JP01001	14	63,1
JP01010	-	34,9
JP01110	-	59,2
JP10000	35	18,1
JP10001	23	101,0
JP11000	25	16,0
JP11001	4	191,0
JP11101	34	141,0

Table 7.3 – Mode analysis summary – Headwall compound slope

Results show that 6 removable blocks are type III (safe even without friction), which do not present a failure mode. Safety factors from the removable blocks which

present a failure mode (potential and real key blocks) are presented in Table 7.4. The JP's which form real key blocks in the head wall are: JP10001 with sliding on intersection 23, JP11001 with sliding on plane 4 and JP11101 with sliding on intersection 34. Identified key blocks present extremely low safety factors, which are related to high plunge angles of the sliding directions.

To enhance the stability analyses a probabilistic study has also been performed for all possible wedge sliding modes and for sliding on plane 4, which is the only joint set striking nearly parallel to the slope (±20°, according to Hoek and Bray, 1981). The results obtained from the probabilistic analyses are summarized in Table 7.4. To facilitate visualization the results are also graphically presented in Figure 7.8. Probabilistic analyses have been performed using the software Swedge and RocPlane (RocScience, 2011) and take into account just the joint sets involved in failure, i.e., for the failure mode 12 just joint sets 1 and 2 have been considered forming the wedge together with the free faces. In this regard, the analyses are different from block theory, which takes all joint sets into account, but for a dry configuration the results are the same since friction is mobilized just on the sliding planes.

Failure Mode	**Block Theory**	**Probability of Failure**					
	Dry	Dry			Filled		
	FS	Kinematic	Kinetic	Total	Kinematic	Kinetic	Total
	[-]						
4	0,07	0,489	1,000	0,489	0,489	1,000	0,489
12	Stable	0,227	0,007	0,002	0,227	0,058	0,013
13	Stable	0,043	0,222	0,010	0,043	0,236	0,011
14	4,25	0,583	0,127	0,074	0,583	0,343	0,199
15	Stable	0,446	0,022	0,010	0,446	0,149	0,067
23	0,18	0,608	0,762	0,463	0,608	0,934	0,570
24	Stable	0,593	0,797	0,473	0,593	0,925	0,552
25	8,49	0,660	0,038	0,025	0,661	0,172	0,114
34	0,10	0,618	0,863	0,533	0,618	0,935	0,579
35	2,49	0,860	0,097	0,084	0,907	0,365	0,331
45	Stable	0,496	0,224	0,111	0,495	0,553	0,274

Table 7.4 – Stability analyses summary – Head wall compound slope

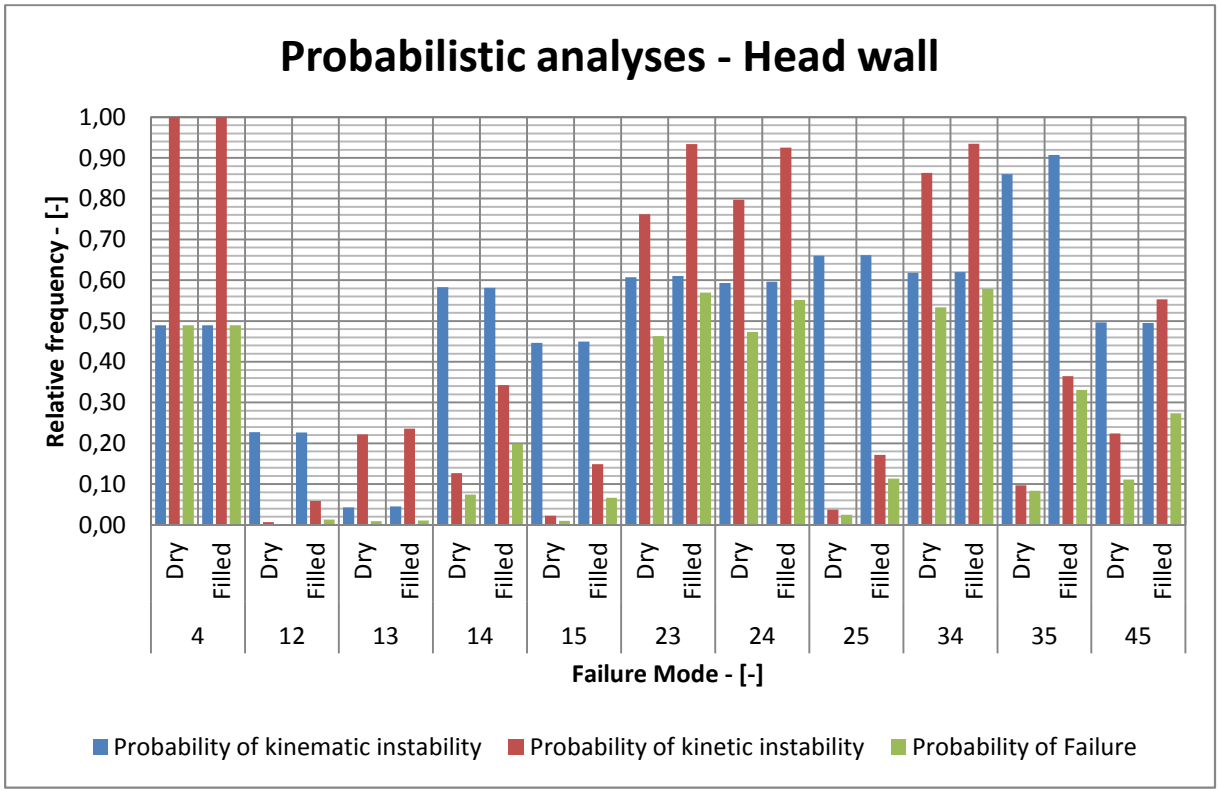

Figure 7.8 – Probabilistic analyses – Head wall compound slope

Probabilistic analyses show failure modes 4, 23, 24 and 34 to be critical. These wedges present high probabilities of kinematical (around 50 to 60%) and kinetic instabilities (around 80 to 100%) and consequently high probabilities of failure (around 50 to 60%), no matter if in dry or wet conditions. In others words these blocks present high probability of removability (kinematical instability) and, if removable also high probability of sliding (kinetic instability). A remarkable difference to a deterministic approach arises already; failure mode on intersection 24 has shown to be stable when stability is evaluated by means of mean orientation values. The results show the influence of steep joints in mechanical behaviour of the head wall.

Other potentially unstable wedges present failure modes on intersections 14, 35 and 45. These wedges have probabilities of failure varying from around 20 to 33% in wet conditions. These failure modes are identified with block theory, but are shown to be stable with enough friction (Type II). This behaviour is also seen in probabilistic analyses, where these wedges present high probabilities of kinematical instability but not very high probabilities of kinetic instability. They are, therefore, most likely to be removable with probabilities varying from 50 to 90%, and when removable failure may happen with 35 to 55% chance. Failure mode 25, which is also identified in block

theory, presents also high kinematical instability probability (around 60%) but low probability of kinetic instability. Its probability of failure lies around 11% for wet conditions.

The ratio of kinetic instability in dry and wet conditions permits an evaluation of the influence of water on the stability of removable blocks. This ratio is graphically presented in Figure 7.9. It is clear from the graphic that water has no high influence in cases where sliding directions are very steep, higher than the real variation of the friction angle. In these cases the probability of failure is controlled by the probability of kinematical instability, failure occurs almost similarly in dry and wet conditions. For the head wall sliding in plane 4 and on intersections 23, 24 and 34 fall in these cases. These are the intersections between steep joint sets and sliding in a steep plane. The blocks, where friction is considerably mobilized, are much more sensitive to water and present probabilities of kinetic instability in dry conditions which are around 10 to 40% of the probabilities in wet conditions.

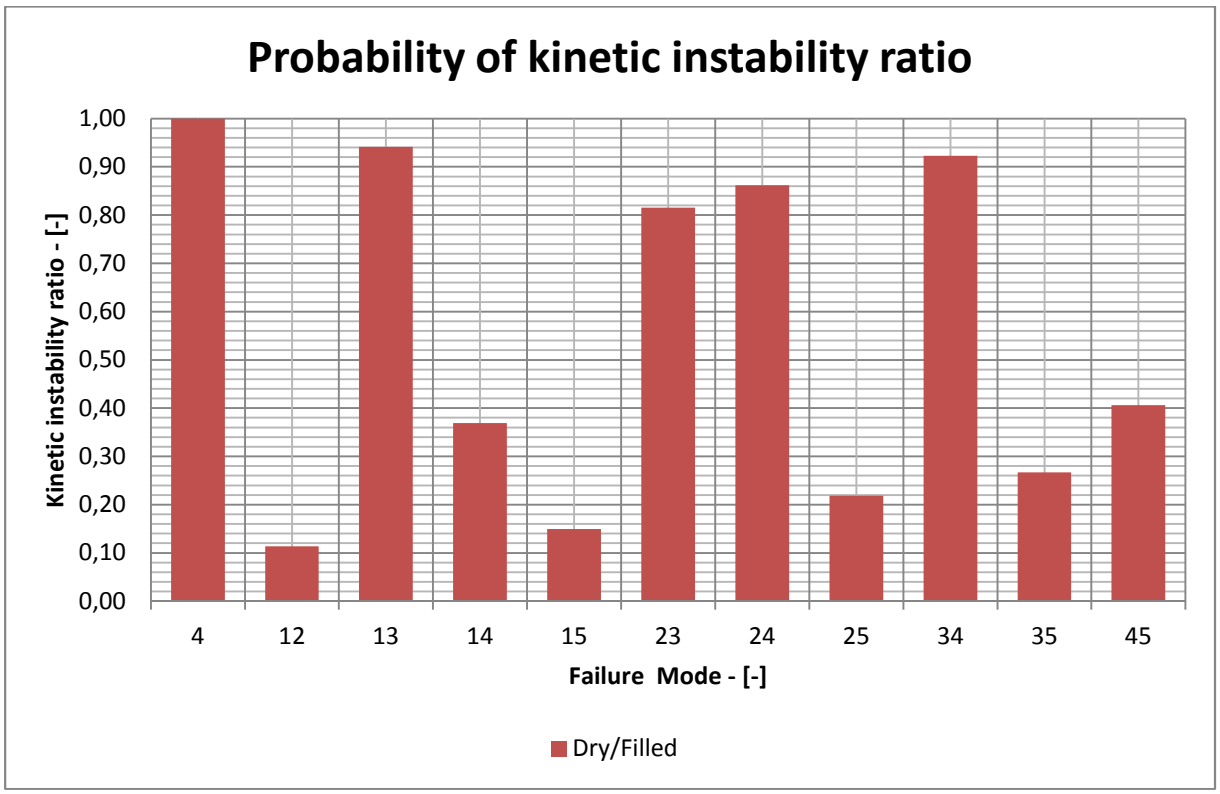

Figure 7.9 – Ratio of dry to filled probability of kinetic instability – Head wall compound slope

Another important aspect is the volume of rock involved in failure. The block volumes obtained from block theory constrained by joint set spacing have been presented in Table 7.3. Block volumes presented in Table 7.5 and graphically presented in Figure 7.10 are obtained from the software Swedge and RocPlane. The software calculates the block volume in the same manner, but the only constraints introduced in these cases are the slope dimensions. Blocks represent for these cases the largest possible blocks likely to form in a slope with this size, if joint persistence is considered infinite. The largest possible blocks may present conservative values and the ones obtained with the real spacing may not represent larger failure mechanisms. Real failure mechanisms may fall between these two extremes and the values already give an idea of the large volume of rock material involved. Another constraint that has not been taken into account is the joint persistence. Rock mass characterization shows evidence of high persistence, nonetheless failure mechanisms may involve smaller rock volumes than estimated for the largest possible.

The most critical failure mechanisms recognized (steep sliding directions) are also very sensitive to relief gain, involving a much larger rock volume as scour evolves from event 2 to 4. Rupture of the head wall protection, during scour event 4 may have been related to this phenomenon. On the other hand the largest block present (failure mechanism 12) is related to blocks most likely safe.

Stability information supports the idea of mechanical behaviour of a block system, which could have been undermined by water action, not directly by destabilizing the blocks (the most critical would be unsafe even in dry conditions) but by opening free space and gain of relief through scour.

Failure Mode	Probability Analysis					
	Dry			Filled		
	SE2	SE3	SE4	SE2	SE3	SE4
	[m³] or [m³/m]*					
4*	92	430	735	92	430	735
12	14004	23362	24569	13204	22719	24019
13	2953	3734	3954	3127	4265	4385
14	1956	2722	2814	1937	2754	2845
15	3828	3935	3935	3623	3726	3728
23	1483	10935	18635	1476	10819	18442
24	1297	4377	5827	1303	4346	5762
25	7881	11315	11754	7796	10846	11123
34	1097	3803	5181	1101	3873	5269
35	6404	10019	10381	6377	9873	10227
45	1181	1420	1437	1190	1417	1435

Table 7.5 – Mean block volume obtained from probabilistic analyses – Head wall compound slope.

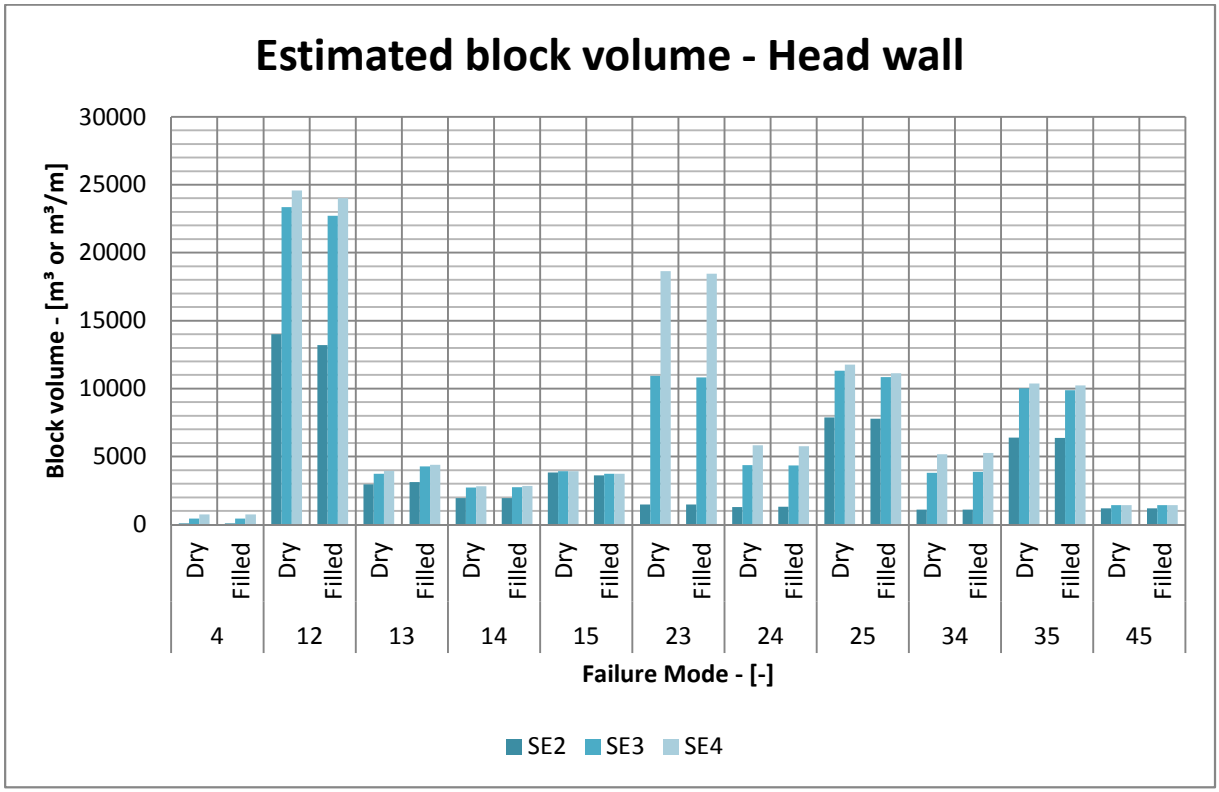

Figure 7.10 – Mean block volume obtained from probabilistic analyses – Head wall compound slope

7.3 Left wall

The removable blocks recognized for the left wall of the Ricobayo plunge pool are shaded in Figure 7.11, together with the excavation pyramid (EP). This side wall presents 9 removable blocks. Removable JP's are listed in Table 7.6, where the associated failure modes and block volumes are summarized. A mode analysis has been graphically performed and is shown in Figure 7.12.

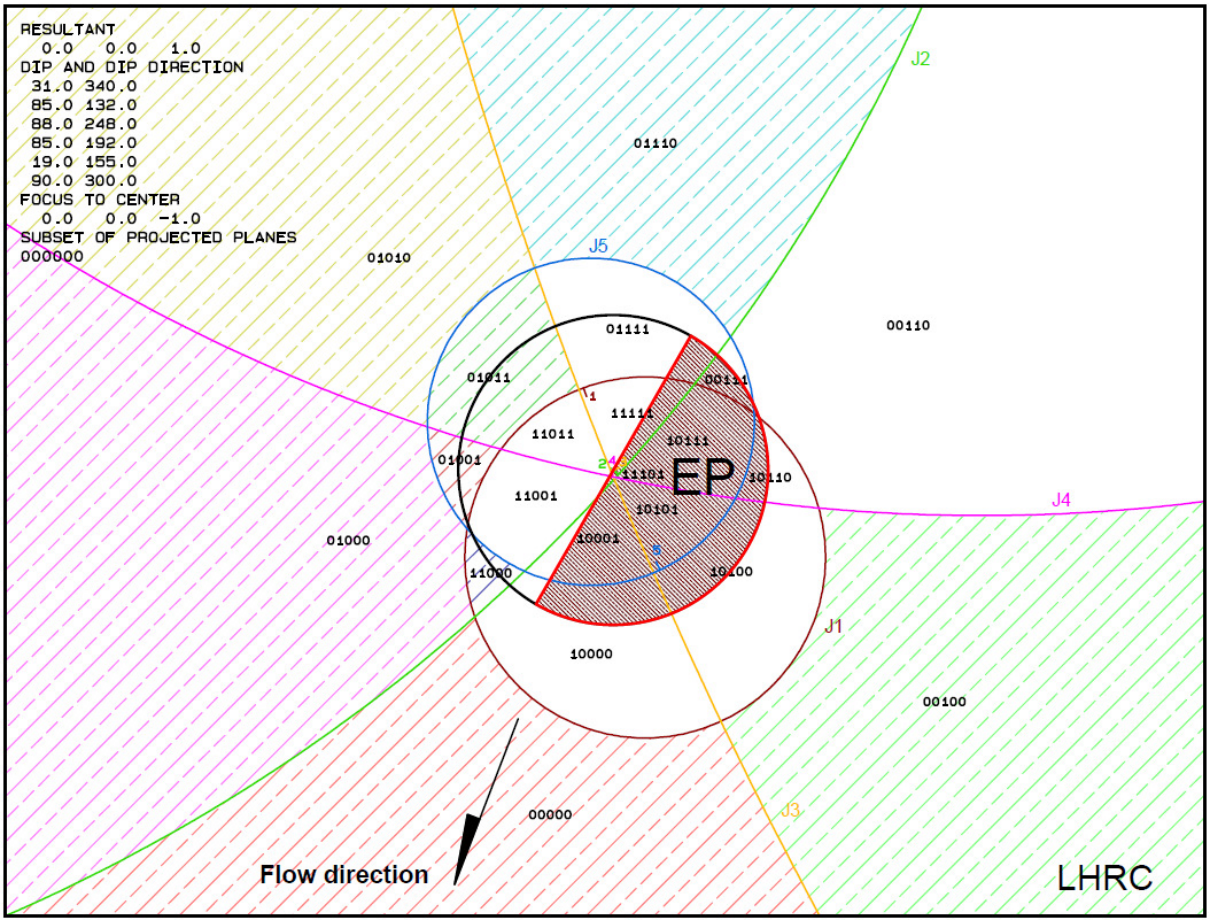

Figure 7.11 – Block removability – Left wall compound slope

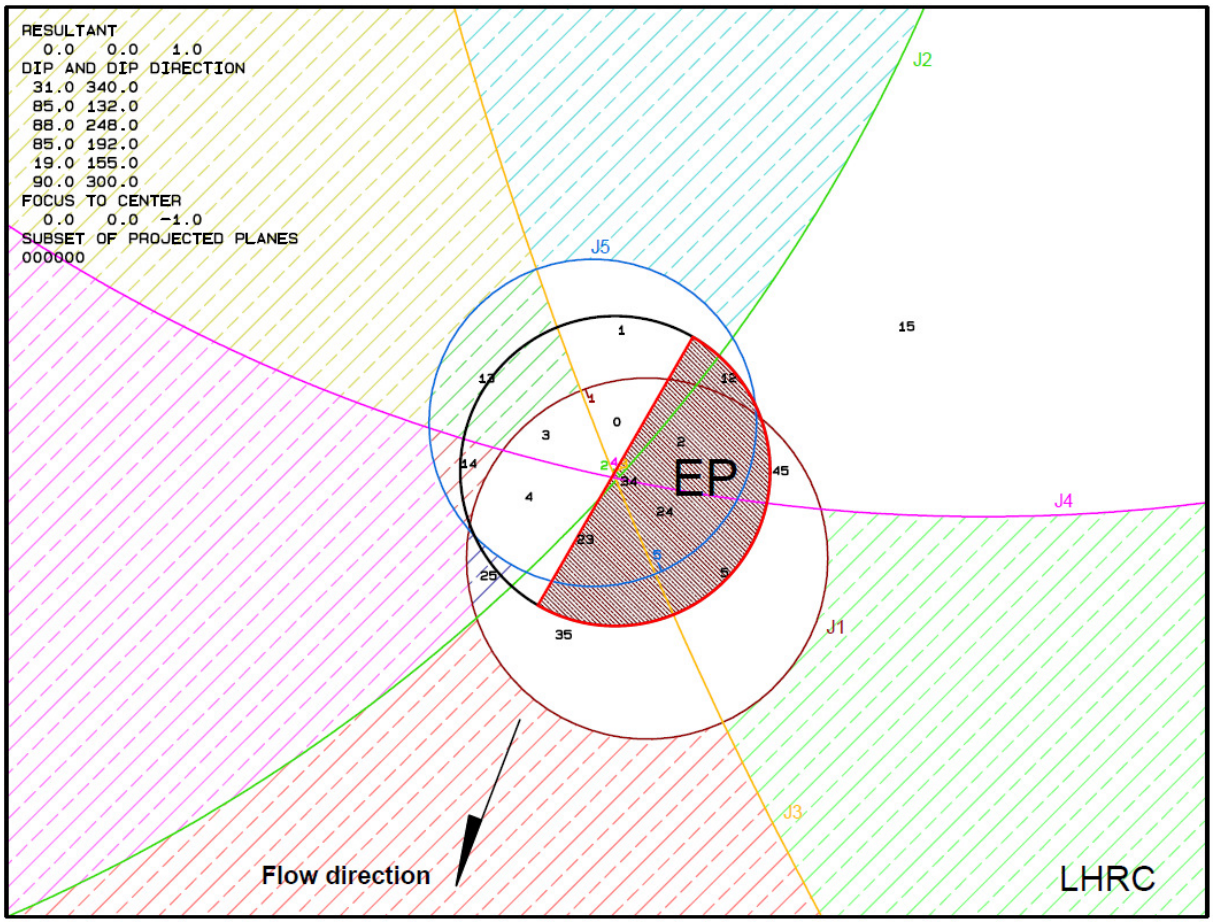

Figure 7.12 – Mode analysis – Left wall compound slope

Removable block	Failure mode	Block Volume [m³]
JP00000	-	31,3
JP00010	-	18,0
JP00100	-	37,6
JP01000	-	21,1
JP01001	14	18,9
JP01010	-	14,9
JP01011	13	21,5
JP01110	-	45,2
JP11000	25	41,6

Table 7.6 – Block theory analysis – Left wall compound slope

From the total number of removable blocks, 6 are blocks type III, which would not represent stability concerns. Safety factor analyses of the remaining 3 removable blocks, presented in Table 7.7, show that no real key blocks are present on the left wall. The potential key blocks recognized are: JP01001 (failure mode 14), JP01011

(failure mode 13) and JP11000 (failure mode 25). Most critical in this case is JP01011 presenting the lowest safety factor (1,44).

Probabilistic study results are presented in Table 7.7, and graphically in Figure 7.13, for all possible wedge sliding modes and for sliding on plane 2, which in this case strikes almost parallel (±20°) to the wall.

Failure Mode	Block Theory	Probability of Failure					
	Dry	Dry			Filled		
	FS	Kinematic	Kinetic	Total	Kinematic	Kinetic	Total
	[-]						
2	Stable	0,224	1,000	0,224	0,224	1,000	0,224
12	Stable	0,437	0,268	0,117	0,431	0,564	0,243
13	1,44	0,963	0,229	0,221	0,963	0,595	0,572
14	4,25	0,808	0,062	0,050	0,808	0,232	0,187
15	Stable	0,500	0,038	0,019	0,500	0,152	0,076
23	Stable	0,411	0,894	0,368	0,411	0,956	0,396
24	Stable	0,420	0,725	0,304	0,420	0,902	0,382
25	8,49	0,471	0,058	0,027	0,474	0,273	0,130
34	Stable	0,459	0,771	0,354	0,457	0,929	0,425
35	Stable	0,139	0,017	0,002	0,139	0,055	0,008
45	Stable	0,259	0,006	0,002	0,261	0,059	0,015

Table 7.7 – Stability analyses summary – Left wall compound slope

The most critical failure mode recognized with probabilistic methods is failure mode 13, same obtained from deterministic block theory. These wedges are almost certainly removable, presenting a probability of kinematical instability of around 96%. The probability of kinetic instability is very sensitive to water in this case reaching almost 60% in wet conditions, resulting in a high probability of failure (~58%) for these wedges when water action is considered.

Failure modes involving steep joint sets (23, 24 and 34) present probabilities of failure around 40% for the left wall. These failure modes, as already mentioned, present high probabilities of kinetic instability (~80-95%), but for the left wall their kinematic situation is more favourable, with probabilities of kinematic instability ranging around 40 to 50%, what greatly reduces their probability of failure. That is also the case for sliding on plane 2, which presents around 22% probability of failure.

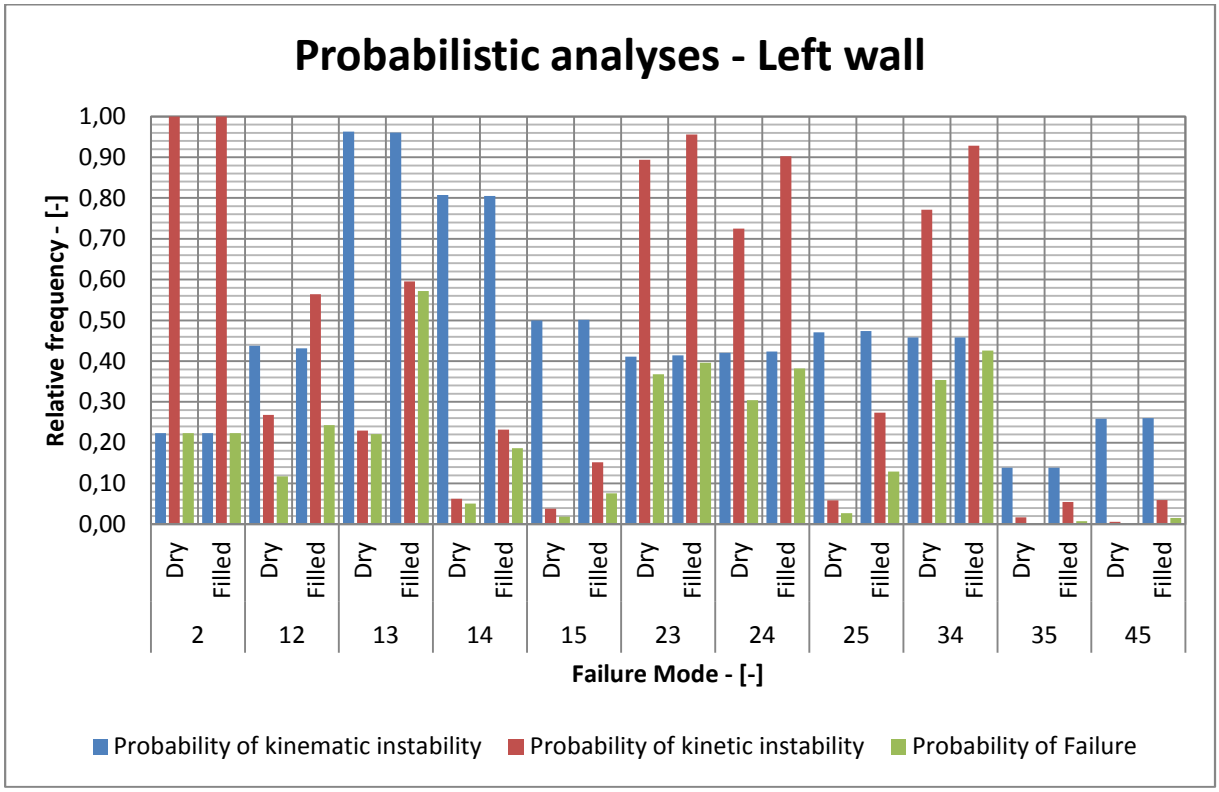

Figure 7.13 - Probabilistic analyses – Left wall compound slope

Other failure modes recognized from block theory (14 and 25) also do not present expressive probabilities of failure (around 18 and 12%, respectively). Their situation is distinct, wedges formed by joints 1 and 4 are most likely to be removable (~80%) but present low probability of kinetic instability (around 18% when filled). Failure mode 25 has a lower probability of kinematical instability compared to 14 (around 48%) and despite its higher probability of kinetic instability presents a lower total probability of failure.

The other failure modes present much lower probabilities of failure, less than 10%, and would not represent major stability concerns, except for failure mode 12 which reaches around 24% probability of failure in wet condition. The importance of joint set 1 for instabilities on the left wall becomes clear at this point.

The ratio of kinetic instability between dry and wet conditions is graphically presented in Figure 7.14. The same comments from the head wall are valid, but since joint set 1 is more important for the mechanical behaviour of the left wall and water has a greater influence on sliding blocks with lower plunge angles of the sliding direction,

the left wall appears more sensitive to water presence. Probability of failure also reflects this behaviour.

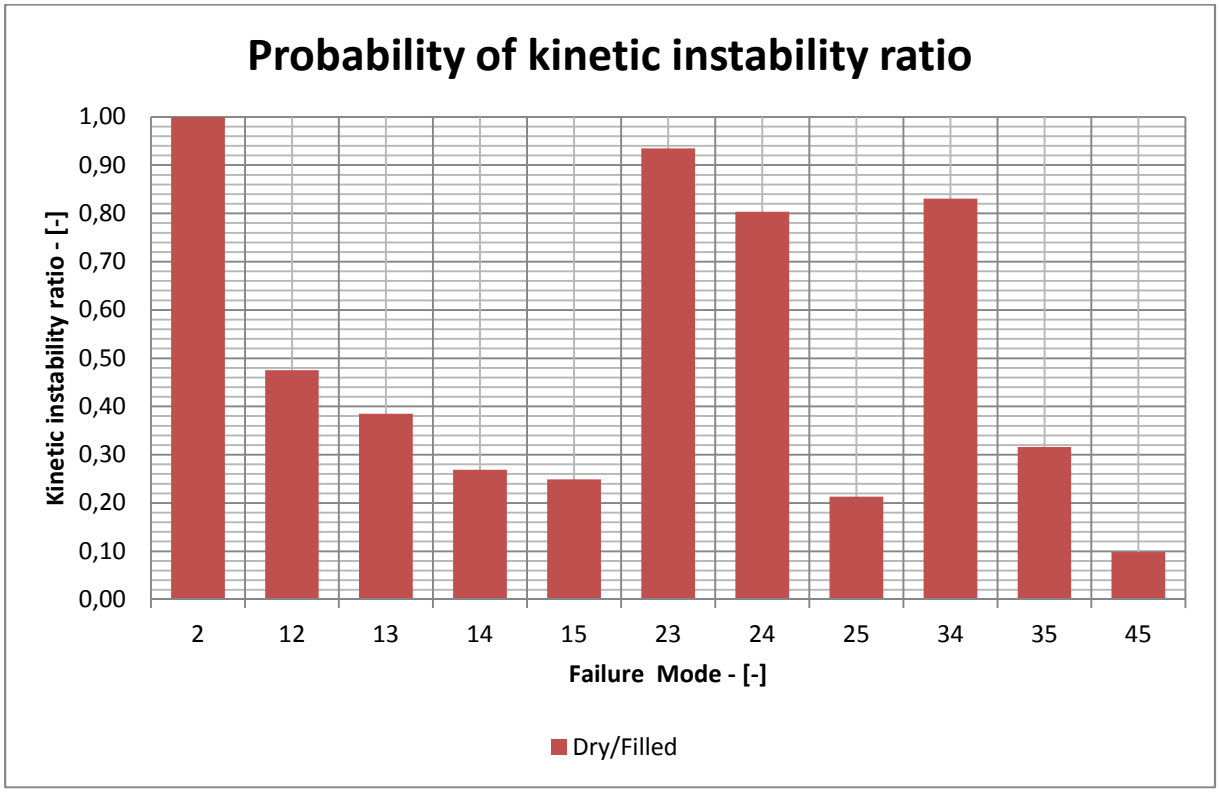

Figure 7.14 - Ratio of dry to filled probability of kinetic instability – Left wall compound slope

Block volumes obtained in the deterministic and probabilistic analyses are presented in Tables 7.5 and 7.7. Figure 7.15 graphically presents the results obtained from the software Swedge and RocPlane for the maximal block size. Rock volume involved is much larger than for the head wall. The reason for that is the size of the left side wall, which is much higher (at least 20m) and much longer than the constrained head wall. Most of these very large blocks have shown to be unlikely unstable, except for blocks formed by joint sets 1 and 3, which are large and critical for this slope.

The overall block system appears to behave in a stable manner with localized and isolated large block failures. Some large failure surfaces have been observed in the field, and appear be related to failure mode 13, as show in Figure 7.16.

Failure Mode	Probability Analysis					
	Dry			Filled		
	SE2	SE3	SE4	SE2	SE3	SE4
	[m³] or [m³/m]*					
2*	127	368	562	127	368	562
12	9054	13150	21458	9135	13019	21231
13	42808	88885	149115	42846	88962	149269
14	58385	101846	168808	58500	100962	167115
15	37104	40423	64385	37169	40730	64808
23	5312	16462	29253	5439	16835	29869
24	6927	21715	38454	7231	22604	40000
25	16365	23623	38415	16339	23562	38269
34	5012	22935	42769	5173	23881	44538
35	45385	57615	92539	43769	55423	89346
45	111000	181962	299115	110808	182000	299039

Table 7.8 – Mean block volume obtained from probabilistic analyses – Left wall compound slope.

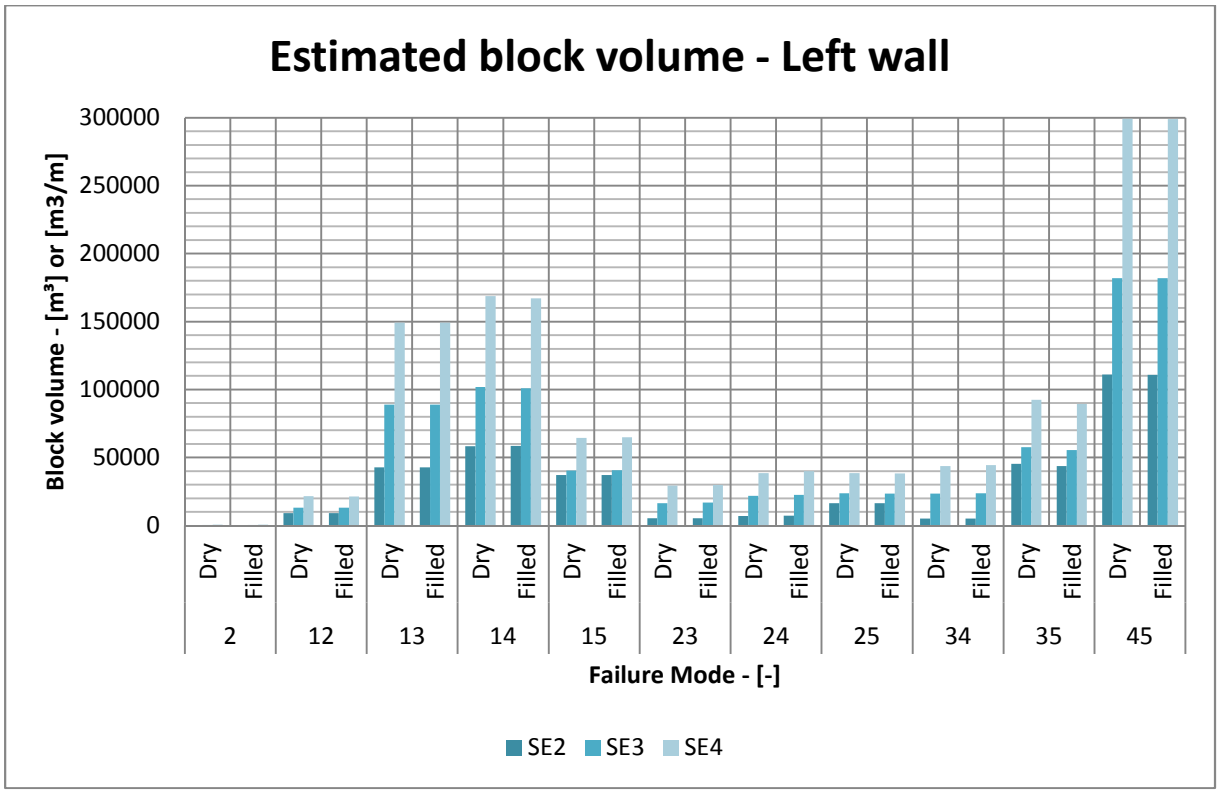

Figure 7.15 - Mean block volume obtained from probabilistic analyses – Left wall compound slope

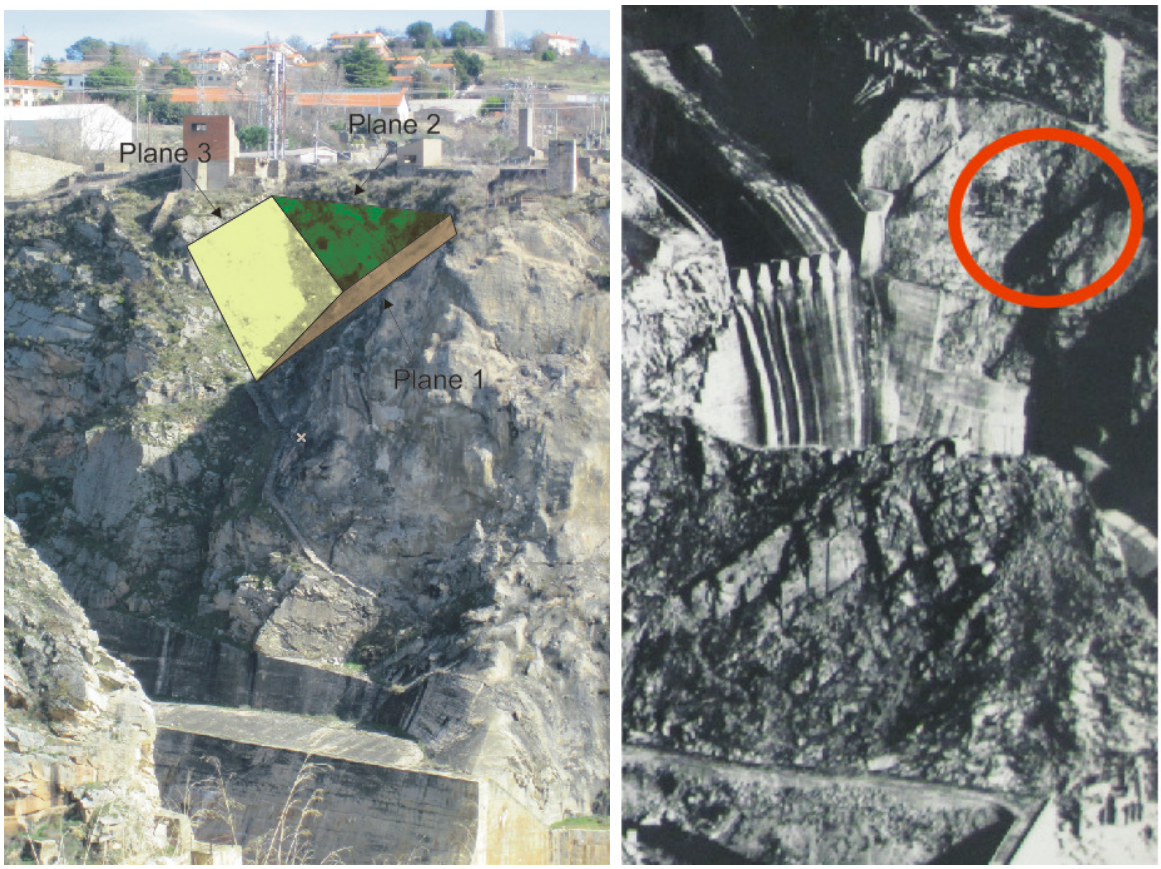

Figure 7.16 – Rock wedge moulds observed on the left wall

7.4 Right wall

The block removability analysis for the right wall of the Ricobayo plunge pool is presented in Figure 7.17. Removable blocks and the excavation pyramid (EP) are shaded. The right wall presents 13 removable blocks. The mode analysis performed for gravitational action only is presented in Figure 7.18 and summarized in Table 7.9, together with the block volumes obtained using joint set spacing presented in Table 7.2.

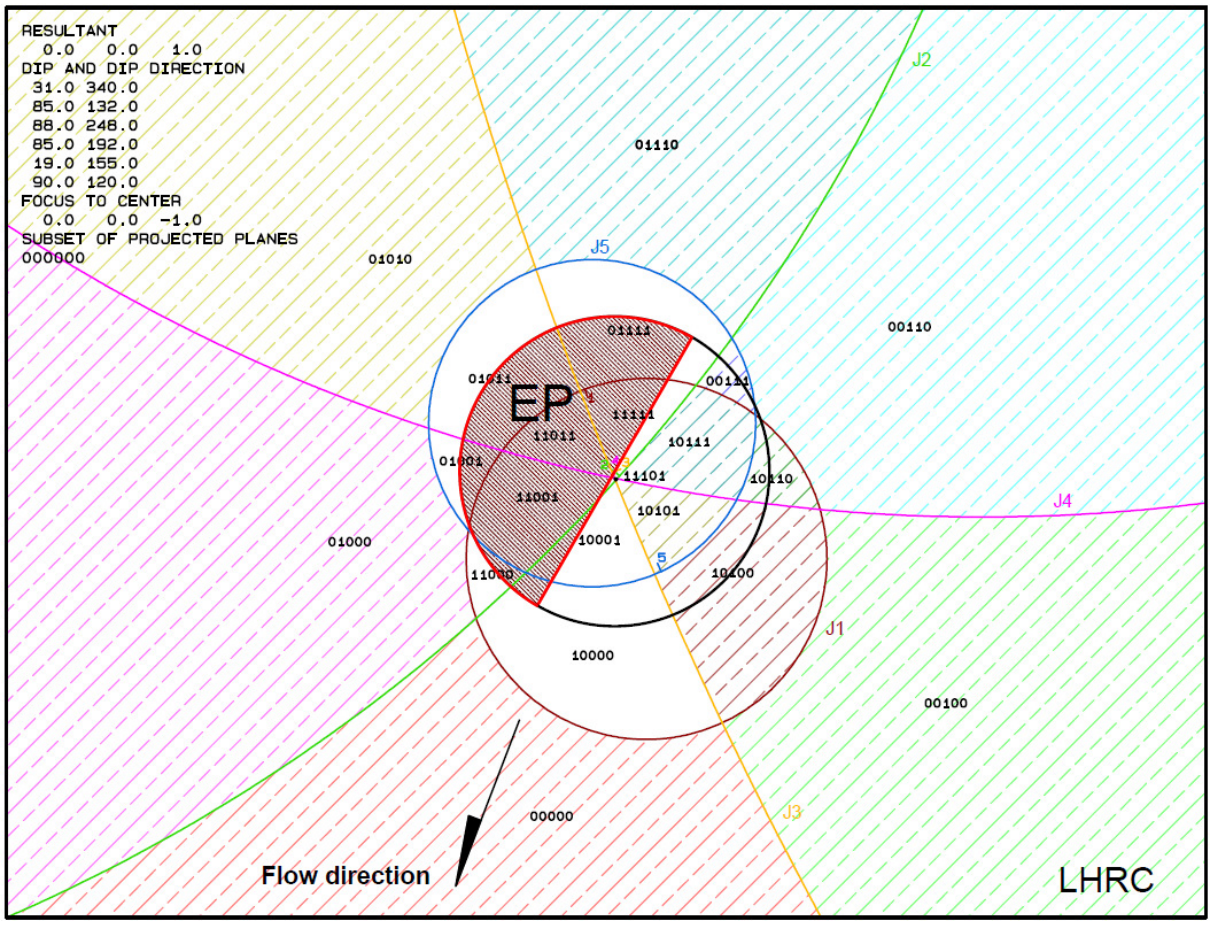

Figure 7.17 – Block removability – Right wall compound slope

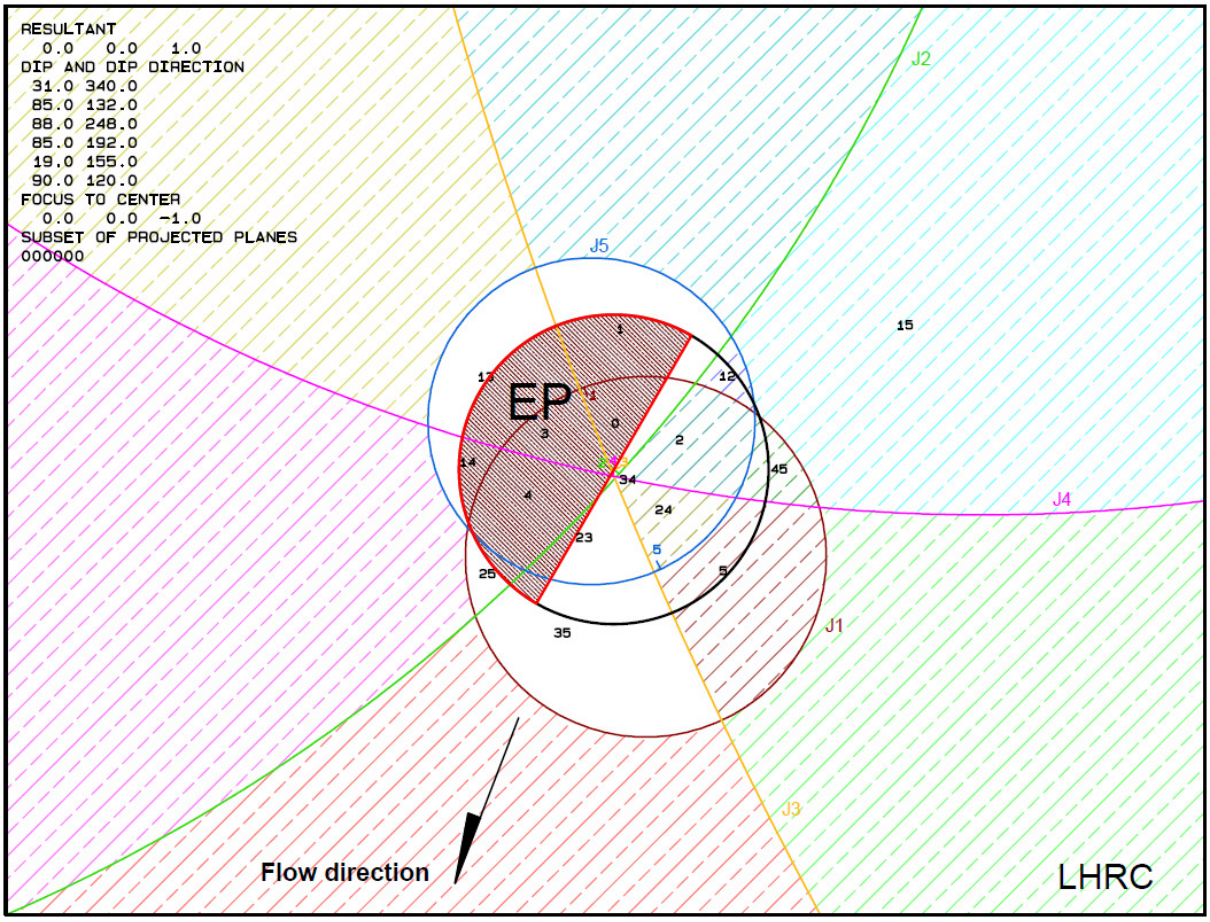

Figure 7.18 – Mode analysis – Right wall compound slope

Removable block	Failure mode	Block Volume [m³]
JP00000	-	33,7
JP00010	-	14,9
JP00100	-	15,0
JP00110	15	23,1
JP00111	12	50,5
JP01000	-	396,0
JP01010	-	41,0
JP01110	-	39,6
JP10100	5	17,0
JP10101	24	141,0
JP10110	45	16,6
JP10111	2	200,0
JP11101	34	354,0

Table 7.9 – Block theory analysis – Right wall compound slope

Stable blocks of type III represent almost half of the removable blocks (6 blocks). Remaining blocks present a failure mode; stability analysis in these cases is possible and necessary. The safety factors for these blocks are listed in Table 7.10. Results indicate 3 real key blocks with very low safety factors. JP's forming real key blocks are: JP10101 (mode 24), JP10111 (mode 2) and JP11101 (mode 34). All key blocks involve steep joints in this case. Potential key blocks presented in the right wall are not of primary concern since the safety factors calculated are quite high; JP10100 has the lowest value with 2,44.

Probabilistic analyses have been performed for all possible wedge sliding modes and for sliding on plane 2, which, also in this case, strikes nearly parallel to the wall (±20°). Failure mode 5 (plane sliding on joint set 5) has been recognized as admissible by deterministic block theory but has not been probabilistically studied. The reasons are the low probability of a joint trace striking parallel to the wall slope and the low dip angle of this plane (19°), which is much lower than the considered residual friction angle (30°). Results obtained from the probabilistic analyses are summarized in Table 7.10 and graphically presented in Figure 7.19.

Failure Mode	**Block Theory**	**Probability of Failure**					
	Dry	Dry			Filled		
	FS	Kinematic	Kinetic	Total	Kinematic	Kinetic	Total
	[-]						
2	0,07	0,297	1,000	0,297	0,297	1,000	0,297
5	2,44	-	-	-	-	-	-
12	4,90	0,563	0,110	0,062	0,569	0,309	0,175
13	Stable	0,037	0,116	0,004	0,037	0,124	0,005
14	Stable	0,184	0,005	0,001	0,184	0,042	0,008
15	48,21	0,502	0,032	0,016	0,502	0,180	0,090
23	Stable	0,589	0,854	0,503	0,589	0,939	0,550
24	0,10	0,580	0,782	0,453	0,580	0,921	0,531
25	Stable	0,529	0,194	0,103	0,526	0,502	0,264
34	0,10	0,541	0,727	0,393	0,543	0,919	0,499
35	Stable	0,861	0,102	0,088	0,861	0,375	0,323
45	5,27	0,737	0,047	0,035	0,739	0,201	0,148

Table 7.10 – Stability analyses summary – Right wall compound slope

The most critical failure modes resulting from the probabilistic analyses are involving steep joint sets. These are modes 23, 24 and 34, with probabilities of failure around 50 to 55% in wet conditions. Failure probabilities are not very sensitive to water and in these cases controlled by the probability of kinematical instability. This is clear for mode 23, which would not be identified with a classical block theory analysis using just the mean orientation vectors.

Three other failure modes present some stability concern; they are mode 2, 25 and 35. These failure modes have probabilities of failure around 30% in wet conditions. Failure mode 2 is controlled by its probability of kinematical instability, since once removable failure is certain (100%), no matter in what conditions. It has also been recognized using deterministic block theory (very low FS). Failure mode 25 is likely to be removed, around 50%, and has been identified deterministically. This mode is sensitive to water presence and probability of kinetic instability reaches 50% in wet conditions. The failure mode 35 could not be identified using mean orientation vectors with block theory; the mode is although very likely to produce a kinematically free block (~85%). Its stability is also very sensitive to water presence and probability of kinetic failure is around 32% in wet conditions.

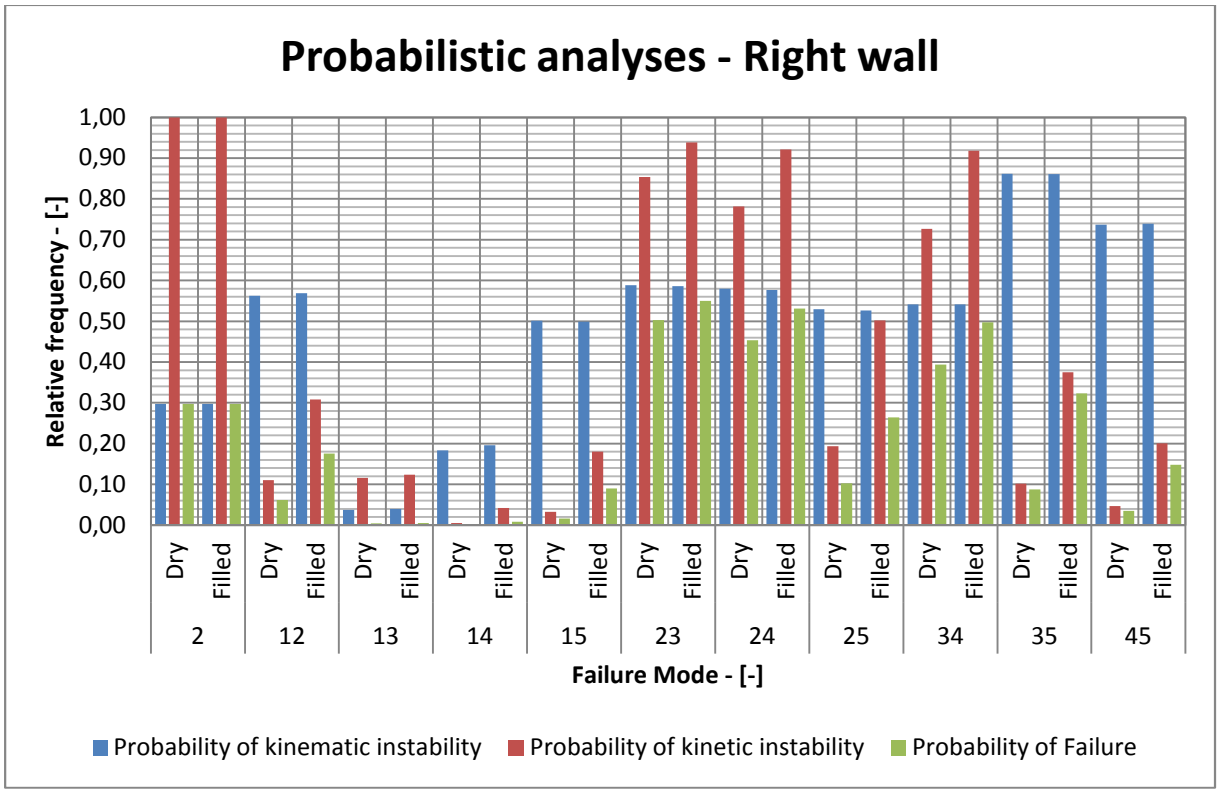

Figure 7.19 - Probabilistic analyses – Right wall compound slope

Of less importance are modes 12 and 45. These modes are recognized deterministically and a probabilistic approach also reflects that; their probabilities of kinematical instability are around 55 and 75% respectively. Probability of kinetic instability is less expressive ranging around 30% in wet conditions. The total failure probability ranges around 15 to 18% in wet conditions. Remaining failure modes are not of primary concern presenting probabilities of failure under 10%.

The ratio of kinetic instability between dry and wet conditions for the case of the right wall is graphically presented in Figure 7.20. For failure modes involving steep joint sets water does not have considerable influence; these blocks would fail even in dry conditions. The most critical blocks of the right wall belong to this case. That is not true for mode 12, 25, 35 and 45, which represent, not primary, but considerable stability concerns. Water presence may have triggered some of these failure modes, contributing to the overall instability of the right wall slope.

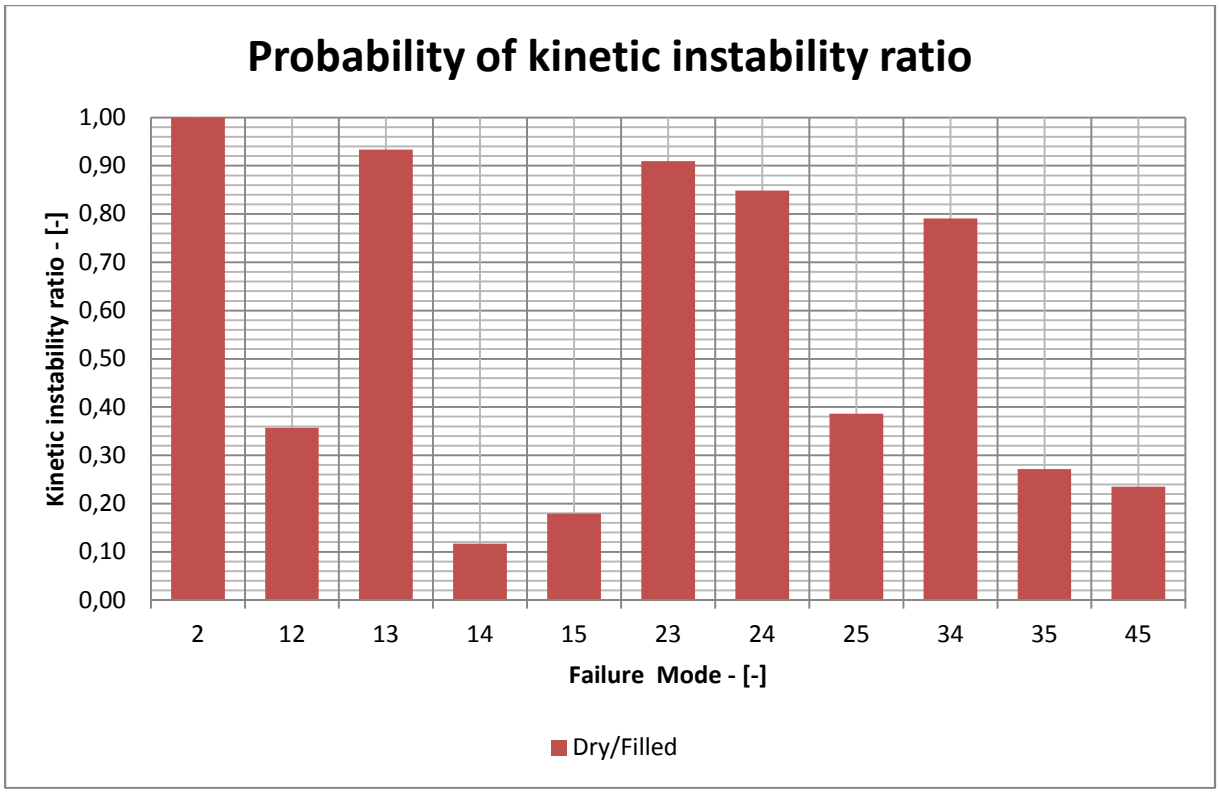

Figure 7.20 – Ratio of dry to filled probability of kinetic instability – Right wall compound slope

Block volumes obtained for average spacing are presented in Table 7.9, and the maximal block volumes in Table 7.11 and Figure 7.21. The block volumes obtained for the right wall are much smaller than those of the left wall. This wall is not as high

as the left wall (20m less than the left wall), but it seems that the nature of the probable removable blocks control the block volumes. Blocks most likely to be removed involve joint set 2, which is nearly parallel to the slope; this factor may contribute to constrain the block formation close to the wall. In this way the block would not extend much further behind the slope face, resulting in smaller volumes. The largest blocks indicated are most likely to be safe (modes 14 and 45), but mode 35 may represent a very large failure mechanism with potentially large rock mass involved. The slope is nevertheless most likely to behave as a block system controlled by steep joint sets.

Failure Mode	Probability Analysis					
	Dry			Filled		
	SE2	SE3	SE4	SE2	SE3	SE4
	[m³] or [m³/m*]					
2*	47	223	381	47	223	381
12	8208	21804	37750	8239	21608	37385
13	26104	44500	74154	26708	52500	88231
14	46923	160000	288654	48539	160577	288962
15	20046	29762	48385	19854	29269	47462
23	2265	12000	23700	2310	12258	24292
24	2658	14685	29065	2715	15108	29881
25	6965	12881	21385	6885	12923	21492
34	1323	12685	27935	1332	12731	28108
35	20712	61615	108885	20735	61692	108923
45	31827	77308	132846	32154	81500	139769

Table 7.11 – Mean block volume obtained from probabilistic analyses – Right wall compound slope.

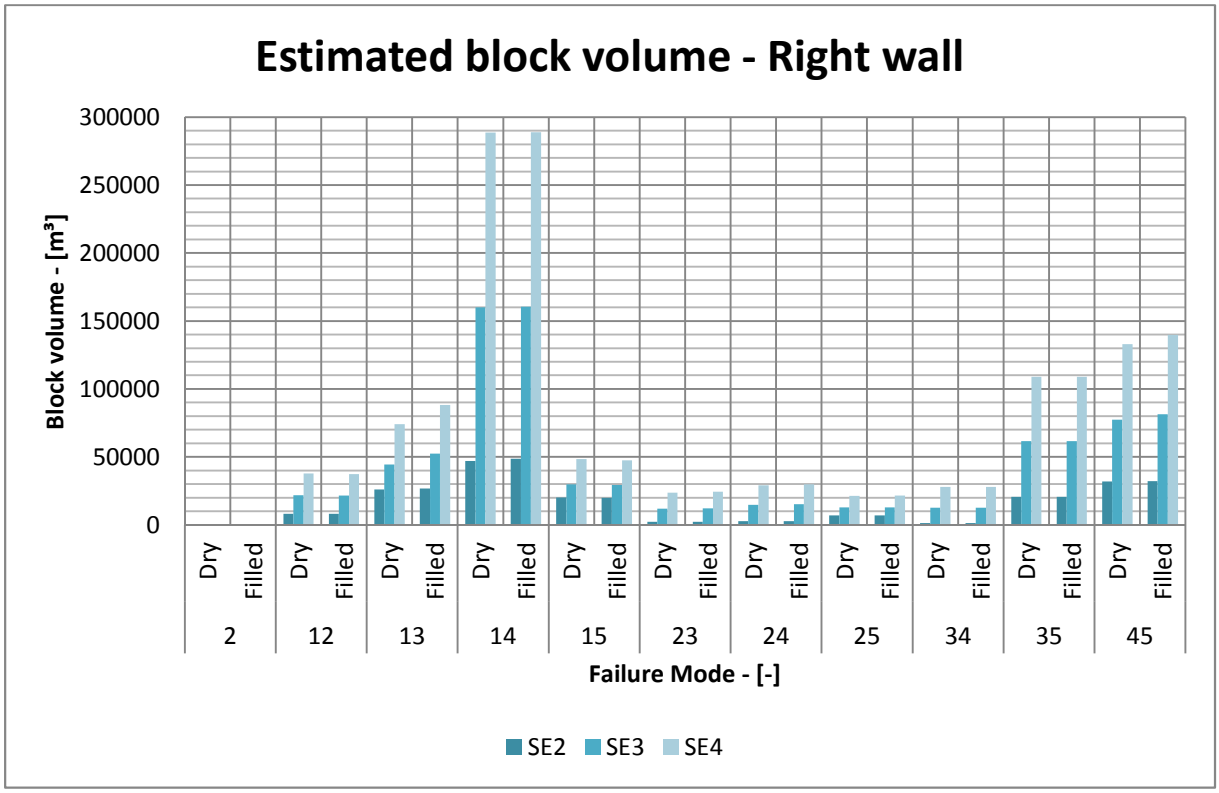

Figure 7.21 - Mean block volume obtained from probabilistic analyses – Right wall compound slope

8 Conclusion

The Ricobayo Dam is founded on a granitic rock body called the Ricobayo Massif. This plutonic intrusion occurred, according to literature research, during the third phase (D_3) of the Variscan Orogeny (380 to 280Ma). The Ricobayo Massif is imprinted by this deformation event (D_3) and by a syntectonic shear zone called the Villalcampo shear system. Structural measurement around the dam site indicated two discontinuity sets (3 and 4) with the geological characteristics similar to the NW-SE trending tectonic foliation mentioned in the literature. The Ricobayo granitoid is also described as bearing two micaceous minerals. These kinds of minerals are easily orientated through deformation, and produce preferential planes for discontinuity formation (cleavage). These two factors (tectonic deformation and mineral alignment) may have contributed to the formation of penetrative jointing in this granitic rock mass.

Engineering rock mass characterization performed shows a blocky/tabular rock mass. Five joint sets have been recognized with set spacing ranging around 1 to 2m. Discontinuities have shown to be highly persistent, but no major faults have been observed. Joints are mainly planar with some roughness, and joint set 1 is slickensided. Strong weathering has been observed close to the surface, but low weathering grades (II) prevail throughout the site. According to this information and field descriptions, strength of discontinuity walls could be related to that of the intact rock, which is reported ranging from 79 to 128 MPa with 100 MPa mean value. Discontinuities are closed underground and may be slightly open at the surface, except in areas where instabilities have been observed. In these cases joints are clearly open. Infilling has been observed close to the surface, originated most likely from intact rock weathering, although the general situation is of clean joints, occasionally with disintegrated rock. Water is present at the surface, and minor streams reach the Esla River, but no major seepage or water flows have been observed (also underground). The rock mass is characterized by large rock blocks (up to or larger than 8 m^3). Joint peak friction angles have been estimated around 40° (±2°); friction vary slightly between joint sets but is very much alike, for this reason was assume equal for all joint sets for stability analyses purposes.

The mechanical behavior of the head and side walls of the plunge pool during scour is believed to relate to the rock mass conditions and also to some construction aspects.

The head wall stability analysis shows a poor static behavior for a steep slope with this orientation. Deterministic block theory analysis, using mean joint set orientations, results in recognition of three real key blocks with very low factors of safety, all three involving steep joint sets. Probabilistic analyses, compatible with block theory but considering only discontinuities directly involved in failure, have been carried out for dry and wet conditions. They also show a poor situation for the head wall; four failure modes are critical (4, 23, 24 and 34), presenting high probabilities of failure (ranging from 50 to 60% in wet conditions), and an expressive volume gain when relief grows, but water does not much influence failure, since these mechanisms are related to very steep sliding directions. In this matter Failure is controlled by kinematics; the blocks fail as soon as free space is given. In this configuration scour played a central role by releasing these blocks. After scour event 1 the head wall was formed, providing free space for these kinds of block to move. Head wall back migration developed until March 1934 (Scour event 2). The largest involved blocks seemed to be removed and the slope achieved a stable situation. After that, water flow diminished, and may have not been enough to trigger any major failure. During summer of 1934 the head wall and spillway surfaces have been protected by concrete lining. Scour event 3 is also characterized by back migration of the head wall, but not where protection was built. A second level has been back eroded until the river level was reached. The back migration was apparently constrained by the head wall protection. At this point scour concentrated on the plunge pool bottom. Relief was accumulated during 1935 and especially during scour event 4 in 1936. During this process, free space has been given and it seems that a large block was released destroying the head wall protection and initiating the back migration again. The failure surface observed after this event is very steep, what allows failure relation to steep joint sets. Other failure modes presenting stability concerns are modes 14, 35 and 45 (probabilities of failure ranging from 20 to 33%). These blocks are very sensitive to water presence and their failure may have also helped to undermine the overall slope safety enlarging the rock mass volume involved.

Stability analyses performed for the left side wall of the plunge pool show a better condition. This is also supported by observations made at site and information documented during the scour process. The left wall did not suffer much during scour, no major failures have been reported, and today the situation appears much more stable in this wall. No real key blocks have been recognized on the left wall by deterministic block theory. The most critical block presents a failure mode on the intersection between joint sets 1 and 3. Its safety factor is 1,44. This failure mode has also been recognized as the most critical when parameter variability is taken into account. Its probability of failure reaches about 58% in wet conditions. These blocks are likely to be removed and are sensitive to water presence; some large wedge moulds are seen throughout the left wall and are related to this failure mode. Wedges formed involving steep joints (23, 24 and 34) are also a considerable concern. These failure modes cannot be identified using deterministic methods. Their probability of failure is around 40%, and they are largely controlled by kinematics (this may also be the case for sliding on plane 2 ($P_f \sim 20\%$)). These blocks present a medium probability of kinematical instability, but steep block moulds may also be observed along the left wall. Of the remaining failure modes, 14 and 25 are the only ones with probability of failure over 10%. The left wall appears much more stable and sensitive to water action; its behavior is one of a stable block system with isolated large block failures.

The right wall presents an intermediate situation between the left and head wall. Its behavior is, although much more similar to that of the head wall. Deterministic block theory yields 3 key blocks with low safety factors, all related to steep joint sets. Probabilistic analyses show the failure modes 23, 24 and 34 to be the most critical. Mode 23 is not present in deterministic analyses. These failure modes present a probability of failure around 50 to 55%, and are largely controlled by kinematics. Secondary failure modes recognized are 2, 25 and 35, with probabilities of failure around 30%. Sliding on plane 2 is a critical failure mode indicated by deterministic analysis, but shows to be kinematically controlled. Modes 25 and 35 are likely to be removable with a better static situation, but are very sensitive to water presence. Failure modes 12 and 45 are also concerning, with probabilities of failure around 15 and 18%. Most of the above-mentioned failure modes (12, 25, 35 and 45) are not of primary concern, but show to be very sensitive to water presence and may have also

been involved in overall failure. The right wall presents a situation comparable with the head wall: its behavior is expected to be as an unstable block system controlled by steep joint sets. This may be the reason why most action was concentrated in scour events 3 and 4. During this period, the scour occurred mainly at the plunge pool bottom. As the plunge pool was eroded down, free space was given for blocks with steep sliding directions to move and eventually trigger failure modes involving more rock volume. This resulted in large slope failures on the right wall during scour events 3 (1935) and 4 (1936)

The results and conclusions about the response of the Ricobayo Dam plunge pool walls are strongly supported by the current morphology of the plunge pool. Figure 8.1 illustrates the present form of the plunge pool. The colored lines are lineaments suggested by the form of the plunge pool and their colors suggest the joint set to which they are related. Together with this information a symbol with the mean strike and dip, proposed by this work for these joint sets, is presented. The symbol is used to represent vertical or nearly vertical jointing and is oriented exactly with the mean orientation calculated with the field measurements performed by the author. The depicted joint sets are steep sets 2, 3 and 4. As discussed they represent the controlling structures at site, together with joint set 1, which may be observed on the left wall.

The present work and its analyses showed a poor static situation for the head- and sidewalls of the Ricobayo Dam plunge pool. The rock mass conditions and geometric characteristics of the walls were summed to produce a rapid and large scour event; involving back migration of the head wall and large failures of the side slopes of the spilling channel, resulting in the formation of the Ricobayo plunge pool. The performed rock mass characterization showed to be effective in describing the rock mass behavior. The chosen analytical method, block theory, proved to be a powerful tool to enhance analyses of scour related processes in blocky rock masses, especially when performed in a probabilistic manner. Deterministic analyses are great indicators of static behavior but are not able to take parameter variability into account. This has been shown in this case, where kinematics play in important role on the process and orientation measurements are largely scattered.

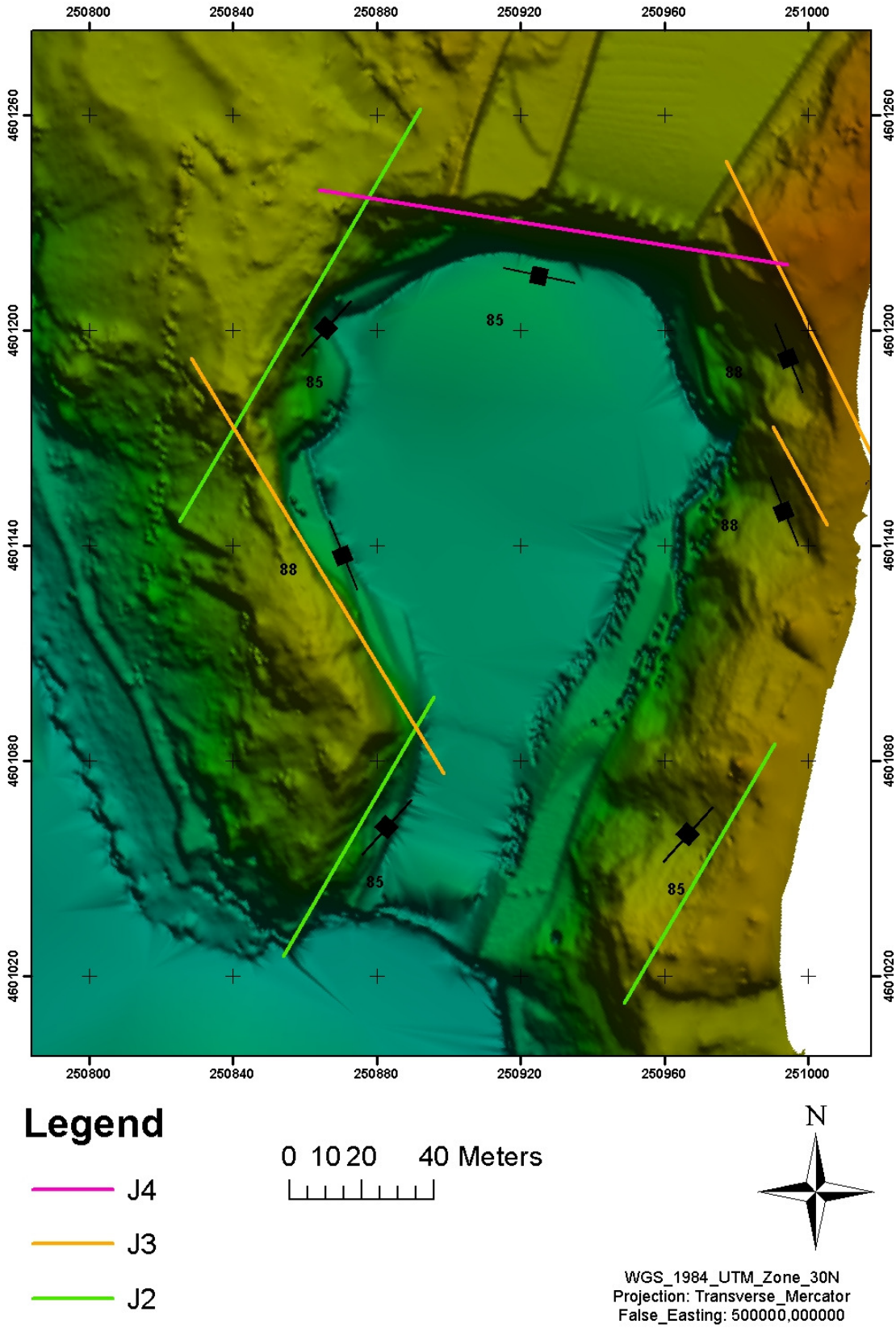

Figure 8.1 – Ricobayo Dam plunge pool

References

Annadale, G. W. (2006). Scour Technology, 1st Ed., McGraw-Hill, New York.

Barton, N.R. (1973). Review of the shear strength criterion for rock joints. Eng. Geol. 7, 287-332.

Barton, N.R. (1976). The shear strength of rock and rock joints. Int. J. Mech. Min. Sci. & Geomech. Abstr. 13(10), 1-24.

Barton, N.R. and Bandis, S.C. (1982). Effects of block size on the shear behavior of jointed rock. 23rd U.S. symp. on rock mechanics, Berkley, 739-760.

Barton, N.R. and Choubey, V. (1977). The shear strength of rock joints in theory and practice. Rock Mech. 10 (1-2), 1-54.

Bollaert, E. and Schleiss, A. (2005). Physically based model for evaluation of rock scour due to high-velocity jet impact. Journal of Hydraulic Engineering, vol. 131 (3).

Del Aguila, A. (1933). “Algunas consideraciones sobre el régimen hidráulico al pie de presas y su aplicación a los ensayos del vertedero del Esla – Primera serie de ensayos.” Revista de Obras Públicas, n° 2627, p. 349 – 357, Madrid.

Del Aguila, A. (1933). “Algunas consideraciones sobre el régimen hidráulico al pie de presas y su aplicación a los ensayos del vertedero del Esla – Segunda serie de ensayos.” Revista de Obras Públicas, n° 2629, p. 397 – 403, Madrid.

Einstein, H.H. (1996). Risk and risk analysis in rock engineering. Tunn. Undergr. Space Technol., 11 (2), 141-155.

Escuder Viruete, J. (1998). “Relationships between structural units in the Tormes gneiss dome (NW Iberian Massif, Spain): geometry, structure and kinematics of contractional and extensional Variscan deformation.” Geologische Rundschau, v. 87, p. 165-179.

Esri Inc. (2009). ArcMap 9.3.1, User's Manual, Redlands.

Fernández-Aláez, M. et al. (1992). "The Esla River basin: From the Cantabrian mountain to the Duero." Limnetica, v. 8, p. 131-140, Madrid.

Fernández-Turiel, J. L. (1985). "Aspectos geológicos y metagenéticos del batolito de Ricobayo y complejo de Villaseco-Peruela y sus mineralizaciones estanníferas asociadas (Zamora)." Doctoral dissertation, Universidad de Barcelona, Barcelona.

Fernández-Turiel, J. L. (1990). "Lithogeochemical exploration in a Hercynian Tin-Bearing Batholith in the Northwest of the Iberian Peninsula." Acta Geológica Hispánica, v. 25, n°3, p. 177-183.

Fernández-Turiel, J. L. et al. (1990). Lithogeochemical exploration in a Hercynian Tin-Bearing Batholith in the Northwest of the Iberian Peninsula. Acta Geologica Hispanica, vol 25, n° 3, pag. 177-183.

González Clavijo, E. et al. (1991). "La cizalla de Villalcampo (Zamora), geometría cinemática y condiciones de la deformación asociada." Cuaderno Lab. Xeolóxico de Laxe, v. 16, p. 203-219, Coruña.

González Clavijo, E., and Martínez Catalán, J. R. (2002). "Stratigraphic record of preorogenic to synorogenic sedimentation, and tectonic evolution of imbricate units in the Alcañices synform (northwestern Iberian Massif)." Geological Society of America, Special paper 364, p. 17-35, Boulder, Colorado.

Goodman, R. E. (1989). Introduction to rock mechanics, 2nd Ed., Wiley, New York.

Goodman, R. E., and Kieffer, D. S. (2000). "Behaviour of rock in slopes." Jour. Geotech. And Geoenvir. Engrg., ASCE, vol 126, n°8.

Goodman, R. E., and Shi, G. H. (1985). Block theory and its applications to rock engineering, Prentice-Hall, Engelwood Cliffs, N. J.

Goodman, R. E., and Shi, G. H. (1989). Block theory software package. University of California, Berkeley.

Guía Técnica de Seguridad de Presas, nº5 – Aliviaderos y Desagües, 1997 (reimpr. 2003). Anexo nº7 – Aliviadero del Esla

Hoek, E. (2007). Practical rock engineering - Lecture notes. RocScience.

Hoek, E., and Bray, J. W. (1981). Rock slope engineering, 3rd Ed, Inst. of Mining and Metallurgy, London.

Iberdrola, S. A.. Salto de Ricobayo II – Caracteristicas geologicas y geotecnicas.

Iberduero, S. A. (1947). Proyecto reformado del de consolidación del aliviadero del Esla. Anexos 3, 4, 6 y 8.

Iberduero, S. A. (1961). Informe sobre el canal inferior de aliviadero "Cazuela". Salto del Esla.

Iberduero, S. A. (1966).Información reparación muros embalse y derrumbamiento muro en salida emisario en el Salto del Esla". Esla.

Iberduero, S. A.. Información de los desprendimientos producidos en el canal inferior aliviadero del Esla, durante los meses invernales 1959-1960.

Iberduero, S. A.. Salto de Ricobayo – Aliviadero.

ISRM (1981). ISRM Suggested Methods, Rock Characterization: Testing and Monitoring. Commission on testing methods ISRM, Pergamon Press, Oxford.

Park, H. (2005). Probabilistic analysis of rock slope stability and random Properties of discontinuity parameters, Interstate Highway 40, Western North Carolina, USA. Engineering Geology, 79, 230-250.

Park, H. et al. (2006). The evaluation oft he probability of rock wedge failure using the point estimate method and maximum likelihood estimation method. Geological Society of London. IAEG, paper number 485.

Porsche-Ully, N. (2001). Sphaira 2.0, User's Manual, Salzburg.

RIEGL LMS GmbH (2009). RiSCAN PRO 1.5.2sp2, User's Manual, Horn.

Riesco Chueca, P.. "El embalse de Ricobayo y la visita en 1934 de Theodor Rehbock." Universidad de Sevilla.

RocScience Inc. (2001). RocPlane 2.0 – Planar Sliding Stability for Rock Slopes, User's Manual, Toronto.

RocScience Inc. (2011). Swedge 5.0 - 3D Surface Analyses for Slopes, User's Manual, Toronto.

Wittke, W. (1965). "Methods to analyse the stability of rock slopes with and without additional loading." Rock mechanics and engineering geology, supplement 2, Springer, Vienna.

Wittke, W. (1984). Felsmechanik. Springer-Verlag Berlin, Heidelberg.

Wyllie, D.C. and Mah, C.W. (2004). Rock slope engineering, 4rd Ed, Taylor & Francis, London.

APPENDIX

In this appendix the results of the outcrop mapping performed with the photogrammetric software ShapeMetrix^{3D} are presented. Ten outcrops have been analysed. The location of the outcrops is presented in the map. The structural sets are the same as suggested in chapter 6, the results vary a little, but as shown before the structural setting seems to be solid.

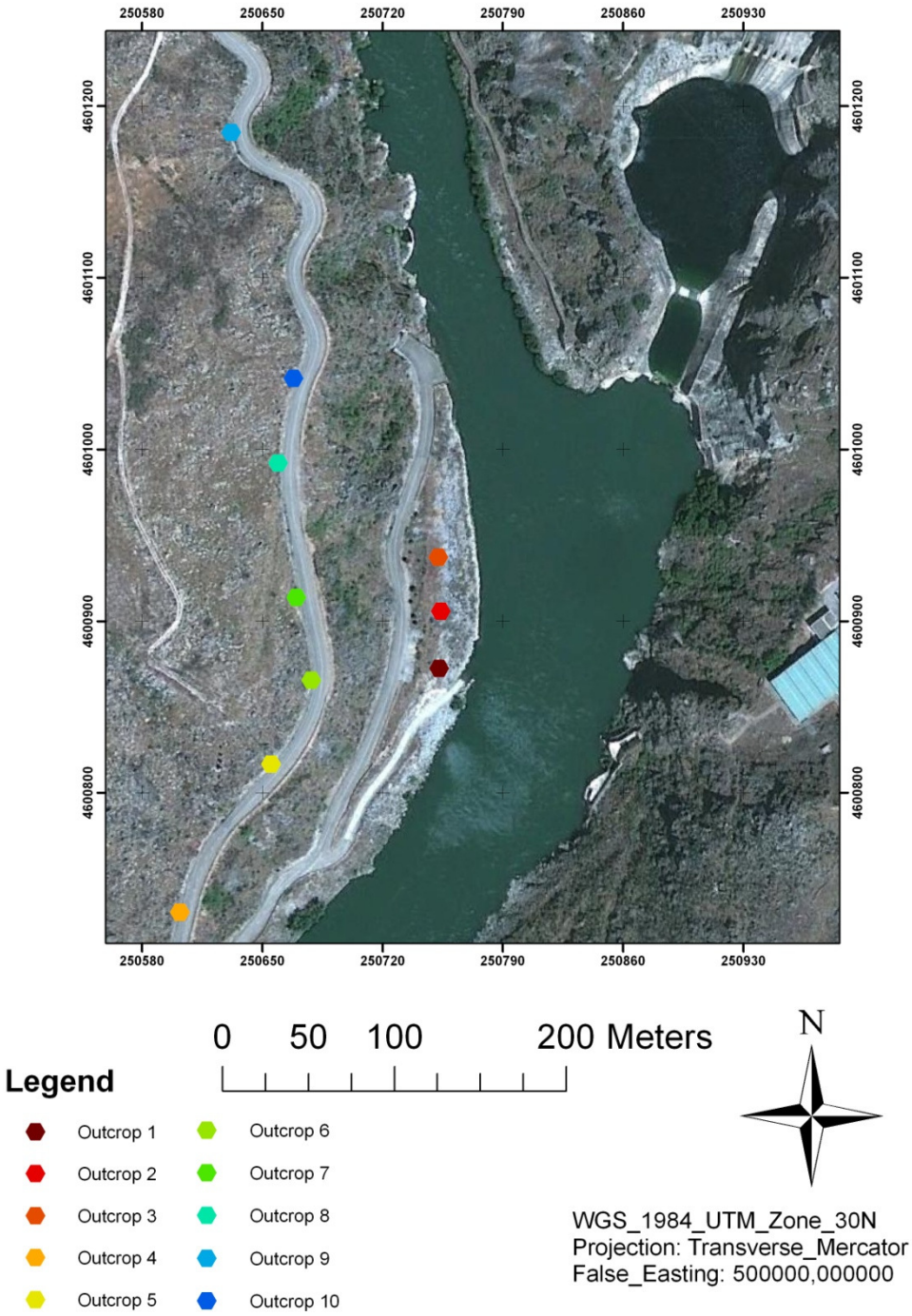

1. Outcrop 1

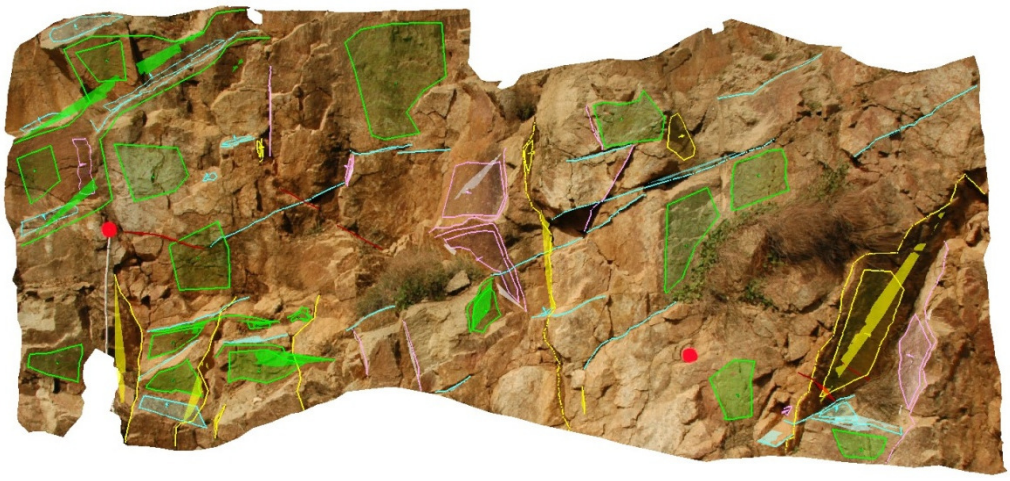

3D Model of Outcrop 1

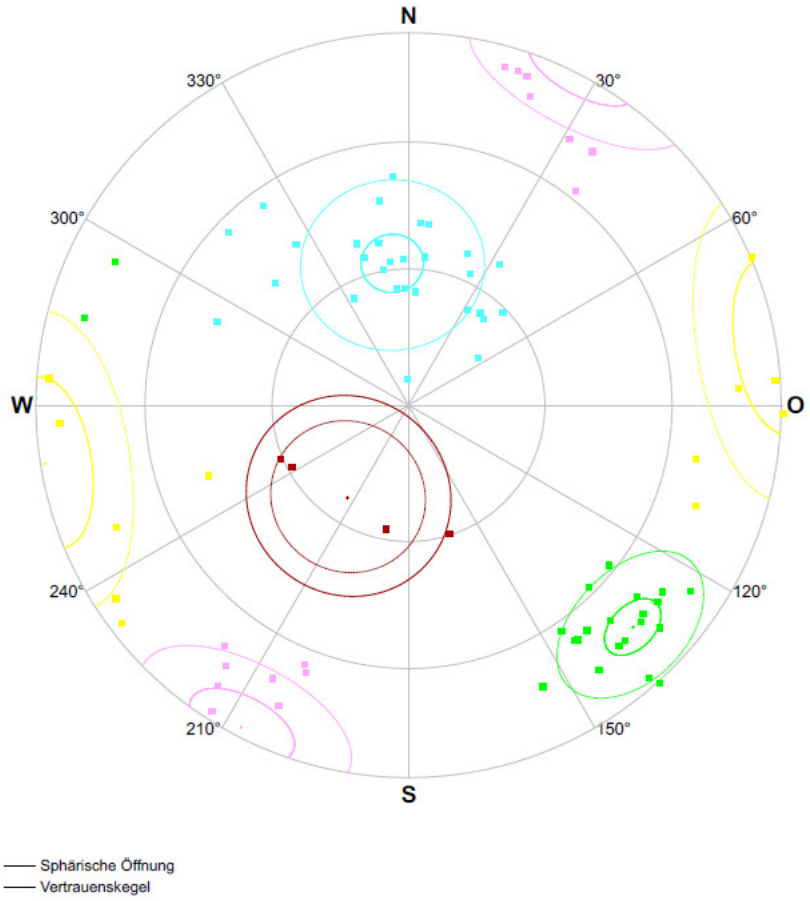

Orientation measurements of outcrop 1 (LHRC - Lambert projection).

- **Statistical details of structural set 1**

Orientation measurements parameters

Beschreibung	Wert	Einheit
Fallrichtung	33.45	°
Fallwinkel	24.29	°
Sphärische Öffnung	16.73	°
Konzentration	18.10	
Orientierungsgrad	91.71	%
Vertrauenskegel	22.19	°
Konfidenz	95.0	%
Anzahl an Orientierungsmessungen	4 / 4	

Trace measurements parameters

Beschreibung	Wert	Einheit
Anzahl an Trennflächenspuren	5	
Trennflächenfrequenz	1.9922	Trennflächenspuren/m
Mittelwert	0.50	m
Standardabweichung	0.05	m
Minimum	0.46	m
Maximum	0.54	m
Länge der Trennflächenspuren	3.05	m
Mittlere Länge der Trennflächenspuren	0.61	m
Standardabweichung der Länge der Trennflächenspuren	0.18	m
Länge der Kluftbrücken	0.00	m
Mittlere Länge der Kluftbrücken	0.00	m
Standardabweichung der Länge der Kluftbrücken	0.00	m

- **Statistical details of structural set 2**

Orientation measurements parameters

Beschreibung	Wert	Einheit
Fallrichtung	314.71	°
Fallwinkel	73.70	°
Sphärische Öffnung	15.26	°
Konzentration	27.62	
Orientierungsgrad	93.07	%
Vertrauenskegel	5.86	°
Konfidenz	95.0	%
Anzahl an Orientierungsmessungen	23 / 23	

Trace measurements parameters

Beschreibung	Wert	Einheit
Anzahl an Trennflächenspuren	6	
Trennflächenfrequenz	1.2885	Trennflächenspuren/m
Mittelwert	0.78	m
Standardabweichung	0.45	m
Minimum	0.25	m
Maximum	1.57	m
Länge der Trennflächenspuren	10.48	m
Mittlere Länge der Trennflächenspuren	1.75	m
Standardabweichung der Länge der Trennflächenspuren	1.34	m
Länge der Kluftbrücken	0.00	m
Mittlere Länge der Kluftbrücken	0.00	m
Standardabweichung der Länge der Kluftbrücken	0.00	m

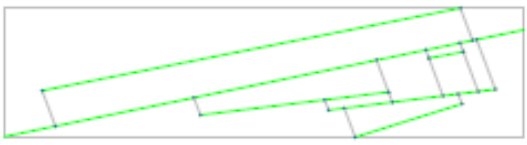

- **Statistical details of structural set 3**

Orientation measurements parameters

Beschreibung	Wert	Einheit
Fallrichtung	80.89	°
Fallwinkel	88.69	°
Sphärische Öffnung	23.68	°
Konzentration	11.37	
Orientierungsgrad	83.87	%
Vertrauenskegel	13.46	°
Konfidenz	95.0	%
Anzahl an Orientierungsmessungen	12 / 12	

Trace measurements parameters

Beschreibung	Wert	Einheit
Anzahl an Trennflächenspuren	9	
Trennflächenfrequenz	0.4942	Trennflächenspuren/m
Mittelwert	2.02	m
Standardabweichung	1.57	m
Minimum	0.14	m
Maximum	5.34	m
Länge der Trennflächenspuren	12.83	m
Mittlere Länge der Trennflächenspuren	1.43	m
Standardabweichung der Länge der Trennflächenspuren	1.22	m
Länge der Kluftbrücken	0.00	m
Mittlere Länge der Kluftbrücken	0.00	m
Standardabweichung der Länge der Kluftbrücken	0.00	m

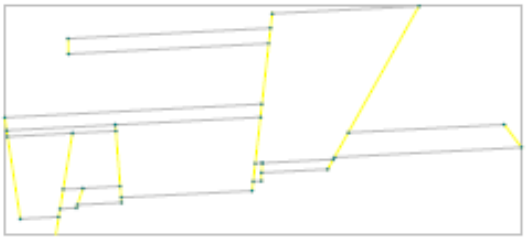

- **Statistical details of structural set 4**

Orientation measurements parameters

Beschreibung	Wert	Einheit
Fallrichtung	27.46	°
Fallwinkel	87.15	°
Sphärische Öffnung	18.31	°
Konzentration	18.91	
Orientierungsgrad	90.13	%
Vertrauenskegel	9.03	°
Konfidenz	95.0	%
Anzahl an Orientierungsmessungen	15 / 15	

Trace measurements parameters

Beschreibung	Wert	Einheit
Anzahl an Trennflächenspuren	9	
Trennflächenfrequenz	0.8100	Trennflächenspuren/m
Mittelwert	1.23	m
Standardabweichung	1.17	m
Minimum	0.00	m
Maximum	4.25	m
Länge der Trennflächenspuren	10.15	m
Mittlere Länge der Trennflächenspuren	1.13	m
Standardabweichung der Länge der Trennflächenspuren	0.69	m
Länge der Kluftbrücken	0.00	m
Mittlere Länge der Kluftbrücken	0.00	m
Standardabweichung der Länge der Kluftbrücken	0.00	m

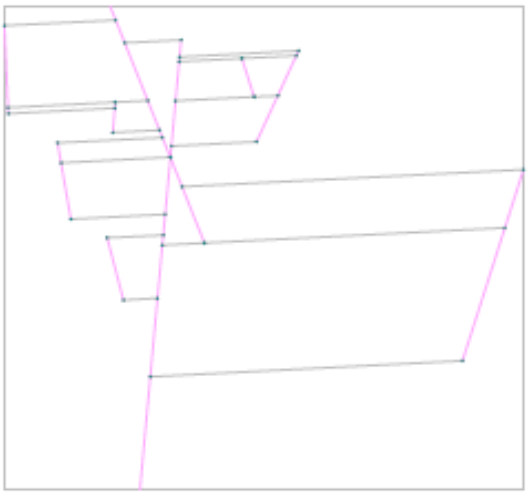

- **Statistical details of structural set 5**

Orientation measurements parameters

Beschreibung	Wert	Einheit
Fallrichtung	173.50	°
Fallwinkel	31.52	°
Sphärische Öffnung	19.37	°
Konzentration	17.56	
Orientierungsgrad	89.00	%
Vertrauenskegel	6.57	°
Konfidenz	95.0	%
Anzahl an Orientierungsmessungen	29 / 29	

Trace measurements parameters

Beschreibung	Wert	Einheit
Anzahl an Trennflächenspuren	21	
Trennflächenfrequenz	1.1361	Trennflächenspuren/m
Mittelwert	0.88	m
Standardabweichung	0.62	m
Minimum	0.00	m
Maximum	2.48	m
Länge der Trennflächenspuren	21.26	m
Mittlere Länge der Trennflächenspuren	1.01	m
Standardabweichung der Länge der Trennflächenspuren	0.57	m
Länge der Kluftbrücken	0.00	m
Mittlere Länge der Kluftbrücken	0.00	m
Standardabweichung der Länge der Kluftbrücken	0.00	m

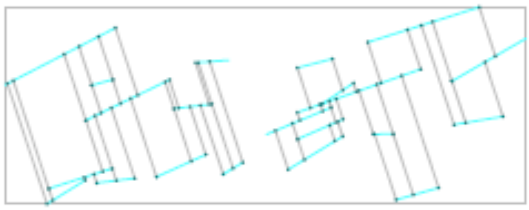

2. Outcrop 2

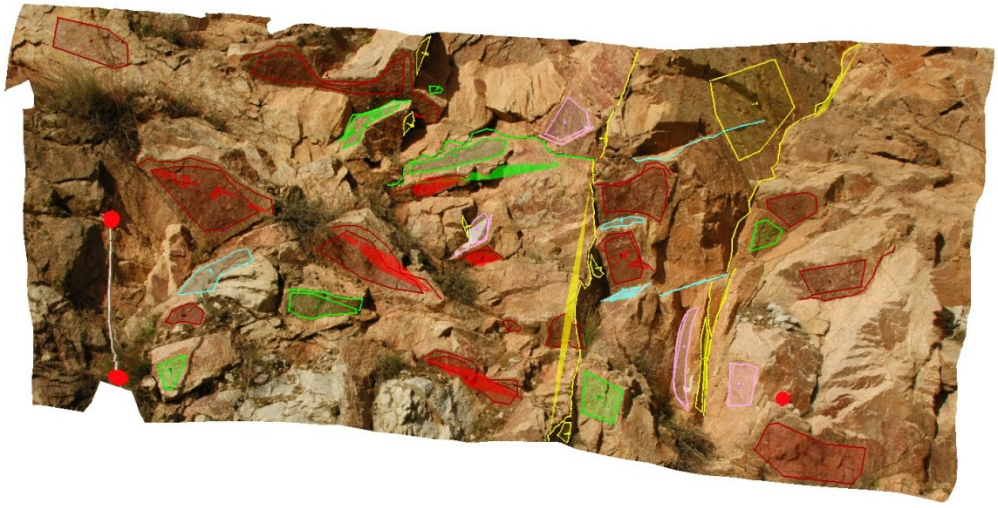

3D Model of Outcrop 2

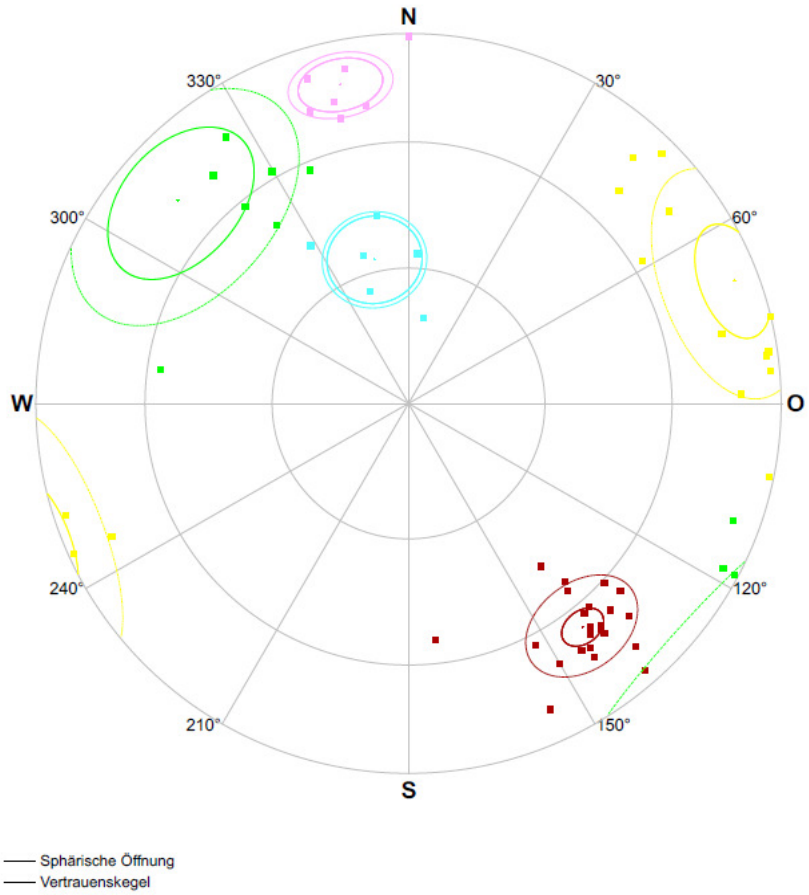

Orientation measurements of outcrop 2 (LHRC - Lambert projection).

- **Statistical details for structural set 1**

Orientation measurements parameters

Beschreibung	Wert	Einheit
Fallrichtung	322.30	°
Fallwinkel	65.47	°
Sphärische Öffnung	11.37	°
Konzentration	49.34	
Orientierungsgrad	96.12	%
Vertrauenskegel	4.25	°
Konfidenz	95.0	%
Anzahl an Orientierungsmessungen	24 / 24	

Trace measurements parameters

Beschreibung	Wert	Einheit
Anzahl an Trennflächenspuren	9	
Trennflächenfrequenz	1.6774	Trennflächenspuren/m
Mittelwert	0.60	m
Standardabweichung	0.34	m
Minimum	0.12	m
Maximum	1.23	m
Länge der Trennflächenspuren	10.22	m
Mittlere Länge der Trennflächenspuren	1.14	m
Standardabweichung der Länge der Trennflächenspuren	0.53	m
Länge der Kluftbrücken	0.00	m
Mittlere Länge der Kluftbrücken	0.00	m
Standardabweichung der Länge der Kluftbrücken	0.00	m

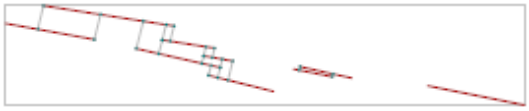

- **Statistical details for structural set 2**

Orientation measurements parameters

Beschreibung	Wert	Einheit
Fallrichtung	131.56	°
Fallwinkel	71.52	°
Sphärische Öffnung	24.51	°
Konzentration	10.46	
Orientierungsgrad	82.79	%
Vertrauenskegel	15.67	°
Konfidenz	95.0	%
Anzahl an Orientierungsmessungen	10 / 10	

Trace measurements parameters

Beschreibung	Wert	Einheit
Anzahl an Trennflächenspuren	3	
Trennflächenfrequenz	2.2827	Trennflächenspuren/m
Mittelwert	0.44	m
Standardabweichung	0.08	m
Minimum	0.38	m
Maximum	0.49	m
Länge der Trennflächenspuren	4.02	m
Mittlere Länge der Trennflächenspuren	1.34	m
Standardabweichung der Länge der Trennflächenspuren	0.82	m
Länge der Kluftbrücken	0.00	m
Mittlere Länge der Kluftbrücken	0.00	m
Standardabweichung der Länge der Kluftbrücken	0.00	m

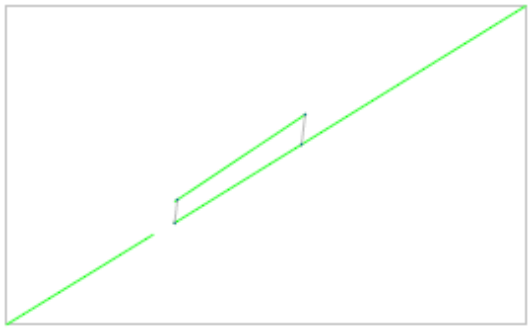

- **Statistical details for structural set 3**

Orientation measurements parameters

Beschreibung	Wert	Einheit
Fallrichtung	249.19	°
Fallwinkel	82.86	°
Sphärische Öffnung	19.89	°
Konzentration	16.12	
Orientierungsgrad	88.42	%
Vertrauenskegel	9.82	°
Konfidenz	95.0	%
Anzahl an Orientierungsmessungen	15 / 15	

Trace measurements parameters

Beschreibung	Wert	Einheit
Anzahl an Trennflächenspuren	7	
Trennflächenfrequenz	0.9800	Trennflächenspuren/m
Mittelwert	1.02	m
Standardabweichung	0.67	m
Minimum	0.08	m
Maximum	1.91	m
Länge der Trennflächenspuren	10.32	m
Mittlere Länge der Trennflächenspuren	1.47	m
Standardabweichung der Länge der Trennflächenspuren	1.30	m
Länge der Kluftbrücken	0.32	m
Mittlere Länge der Kluftbrücken	0.08	m
Standardabweichung der Länge der Kluftbrücken	0.03	m

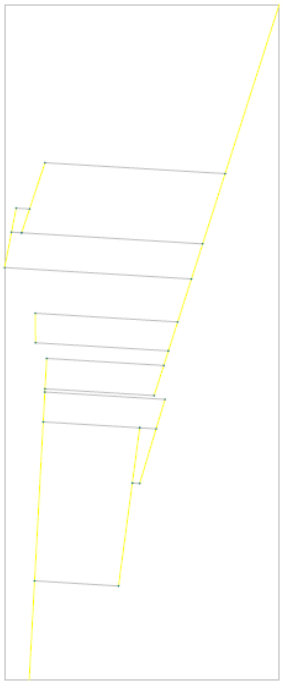

- **Statistical details for structural set 4**

Orientation measurements parameters

Beschreibung	Wert	Einheit
Fallrichtung	168.01	°
Fallwinkel	77.20	°
Sphärische Öffnung	9.05	°
Konzentration	69.29	
Orientierungsgrad	97.53	%
Vertrauenskegel	7.30	°
Konfidenz	95.0	%
Anzahl an Orientierungsmessungen	7 / 7	

Trace measurements parameters

Beschreibung	Wert	Einheit
Anzahl an Trennflächenspuren	3	
Trennflächenfrequenz	1.4375	Trennflächenspuren/m
Mittelwert	0.70	m
Standardabweichung	0.85	m
Minimum	0.00	m
Maximum	1.73	m
Länge der Trennflächenspuren	2.40	m
Mittlere Länge der Trennflächenspuren	0.80	m
Standardabweichung der Länge der Trennflächenspuren	0.24	m
Länge der Kluftbrücken	0.00	m
Mittlere Länge der Kluftbrücken	0.00	m
Standardabweichung der Länge der Kluftbrücken	0.00	m

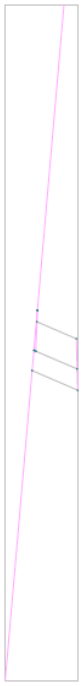

- **Statistical details for structural set 5**

Orientation measurements parameters

Beschreibung	Wert	Einheit
Fallrichtung	166.79	°
Fallwinkel	32.91	°
Sphärische Öffnung	10.96	°
Konzentration	46.07	
Orientierungsgrad	96.38	%
Vertrauenskegel	9.97	°
Konfidenz	95.0	%
Anzahl an Orientierungsmessungen	6 / 6	

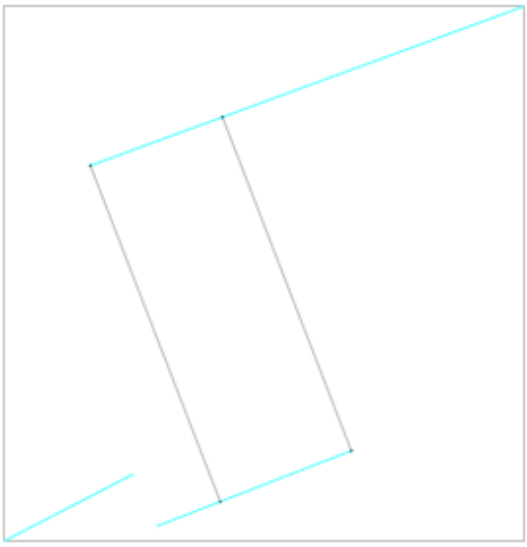

Trace measurements parameters

Beschreibung	Wert	Einheit
Anzahl an Trennflächenspuren	3	
Trennflächenfrequenz	0.6424	Trennflächenspuren/m
Mittelwert	1.56	m
Standardabweichung	0.01	m
Minimum	1.55	m
Maximum	1.56	m
Länge der Trennflächenspuren	3.32	m
Mittlere Länge der Trennflächenspuren	1.11	m
Standardabweichung der Länge der Trennflächenspuren	0.69	m
Länge der Kluftbrücken	0.00	m
Mittlere Länge der Kluftbrücken	0.00	m
Standardabweichung der Länge der Kluftbrücken	0.00	m

3. Outcrop 3

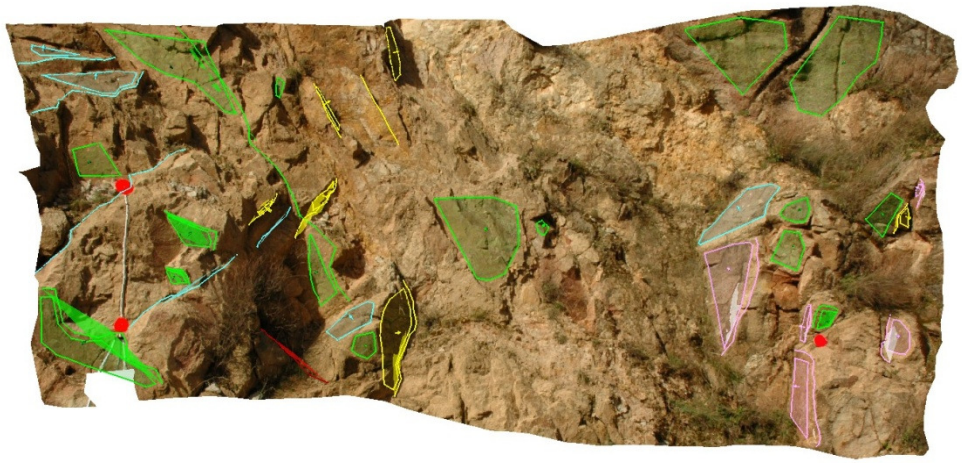

3D Model of Outcrop 3

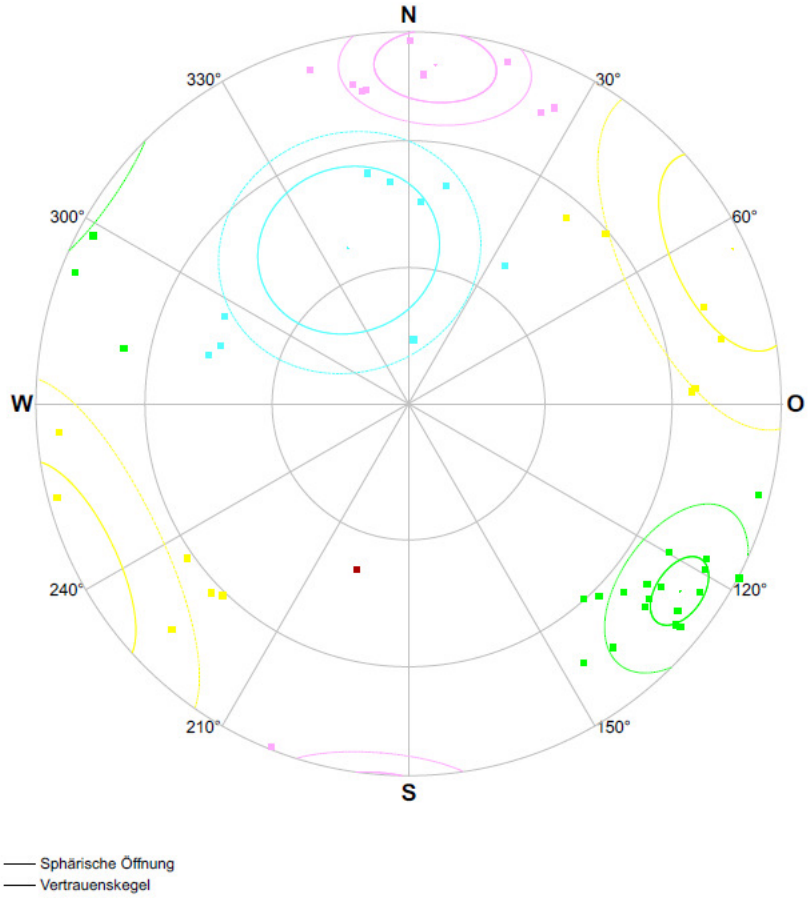

Orientation measurements of outcrop 3 (LHRC - Lambert projection).

- **Statistical details for structural set 2**

Orientation measurements parameters

Beschreibung	Wert	Einheit
Fallrichtung	304.68	°
Fallwinkel	77.63	°
Sphärische Öffnung	16.14	°
Konzentration	24.66	
Orientierungsgrad	92.28	%
Vertrauenskegel	6.53	°
Konfidenz	95.0	%
Anzahl an Orientierungsmessungen	21 / 21	

Trace measurements parameters

Beschreibung	Wert	Einheit
Anzahl an Trennflächenspuren	5	
Trennflächenfrequenz	1.1834	Trennflächenspuren/m
Mittelwert	0.85	m
Standardabweichung	0.62	m
Minimum	0.07	m
Maximum	1.84	m
Länge der Trennflächenspuren	6.90	m
Mittlere Länge der Trennflächenspuren	1.38	m
Standardabweichung der Länge der Trennflächenspuren	1.49	m
Länge der Kluftbrücken	0.00	m
Mittlere Länge der Kluftbrücken	0.00	m
Standardabweichung der Länge der Kluftbrücken	0.00	m

- **Statistical details for structural set 3**

Orientation measurements parameters

Beschreibung	Wert	Einheit
Fallrichtung	244.44	°
Fallwinkel	86.00	°
Sphärische Öffnung	29.69	°
Konzentration	7.47	
Orientierungsgrad	75.47	%
Vertrauenskegel	17.01	°
Konfidenz	95.0	%
Anzahl an Orientierungsmessungen	12 / 12	

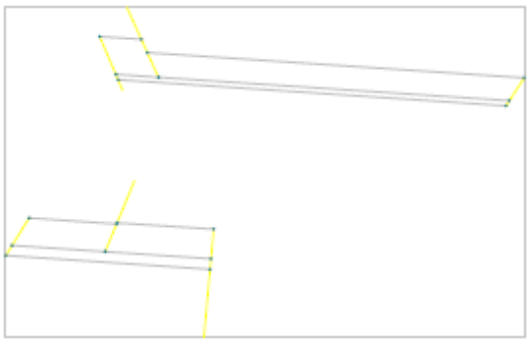

Trace measurements parameters

Beschreibung	Wert	Einheit
Anzahl an Trennflächenspuren	6	
Trennflächenfrequenz	0.3820	Trennflächenspuren/m
Mittelwert	2.62	m
Standardabweichung	2.06	m
Minimum	0.61	m
Maximum	5.68	m
Länge der Trennflächenspuren	5.06	m
Mittlere Länge der Trennflächenspuren	0.84	m
Standardabweichung der Länge der Trennflächenspuren	0.36	m
Länge der Kluftbrücken	0.00	m
Mittlere Länge der Kluftbrücken	0.00	m
Standardabweichung der Länge der Kluftbrücken	0.00	m

- **Statistical details for structural set 4**

Orientation measurements parameters

Beschreibung	Wert	Einheit
Fallrichtung	184.53	°
Fallwinkel	80.40	°
Sphärische Öffnung	16.12	°
Konzentration	23.36	
Orientierungsgrad	92.29	%
Vertrauenskegel	10.21	°
Konfidenz	95.0	%
Anzahl an Orientierungsmessungen	10 / 10	

Trace measurements parameters

Beschreibung	Wert	Einheit
Anzahl an Trennflächenspuren	5	
Trennflächenfrequenz	1.5110	Trennflächenspuren/m
Mittelwert	0.66	m
Standardabweichung	0.26	m
Minimum	0.35	m
Maximum	0.96	m
Länge der Trennflächenspuren	4.27	m
Mittlere Länge der Trennflächenspuren	0.85	m
Standardabweichung der Länge der Trennflächenspuren	0.51	m
Länge der Kluftbrücken	0.00	m
Mittlere Länge der Kluftbrücken	0.00	m
Standardabweichung der Länge der Kluftbrücken	0.00	m

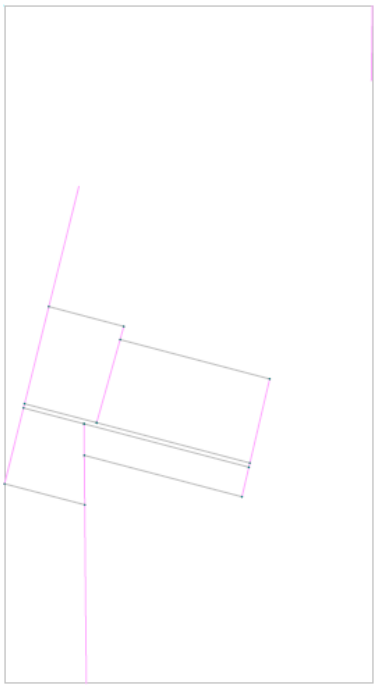

- **Statistical details for structural set 5**

Orientation measurements parameters

Beschreibung	Wert	Einheit
Fallrichtung	158.71	°
Fallwinkel	37.06	°
Sphärische Öffnung	27.66	°
Konzentration	8.25	
Orientierungsgrad	78.45	%
Vertrauenskegel	19.06	°
Konfidenz	95.0	%
Anzahl an Orientierungsmessungen	9 / 9	

Trace measurements parameters

Beschreibung	Wert	Einheit
Anzahl an Trennflächenspuren	5	
Trennflächenfrequenz	0.8023	Trennflächenspuren/m
Mittelwert	1.25	m
Standardabweichung	0.43	m
Minimum	0.49	m
Maximum	1.83	m
Länge der Trennflächenspuren	7.15	m
Mittlere Länge der Trennflächenspuren	1.43	m
Standardabweichung der Länge der Trennflächenspuren	0.57	m
Länge der Kluftbrücken	0.00	m
Mittlere Länge der Kluftbrücken	0.00	m
Standardabweichung der Länge der Kluftbrücken	0.00	m

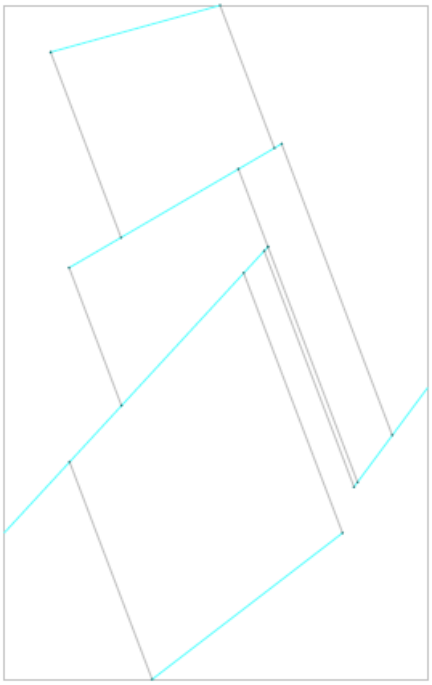

4. Outcrop 4

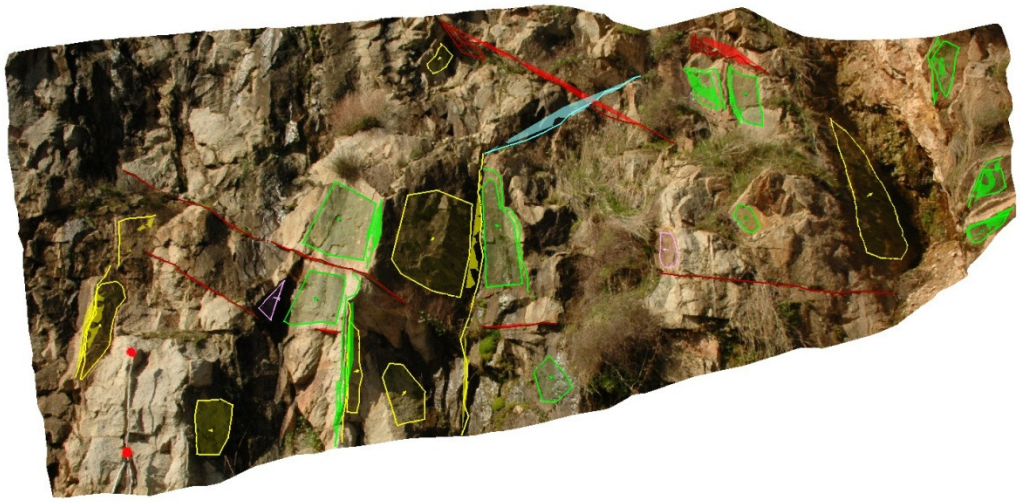

3D Model of Outcrop 4

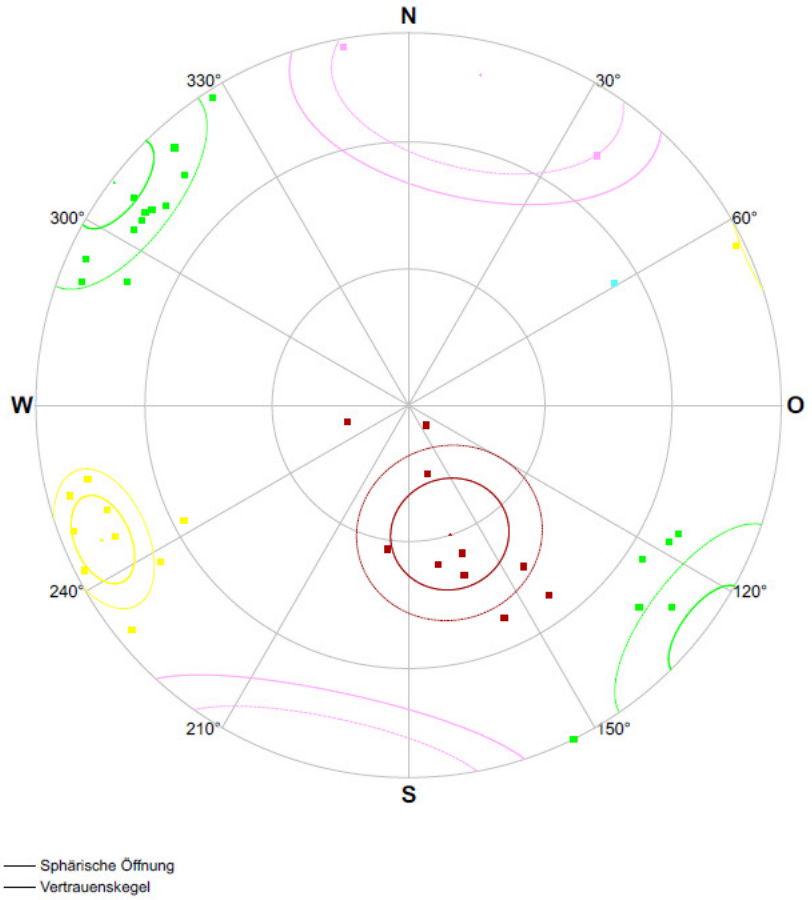

Orientation measurements of outcrop 4 (LHRC - Lambert projection).

- **Statistical details for structural set 1**

Orientation measurements parameters

Beschreibung	Wert	Einheit
Fallrichtung	342.24	°
Fallwinkel	29.96	°
Sphärische Öffnung	19.72	°
Konzentration	15.81	
Orientierungsgrad	88.61	%
Vertrauenskegel	12.54	°
Konfidenz	95.0	%
Anzahl an Orientierungsmessungen	10 / 10	

Trace measurements parameters

Beschreibung	Wert	Einheit
Anzahl an Trennflächenspuren	9	
Trennflächenfrequenz	0.3733	Trennflächenspuren/m
Mittelwert	2.68	m
Standardabweichung	1.64	m
Minimum	0.90	m
Maximum	4.92	m
Länge der Trennflächenspuren	18.00	m
Mittlere Länge der Trennflächenspuren	2.00	m
Standardabweichung der Länge der Trennflächenspuren	1.36	m
Länge der Kluftbrücken	0.82	m
Mittlere Länge der Kluftbrücken	0.41	m
Standardabweichung der Länge der Kluftbrücken	0.05	m

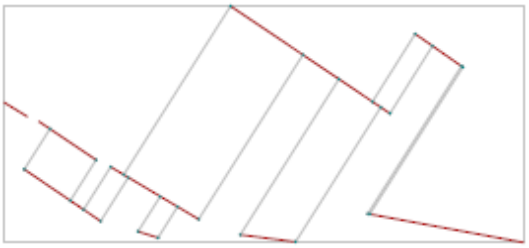

- **Statistical details for structural set 2**

Orientation measurements parameters

Beschreibung	Wert	Einheit
Fallrichtung	127.13	°
Fallwinkel	88.88	°
Sphärische Öffnung	18.48	°
Konzentration	18.80	
Orientierungsgrad	89.95	%
Vertrauenskegel	8.19	°
Konfidenz	95.0	%
Anzahl an Orientierungsmessungen	18 / 18	

Trace measurements parameters

Beschreibung	Wert	Einheit
Anzahl an Trennflächenspuren	8	
Trennflächenfrequenz	1.2097	Trennflächenspuren/m
Mittelwert	0.83	m
Standardabweichung	1.14	m
Minimum	0.01	m
Maximum	3.19	m
Länge der Trennflächenspuren	11.21	m
Mittlere Länge der Trennflächenspuren	1.40	m
Standardabweichung der Länge der Trennflächenspuren	0.70	m
Länge der Kluftbrücken	0.00	m
Mittlere Länge der Kluftbrücken	0.00	m
Standardabweichung der Länge der Kluftbrücken	0.00	m

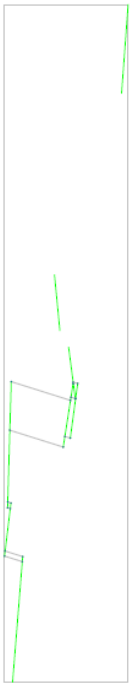

- **Statistical details for structural set 3**

Orientation measurements parameters

Beschreibung	Wert	Einheit
Fallrichtung	66.24	°
Fallwinkel	78.93	°
Sphärische Öffnung	12.44	°
Konzentration	38.81	
Orientierungsgrad	95.36	%
Vertrauenskegel	7.85	°
Konfidenz	95.0	%
Anzahl an Orientierungsmessungen	10 / 10	

Trace measurements parameters

Beschreibung	Wert	Einheit
Anzahl an Trennflächenspuren	4	
Trennflächenfrequenz	0.7367	Trennflächenspuren/m
Mittelwert	1.36	m
Standardabweichung	0.89	m
Minimum	0.44	m
Maximum	2.68	m
Länge der Trennflächenspuren	9.67	m
Mittlere Länge der Trennflächenspuren	2.42	m
Standardabweichung der Länge der Trennflächenspuren	1.50	m
Länge der Kluftbrücken	0.00	m
Mittlere Länge der Kluftbrücken	0.00	m
Standardabweichung der Länge der Kluftbrücken	0.00	m

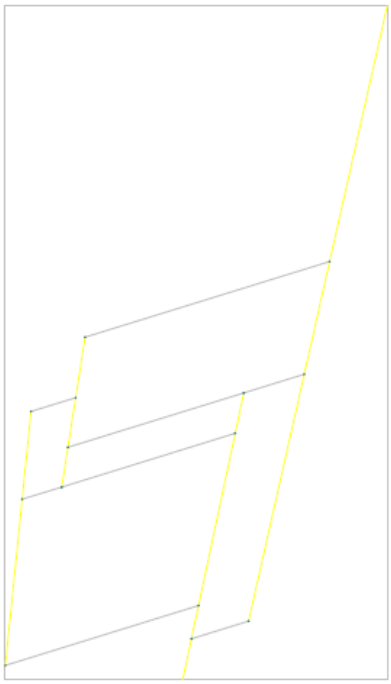

5. Outcrop 5

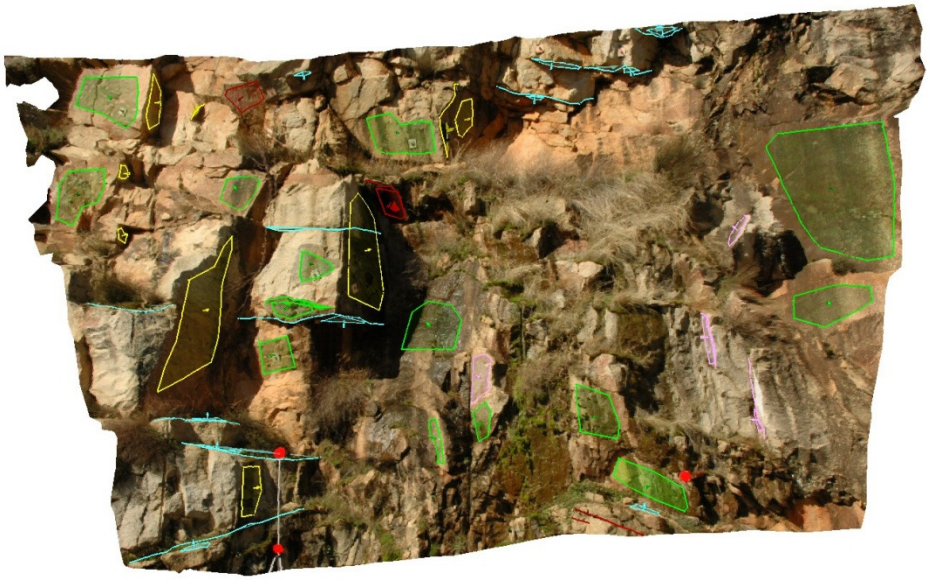

3D Model of Outcrop 5

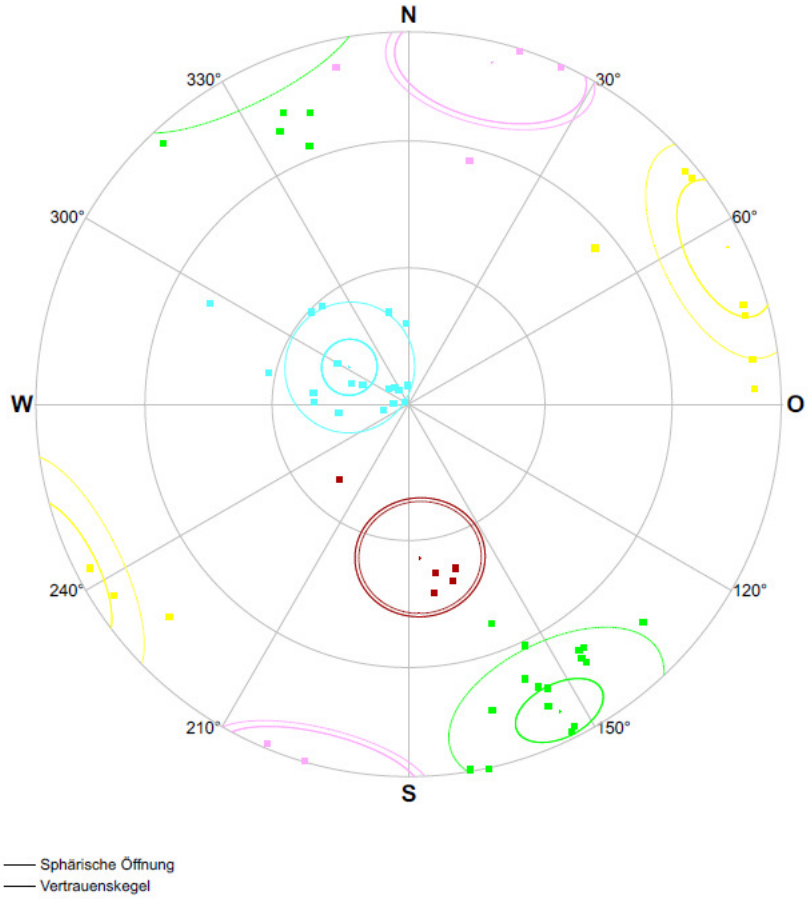

Orientation measurements of outcrop 5 (LHRC - Lambert projection).

- **Statistical details for structural set 1**

Orientation measurements parameters

Beschreibung	Wert	Einheit
Fallrichtung	355.70	°
Fallwinkel	34.15	°
Sphärische Öffnung	12.77	°
Konzentration	32.76	
Orientierungsgrad	95.12	%
Vertrauenskegel	13.57	°
Konfidenz	95.0	%
Anzahl an Orientierungsmessungen	5 / 5	

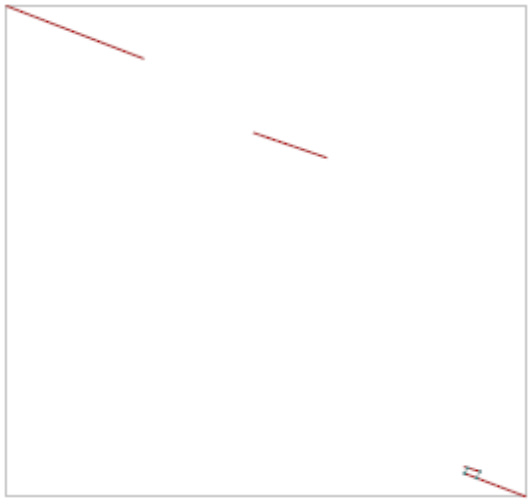

Trace measurements parameters

Beschreibung	Wert	Einheit
Anzahl an Trennflächenspuren	4	
Trennflächenfrequenz	7.6373	Trennflächenspuren/m
Mittelwert	0.13	m
Standardabweichung	0.01	m
Minimum	0.12	m
Maximum	0.14	m
Länge der Trennflächenspuren	4.77	m
Mittlere Länge der Trennflächenspuren	1.19	m
Standardabweichung der Länge der Trennflächenspuren	0.90	m
Länge der Kluftbrücken	0.00	m
Mittlere Länge der Kluftbrücken	0.00	m
Standardabweichung der Länge der Kluftbrücken	0.00	m

- **Statistical details for structural set 2**

Orientation measurements parameters

Beschreibung	Wert	Einheit
Fallrichtung	333.78	°
Fallwinkel	81.13	°
Sphärische Öffnung	19.15	°
Konzentration	17.69	
Orientierungsgrad	89.23	%
Vertrauenskegel	7.77	°
Konfidenz	95.0	%
Anzahl an Orientierungsmessungen	21 / 21	

Trace measurements parameters

Beschreibung	Wert	Einheit
Anzahl an Trennflächenspuren	7	
Trennflächenfrequenz	0.4912	Trennflächenspuren/
Mittelwert	2.04	m
Standardabweichung	2.11	m
Minimum	0.01	m
Maximum	5.52	m
Länge der Trennflächenspuren	10.97	m
Mittlere Länge der Trennflächenspuren	1.57	m
Standardabweichung der Länge der Trennflächenspuren	0.62	m
Länge der Kluftbrücken	0.00	m
Mittlere Länge der Kluftbrücken	0.00	m
Standardabweichung der Länge der Kluftbrücken	0.00	m

- **Statistical details for structural set 3**

Orientation measurements parameters

Beschreibung	Wert	Einheit
Fallrichtung	243.77	°
Fallwinkel	85.03	°
Sphärische Öffnung	18.70	°
Konzentration	17.50	
Orientierungsgrad	89.72	%
Vertrauenskegel	11.88	°
Konfidenz	95.0	%
Anzahl an Orientierungsmessungen	10 / 10	

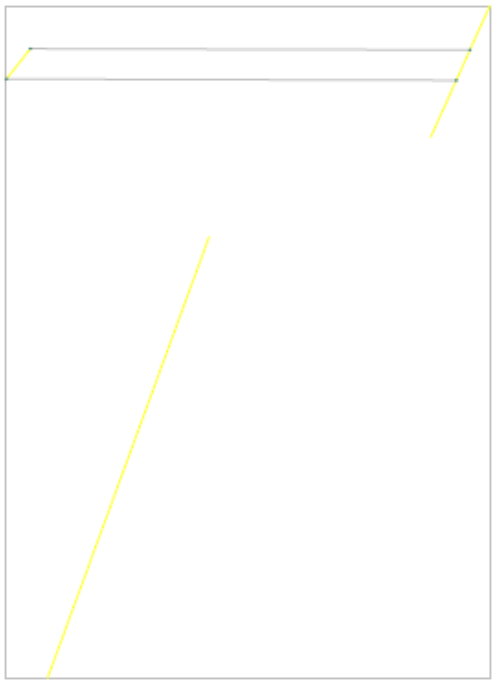

Trace measurements parameters

Beschreibung	Wert	Einheit
Anzahl an Trennflächenspuren	3	
Trennflächenfrequenz	0.2143	Trennflächenspuren/m
Mittelwert	4.67	m
Standardabweichung	0.08	m
Minimum	4.61	m
Maximum	4.72	m
Länge der Trennflächenspuren	6.77	m
Mittlere Länge der Trennflächenspuren	2.26	m
Standardabweichung der Länge der Trennflächenspuren	2.40	m
Länge der Kluftbrücken	0.00	m
Mittlere Länge der Kluftbrücken	0.00	m
Standardabweichung der Länge der Kluftbrücken	0.00	m

- **Statistical details for structural set 4**

Orientation measurements parameters

Beschreibung	Wert	Einheit
Fallrichtung	193.71	°
Fallwinkel	83.78	°
Sphärische Öffnung	17.34	°
Konzentration	18.76	
Orientierungsgrad	91.12	%
Vertrauenskegel	15.87	°
Konfidenz	95.0	%
Anzahl an Orientierungsmessungen	6 / 6	

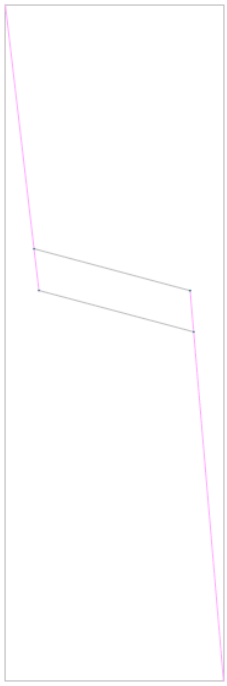

Trace measurements parameters

Beschreibung	Wert	Einheit
Anzahl an Trennflächenspuren	2	
Trennflächenfrequenz	1.8780	Trennflächenspuren/m
Mittelwert	0.53	m
Standardabweichung	0.00	m
Minimum	0.53	m
Maximum	0.53	m
Länge der Trennflächenspuren	2.39	m
Mittlere Länge der Trennflächenspuren	1.20	m
Standardabweichung der Länge der Trennflächenspuren	0.27	m
Länge der Kluftbrücken	0.00	m
Mittlere Länge der Kluftbrücken	0.00	m
Standardabweichung der Länge der Kluftbrücken	0.00	m

- **Statistical details for structural set 5**

Orientation measurements parameters

Beschreibung	Wert	Einheit
Fallrichtung	122.02	°
Fallwinkel	15.23	°
Sphärische Öffnung	14.21	°
Konzentration	31.46	
Orientierungsgrad	93.98	%
Vertrauenskegel	6.08	°
Konfidenz	95.0	%
Anzahl an Orientierungsmessungen	19 / 19	

Trace measurements parameters

Beschreibung	Wert	Einheit
Anzahl an Trennflächenspuren	9	
Trennflächenfrequenz	0.6562	Trennflächenspuren/m
Mittelwert	1.52	m
Standardabweichung	0.90	m
Minimum	0.06	m
Maximum	3.94	m
Länge der Trennflächenspuren	16.78	m
Mittlere Länge der Trennflächenspuren	1.86	m
Standardabweichung der Länge der Trennflächenspuren	0.63	m
Länge der Kluftbrücken	0.00	m
Mittlere Länge der Kluftbrücken	0.00	m
Standardabweichung der Länge der Kluftbrücken	0.00	m

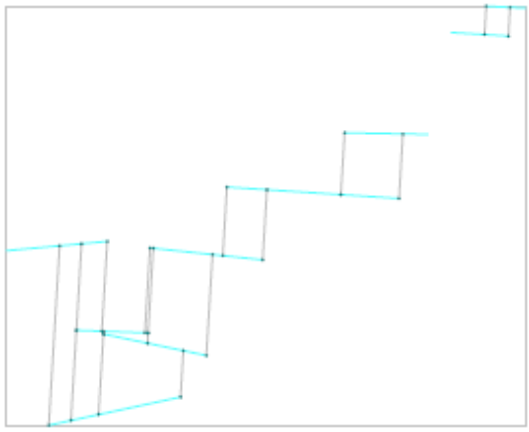

6. Outcrop 6

3D Model of Outcrop 6

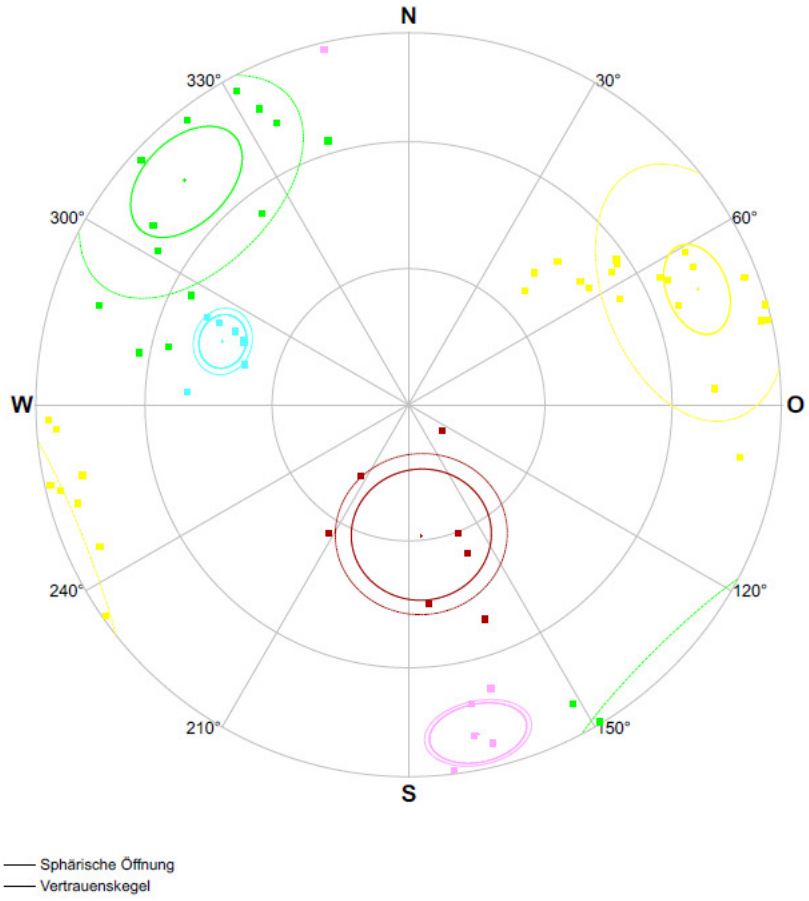

Orientation measurements of outcrop 6 (LHRC - Lambert projection).

- **Statistical details for structural set 1**

Orientation measurements parameters

Beschreibung	Wert	Einheit
Fallrichtung	354.37	°
Fallwinkel	28.98	°
Sphärische Öffnung	18.19	°
Konzentration	17.60	
Orientierungsgrad	90.26	%
Vertrauenskegel	14.80	°
Konfidenz	95.0	%
Anzahl an Orientierungsmessungen	7 / 13	

Trace measurements parameters

Beschreibung	Wert	Einheit
Anzahl an Trennflächenspuren	8	
Trennflächenfrequenz	0.3382	Trennflächenspuren/m
Mittelwert	2.96	m
Standardabweichung	0.85	m
Minimum	2.24	m
Maximum	5.08	m
Länge der Trennflächenspuren	13.61	m
Mittlere Länge der Trennflächenspuren	1.70	m
Standardabweichung der Länge der Trennflächenspuren	0.70	m
Länge der Kluftbrücken	1.49	m
Mittlere Länge der Kluftbrücken	0.74	m
Standardabweichung der Länge der Kluftbrücken	0.21	m

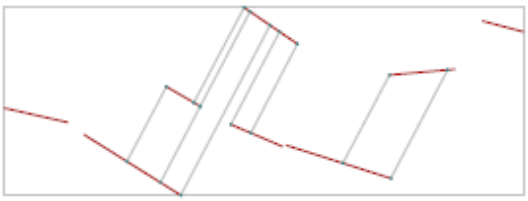

- **Statistical details for structural set 2**

Orientation measurements parameters

Beschreibung	Wert	Einheit
Fallrichtung	135.15	°
Fallwinkel	74.02	°
Sphärische Öffnung	23.31	°
Konzentration	11.92	
Orientierungsgrad	84.34	%
Vertrauenskegel	11.56	°
Konfidenz	95.0	%
Anzahl an Orientierungsmessungen	15 / 15	

Trace measurements parameters

Beschreibung	Wert	Einheit
Anzahl an Trennflächenspuren	4	
Trennflächenfrequenz	0.6248	Trennflächenspuren/m
Mittelwert	1.60	m
Standardabweichung	0.51	m
Minimum	1.07	m
Maximum	2.24	m
Länge der Trennflächenspuren	8.94	m
Mittlere Länge der Trennflächenspuren	2.23	m
Standardabweichung der Länge der Trennflächenspuren	1.19	m
Länge der Kluftbrücken	0.00	m
Mittlere Länge der Kluftbrücken	0.00	m
Standardabweichung der Länge der Kluftbrücken	0.00	m

- **Statistical details for structural set 3**

Orientation measurements parameters

Beschreibung	Wert	Einheit
Fallrichtung	248.14	°
Fallwinkel	72.56	°
Sphärische Öffnung	23.73	°
Konzentration	11.91	
Orientierungsgrad	83.80	%
Vertrauenskegel	8.25	°
Konfidenz	95.0	%
Anzahl an Orientierungsmessungen	28 / 28	

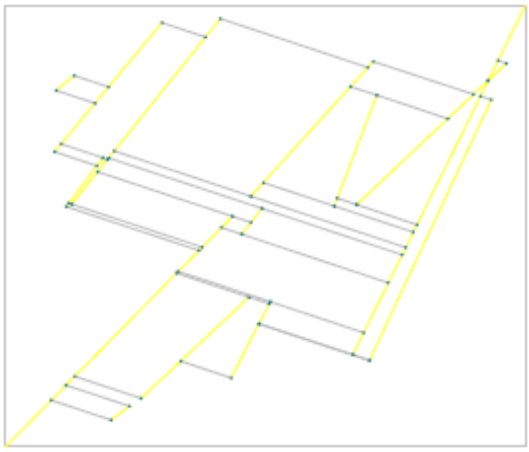

Trace measurements parameters

Beschreibung	Wert	Einheit
Anzahl an Trennflächenspuren	14	
Trennflächenfrequenz	0.6508	Trennflächenspuren/m
Mittelwert	1.54	m
Standardabweichung	1.13	m
Minimum	0.00	m
Maximum	3.51	m
Länge der Trennflächenspuren	38.74	m
Mittlere Länge der Trennflächenspuren	2.77	m
Standardabweichung der Länge der Trennflächenspuren	2.01	m
Länge der Kluftbrücken	0.00	m
Mittlere Länge der Kluftbrücken	0.00	m
Standardabweichung der Länge der Kluftbrücken	0.00	m

- **Statistical details for structural set 4**

Orientation measurements parameters

Beschreibung	Wert	Einheit
Fallrichtung	348.03	°
Fallwinkel	79.56	°
Sphärische Öffnung	9.08	°
Konzentration	66.88	
Orientierungsgrad	97.51	%
Vertrauenskegel	8.25	°
Konfidenz	95.0	%
Anzahl an Orientierungsmessungen	6 / 6	

Trace measurements parameters

Beschreibung	Wert	Einheit
Anzahl an Trennflächenspuren	3	
Trennflächenfrequenz	0.5320	Trennflächenspuren/m
Mittelwert	1.88	m
Standardabweichung	0.55	m
Minimum	1.38	m
Maximum	2.46	m
Länge der Trennflächenspuren	6.31	m
Mittlere Länge der Trennflächenspuren	2.10	m
Standardabweichung der Länge der Trennflächenspuren	1.04	m
Länge der Kluftbrücken	0.00	m
Mittlere Länge der Kluftbrücken	0.00	m
Standardabweichung der Länge der Kluftbrücken	0.00	m

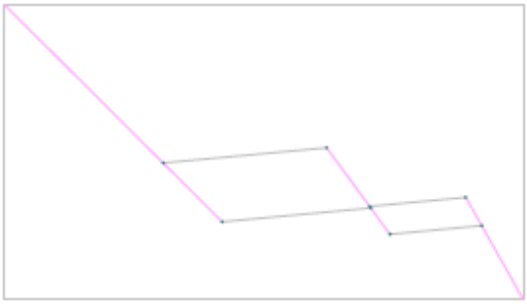

- **Statistical details for structural set 5**

Orientation measurements parameters

Beschreibung	Wert	Einheit
Fallrichtung	108.86	°
Fallwinkel	43.80	°
Sphärische Öffnung	6.82	°
Konzentration	121.65	
Orientierungsgrad	98.59	%
Vertrauenskegel	5.49	°
Konfidenz	95.0	%
Anzahl an Orientierungsmessungen	7 / 7	

Trace measurements parameters

Beschreibung	Wert	Einheit
Anzahl an Trennflächenspuren	3	
Trennflächenfrequenz	3.7783	Trennflächenspuren/m
Mittelwert	0.26	m
Standardabweichung	0.05	m
Minimum	0.23	m
Maximum	0.30	m
Länge der Trennflächenspuren	5.80	m
Mittlere Länge der Trennflächenspuren	1.93	m
Standardabweichung der Länge der Trennflächenspuren	0.63	m
Länge der Kluftbrücken	0.00	m
Mittlere Länge der Kluftbrücken	0.00	m
Standardabweichung der Länge der Kluftbrücken	0.00	m

7. Outcrop 7

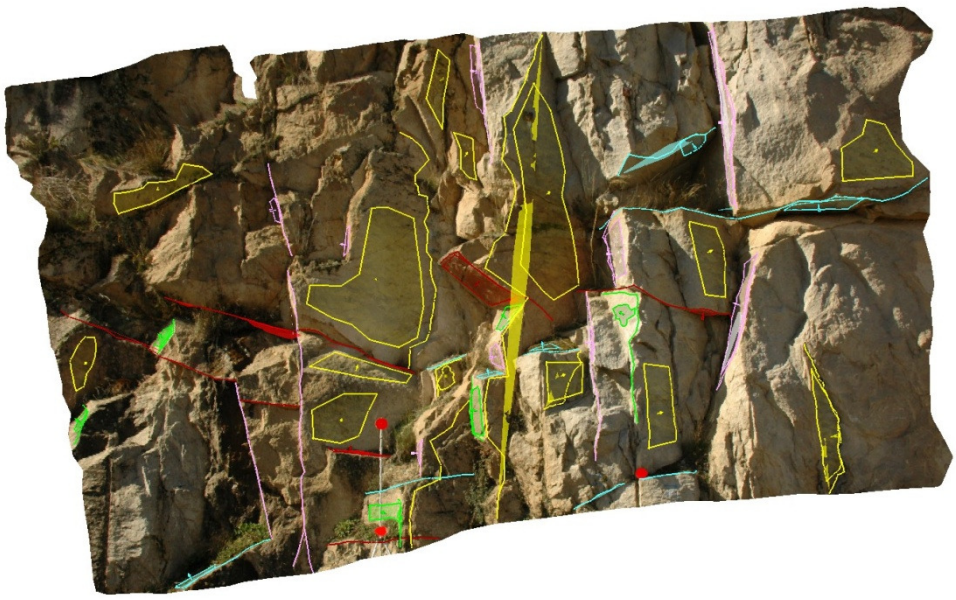

3D Model of Outcrop 7

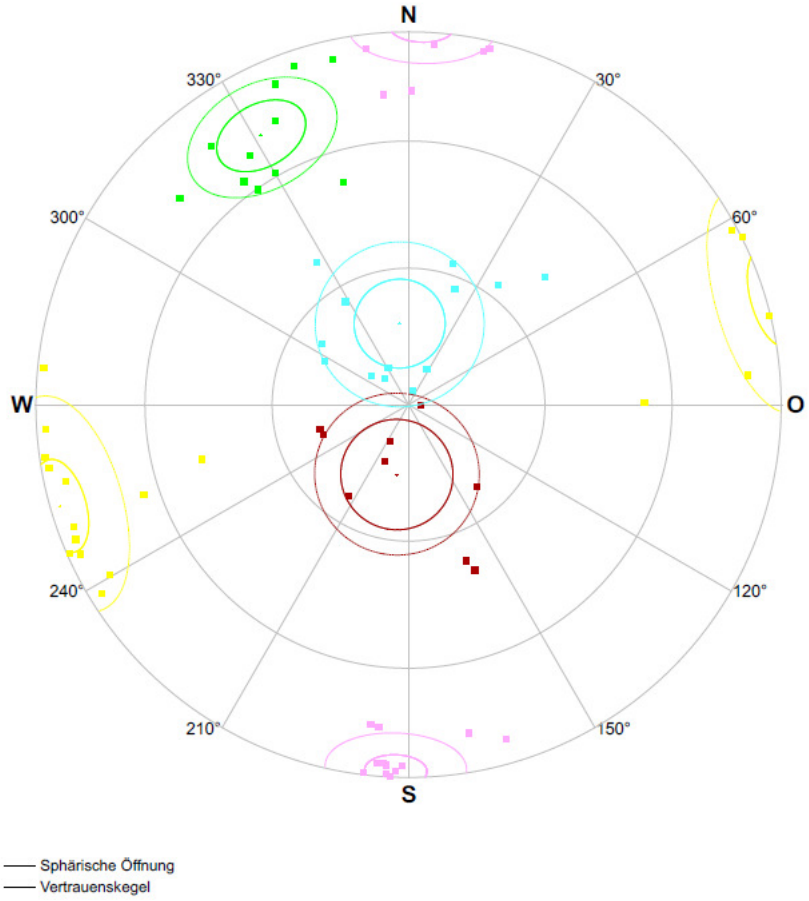

Orientation measurements of outcrop 7 (LHRC - Lambert projection).

- **Statistical details for structural set 1**

Orientation measurements parameters

Beschreibung	Wert	Einheit
Fallrichtung	9.47	°
Fallwinkel	15.54	°
Sphärische Öffnung	17.81	°
Konzentration	18.99	
Orientierungsgrad	90.64	%
Vertrauenskegel	12.12	°
Konfidenz	95.0	%
Anzahl an Orientierungsmessungen	9 / 9	

Trace measurements parameters

Beschreibung	Wert	Einheit
Anzahl an Trennflächenspuren	7	
Trennflächenfrequenz	0.5977	Trennflächenspuren/m
Mittelwert	1.67	m
Standardabweichung	0.83	m
Minimum	0.88	m
Maximum	3.64	m
Länge der Trennflächenspuren	14.27	m
Mittlere Länge der Trennflächenspuren	2.04	m
Standardabweichung der Länge der Trennflächenspuren	1.10	m
Länge der Kluftbrücken	0.00	m
Mittlere Länge der Kluftbrücken	0.00	m
Standardabweichung der Länge der Kluftbrücken	0.00	m

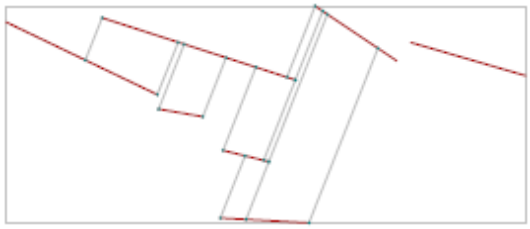

- **Statistical details for structural set 2**

Orientation measurements parameters

Beschreibung	Wert	Einheit
Fallrichtung	151.25	°
Fallwinkel	71.40	°
Sphärische Öffnung	14.19	°
Konzentration	30.26	
Orientierungsgrad	93.99	%
Vertrauenskegel	8.44	°
Konfidenz	95.0	%
Anzahl an Orientierungsmessungen	11 / 11	

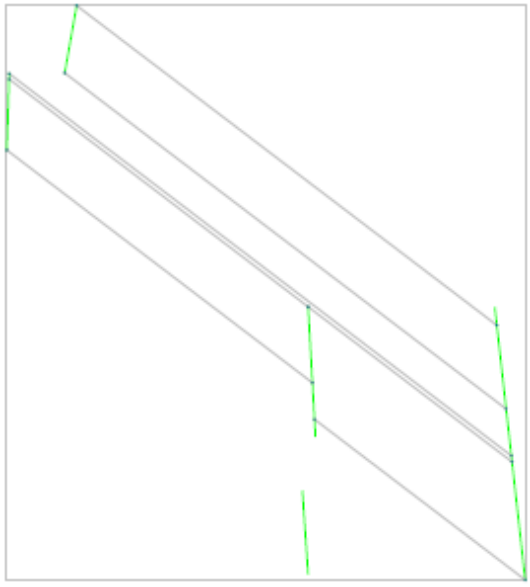

Trace measurements parameters

Beschreibung	Wert	Einheit
Anzahl an Trennflächenspuren	5	
Trennflächenfrequenz	0.2806	Trennflächenspuren/m
Mittelwert	3.56	m
Standardabweichung	1.22	m
Minimum	2.14	m
Maximum	5.26	m
Länge der Trennflächenspuren	5.28	m
Mittlere Länge der Trennflächenspuren	1.06	m
Standardabweichung der Länge der Trennflächenspuren	0.65	m
Länge der Kluftbrücken	0.00	m
Mittlere Länge der Kluftbrücken	0.00	m
Standardabweichung der Länge der Kluftbrücken	0.00	m

- **Statistical details for structural set 3**

Orientation measurements parameters

Beschreibung	Wert	Einheit
Fallrichtung	73.73	°
Fallwinkel	87.04	°
Sphärische Öffnung	17.61	°
Konzentration	20.69	
Orientierungsgrad	90.84	%
Vertrauenskegel	7.56	°
Konfidenz	95.0	%
Anzahl an Orientierungsmessungen	19 / 19	

Trace measurements parameters

Beschreibung	Wert	Einheit
Anzahl an Trennflächenspuren	6	
Trennflächenfrequenz	0.8135	Trennflächenspuren/m
Mittelwert	1.23	m
Standardabweichung	0.88	m
Minimum	0.30	m
Maximum	2.97	m
Länge der Trennflächenspuren	17.35	m
Mittlere Länge der Trennflächenspuren	2.89	m
Standardabweichung der Länge der Trennflächenspuren	2.53	m
Länge der Kluftbrücken	0.00	m
Mittlere Länge der Kluftbrücken	0.00	m
Standardabweichung der Länge der Kluftbrücken	0.00	m

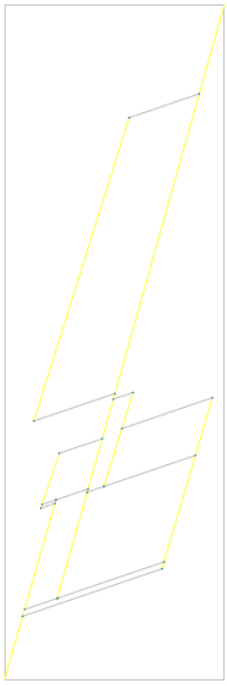

- **Statistical details for structural set 4**

Orientation measurements parameters

Beschreibung	Wert	Einheit
Fallrichtung	1.99	°
Fallwinkel	88.19	°
Sphärische Öffnung	11.07	°
Konzentration	51.20	
Orientierungsgrad	96.31	%
Vertrauenskegel	4.88	°
Konfidenz	95.0	%
Anzahl an Orientierungsmessungen	18 / 18	

Trace measurements parameters

Beschreibung	Wert	Einheit
Anzahl an Trennflächenspuren	10	
Trennflächenfrequenz	0.4142	Trennflächenspuren/m
Mittelwert	2.41	m
Standardabweichung	1.48	m
Minimum	0.06	m
Maximum	4.70	m
Länge der Trennflächenspuren	20.06	m
Mittlere Länge der Trennflächenspuren	2.01	m
Standardabweichung der Länge der Trennflächenspuren	1.23	m
Länge der Kluftbrücken	0.00	m
Mittlere Länge der Kluftbrücken	0.00	m
Standardabweichung der Länge der Kluftbrücken	0.00	m

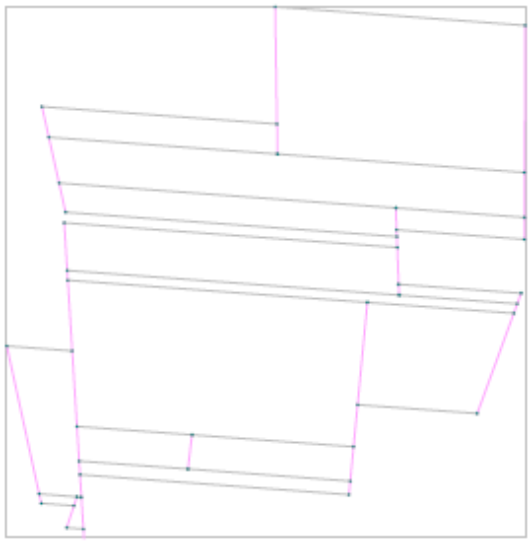

- **Statistical details for structural set 5**

Orientation measurements parameters

Beschreibung	Wert	Einheit
Fallrichtung	173.74	°
Fallwinkel	17.85	°
Sphärische Öffnung	18.22	°
Konzentration	18.88	
Orientierungsgrad	90.22	%
Vertrauenskegel	9.80	°
Konfidenz	95.0	%
Anzahl an Orientierungsmessungen	13 / 13	

Trace measurements parameters

Beschreibung	Wert	Einheit
Anzahl an Trennflächenspuren	8	
Trennflächenfrequenz	0.6941	Trennflächenspuren/m
Mittelwert	1.44	m
Standardabweichung	0.77	m
Minimum	0.24	m
Maximum	2.39	m
Länge der Trennflächenspuren	12.38	m
Mittlere Länge der Trennflächenspuren	1.55	m
Standardabweichung der Länge der Trennflächenspuren	1.38	m
Länge der Kluftbrücken	0.00	m
Mittlere Länge der Kluftbrücken	0.00	m
Standardabweichung der Länge der Kluftbrücken	0.00	m

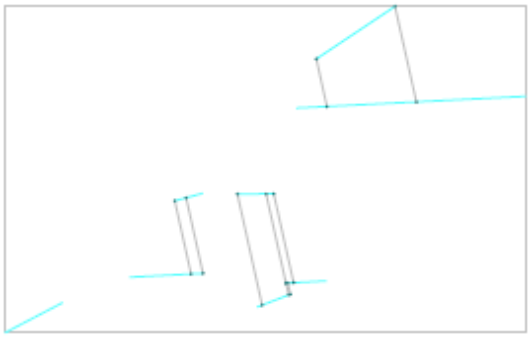

8. Outcrop 8

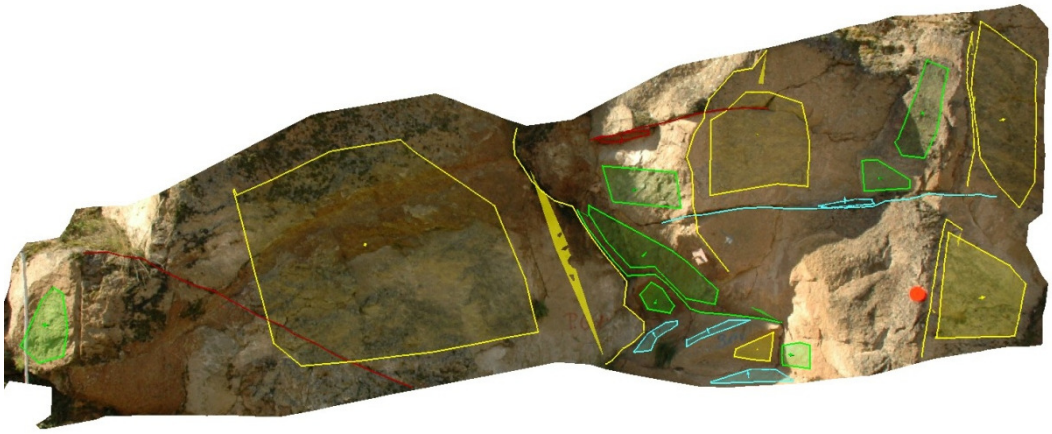

3D Model of Outcrop 8

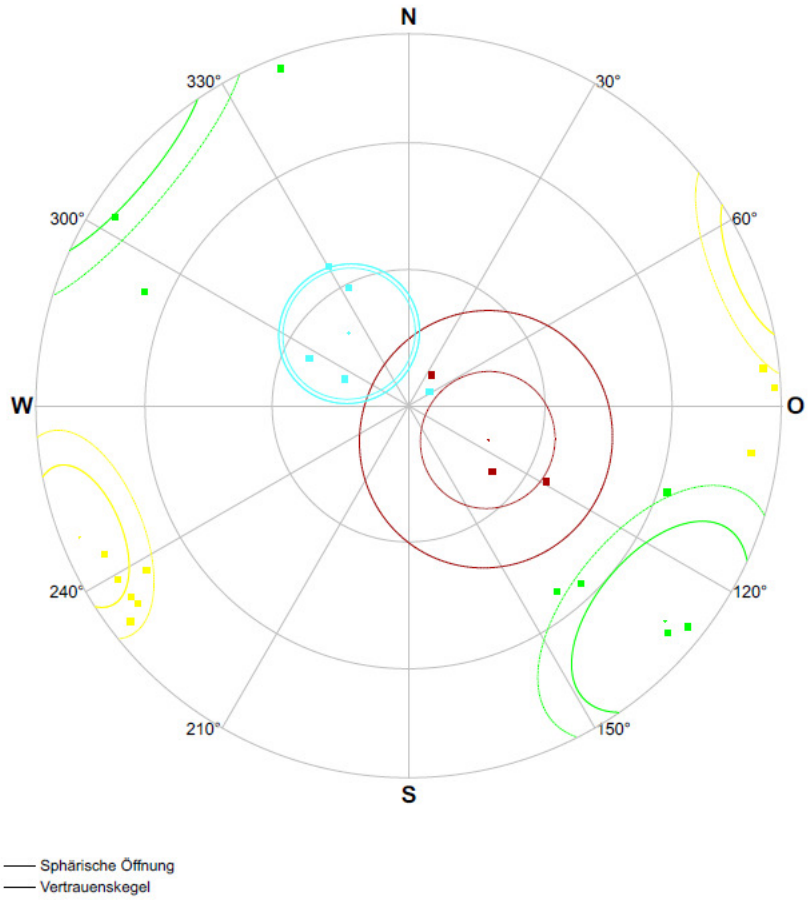

Orientation measurements of outcrop 8 (LHRC - Lambert projection).

- **Statistical details for structural set 1**

Orientation measurements parameters

Beschreibung	Wert	Einheit
Fallrichtung	293.42	°
Fallwinkel	19.00	°
Sphärische Öffnung	14.82	°
Konzentration	20.37	
Orientierungsgrad	93.46	%
Vertrauenskegel	28.05	°
Konfidenz	95.0	%
Anzahl an Orientierungsmessungen	3 / 3	

- **Statistical details for structural set 2**

Orientation measurements parameters

Beschreibung	Wert	Einheit
Fallrichtung	310.11	°
Fallwinkel	79.01	°
Sphärische Öffnung	25.30	°
Konzentration	9.58	
Orientierungsgrad	81.74	%
Vertrauenskegel	18.86	°
Konfidenz	95.0	%
Anzahl an Orientierungsmessungen	8 / 8	

- **Statistical details for structural set 3**

Orientation measurements parameters

Beschreibung	Wert	Einheit
Fallrichtung	68.14	°
Fallwinkel	84.55	°
Sphärische Öffnung	17.79	°
Konzentration	19.05	
Orientierungsgrad	90.67	%
Vertrauenskegel	12.10	°
Konfidenz	95.0	%
Anzahl an Orientierungsmessungen	9 / 9	

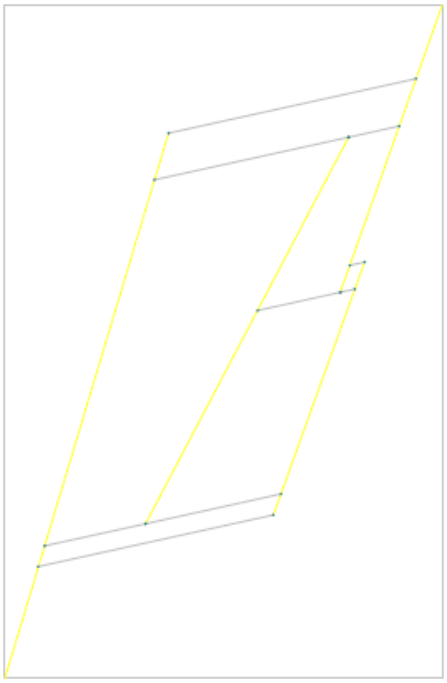

Trace measurements parameters

Beschreibung	Wert	Einheit
Anzahl an Trennflächenspuren	4	
Trennflächenfrequenz	0.6064	Trennflächenspuren/m
Mittelwert	1.65	m
Standardabweichung	1.23	m
Minimum	0.20	m
Maximum	3.41	m
Länge der Trennflächenspuren	8.26	m
Mittlere Länge der Trennflächenspuren	2.07	m
Standardabweichung der Länge der Trennflächenspuren	0.53	m
Länge der Kluftbrücken	0.00	m
Mittlere Länge der Kluftbrücken	0.00	m
Standardabweichung der Länge der Kluftbrücken	0.00	m

- **Statistical details for structural set 5**

Orientation measurements parameters

Beschreibung	Wert	Einheit
Fallrichtung	140.53	°
Fallwinkel	20.61	°
Sphärische Öffnung	14.37	°
Konzentration	25.98	
Orientierungsgrad	93.84	%
Vertrauenskegel	15.29	°
Konfidenz	95.0	%
Anzahl an Orientierungsmessungen	5 / 5	

9. Outcrop 9

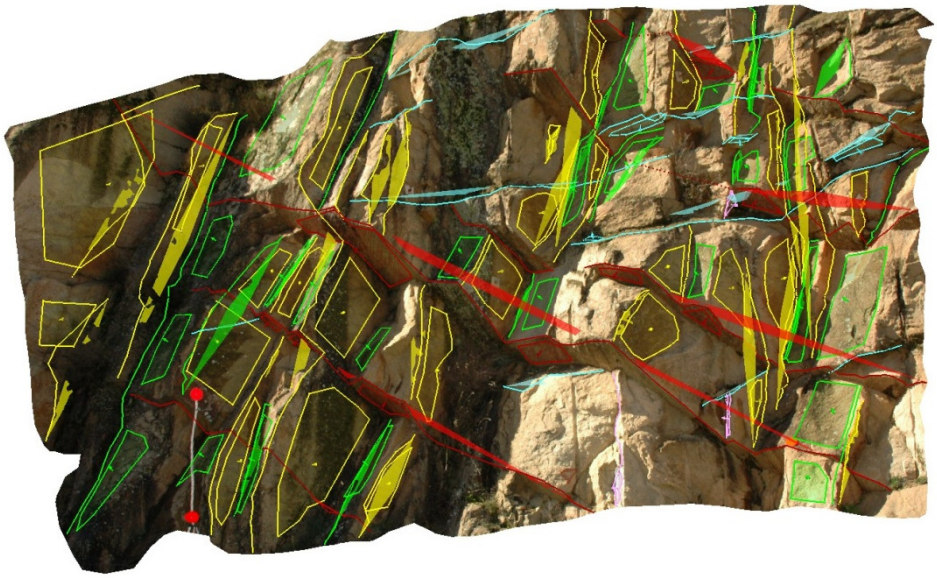

3D Model of Outcrop 9

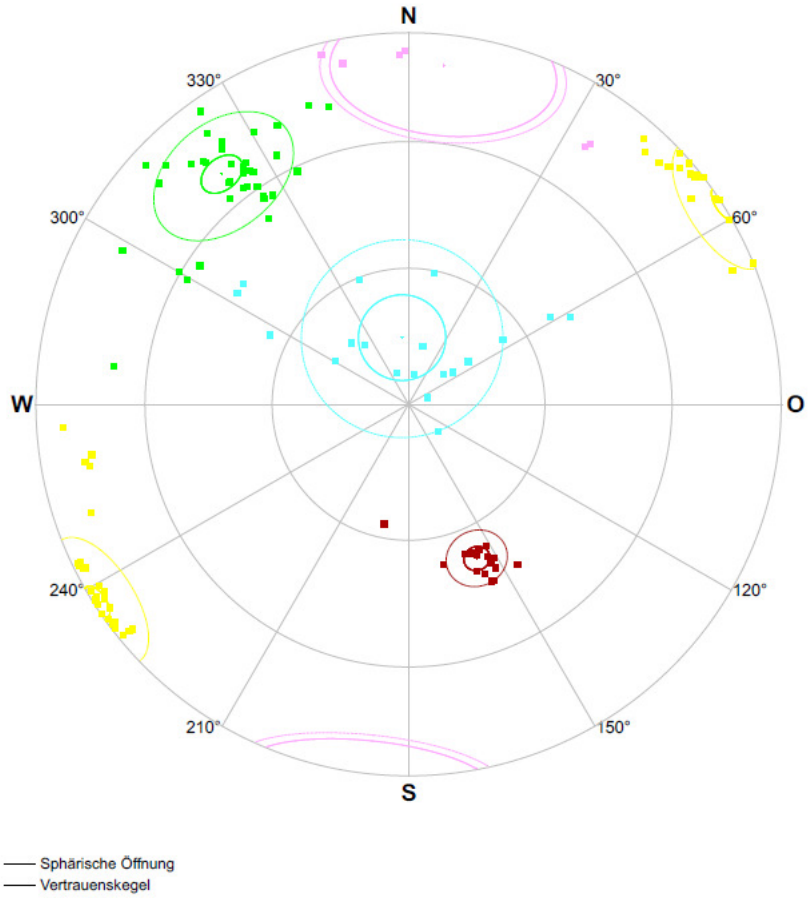

Orientation measurements of outcrop 9 (LHRC - Lambert projection).

- **Statistical details for structural set 1**

Orientation measurements parameters

Beschreibung	Wert	Einheit
Fallrichtung	336.16	°
Fallwinkel	37.44	°
Sphärische Öffnung	6.41	°
Konzentration	152.15	
Orientierungsgrad	98.75	%
Vertrauenskegel	2.73	°
Konfidenz	95.0	%
Anzahl an Orientierungsmessungen	19 / 19	

Trace measurements parameters

Beschreibung	Wert	Einheit
Anzahl an Trennflächenspuren	10	
Trennflächenfrequenz	0.5318	Trennflächenspuren/m
Mittelwert	1.88	m
Standardabweichung	0.80	m
Minimum	0.88	m
Maximum	3.54	m
Länge der Trennflächenspuren	36.72	m
Mittlere Länge der Trennflächenspuren	3.67	m
Standardabweichung der Länge der Trennflächenspuren	3.44	m
Länge der Kluftbrücken	3.24	m
Mittlere Länge der Kluftbrücken	1.08	m
Standardabweichung der Länge der Kluftbrücken	0.73	m

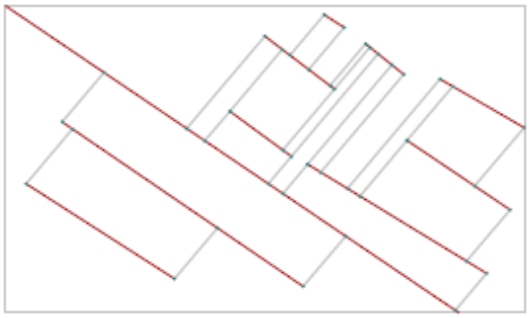

- **Statistical details for structural set 2**

Orientation measurements parameters

Beschreibung	Wert	Einheit
Fallrichtung	141.04	°
Fallwinkel	68.64	°
Sphärische Öffnung	14.17	°
Konzentration	32.46	
Orientierungsgrad	94.01	%
Vertrauenskegel	4.20	°
Konfidenz	95.0	%
Anzahl an Orientierungsmessungen	37 / 37	

Trace measurements parameters

Beschreibung	Wert	Einheit
Anzahl an Trennflächenspuren	17	
Trennflächenfrequenz	0.7907	Trennflächenspuren/m
Mittelwert	1.26	m
Standardabweichung	1.06	m
Minimum	0.00	m
Maximum	3.18	m
Länge der Trennflächenspuren	34.95	m
Mittlere Länge der Trennflächenspuren	2.06	m
Standardabweichung der Länge der Trennflächenspuren	1.51	m
Länge der Kluftbrücken	0.28	m
Mittlere Länge der Kluftbrücken	0.28	m
Standardabweichung der Länge der Kluftbrücken	0.00	m

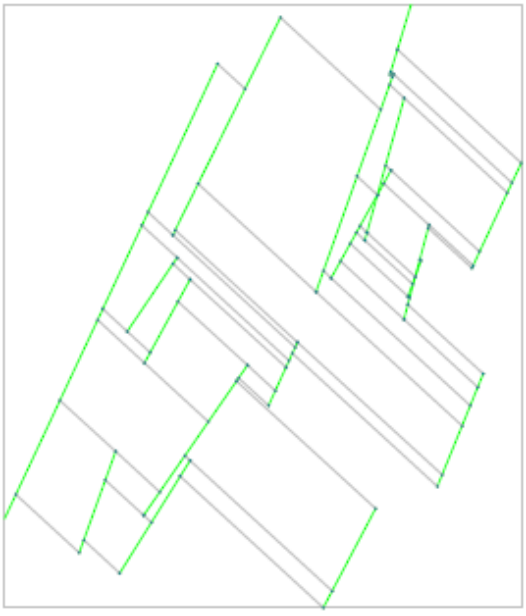

- **Statistical details for structural set 3**

Orientation measurements parameters

Beschreibung	Wert	Einheit
Fallrichtung	57.43	°
Fallwinkel	89.24	°
Sphärische Öffnung	11.20	°
Konzentration	51.85	
Orientierungsgrad	96.23	%
Vertrauenskegel	2.95	°
Konfidenz	95.0	%
Anzahl an Orientierungsmessungen	46 / 46	

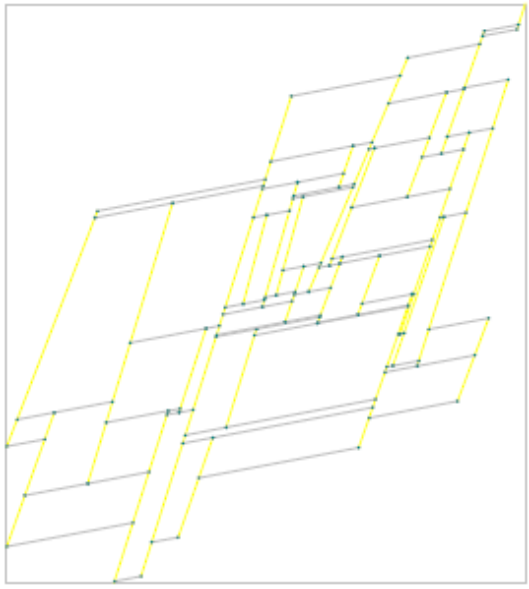

Trace measurements parameters

Beschreibung	Wert	Einheit
Anzahl an Trennflächenspuren	25	
Trennflächenfrequenz	1.0665	Trennflächenspuren/m
Mittelwert	0.94	m
Standardabweichung	0.78	m
Minimum	0.04	m
Maximum	3.54	m
Länge der Trennflächenspuren	58.55	m
Mittlere Länge der Trennflächenspuren	2.34	m
Standardabweichung der Länge der Trennflächenspuren	1.65	m
Länge der Kluftbrücken	0.00	m
Mittlere Länge der Kluftbrücken	0.00	m
Standardabweichung der Länge der Kluftbrücken	0.00	m

- **Statistical details for structural set 4**

Orientation measurements parameters

Beschreibung	Wert	Einheit
Fallrichtung	185.97	°
Fallwinkel	80.85	°
Sphärische Öffnung	20.58	°
Konzentration	13.49	
Orientierungsgrad	87.65	%
Vertrauenskegel	18.92	°
Konfidenz	95.0	%
Anzahl an Orientierungsmessungen	6 / 6	

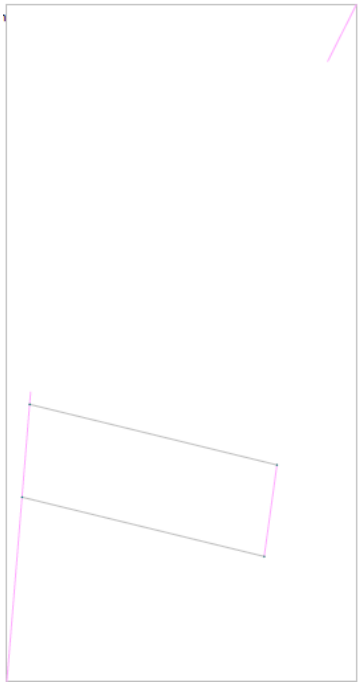

Trace measurements parameters

Beschreibung	Wert	Einheit
Anzahl an Trennflächenspuren	3	
Trennflächenfrequenz	0.7047	Trennflächenspuren/m
Mittelwert	1.42	m
Standardabweichung	0.02	m
Minimum	1.40	m
Maximum	1.43	m
Länge der Trennflächenspuren	2.63	m
Mittlere Länge der Trennflächenspuren	0.88	m
Standardabweichung der Länge der Trennflächenspuren	0.73	m
Länge der Kluftbrücken	0.00	m
Mittlere Länge der Kluftbrücken	0.00	m
Standardabweichung der Länge der Kluftbrücken	0.00	m

- **Statistical details for structural set 5**

Orientation measurements parameters

Beschreibung	Wert	Einheit
Fallrichtung	174.48	°
Fallwinkel	14.69	°
Sphärische Öffnung	21.89	°
Konzentration	13.64	
Orientierungsgrad	86.11	%
Vertrauenskegel	9.43	°
Konfidenz	95.0	%
Anzahl an Orientierungsmessungen	19 / 19	

Trace measurements parameters

Beschreibung	Wert	Einheit
Anzahl an Trennflächenspuren	15	
Trennflächenfrequenz	0.7747	Trennflächenspuren/m
Mittelwert	1.29	m
Standardabweichung	0.86	m
Minimum	0.05	m
Maximum	2.87	m
Länge der Trennflächenspuren	22.04	m
Mittlere Länge der Trennflächenspuren	1.47	m
Standardabweichung der Länge der Trennflächenspuren	1.21	m
Länge der Kluftbrücken	1.21	m
Mittlere Länge der Kluftbrücken	0.30	m
Standardabweichung der Länge der Kluftbrücken	0.30	m

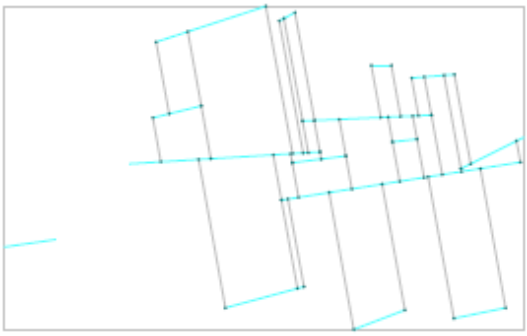

10. Outcrop 10

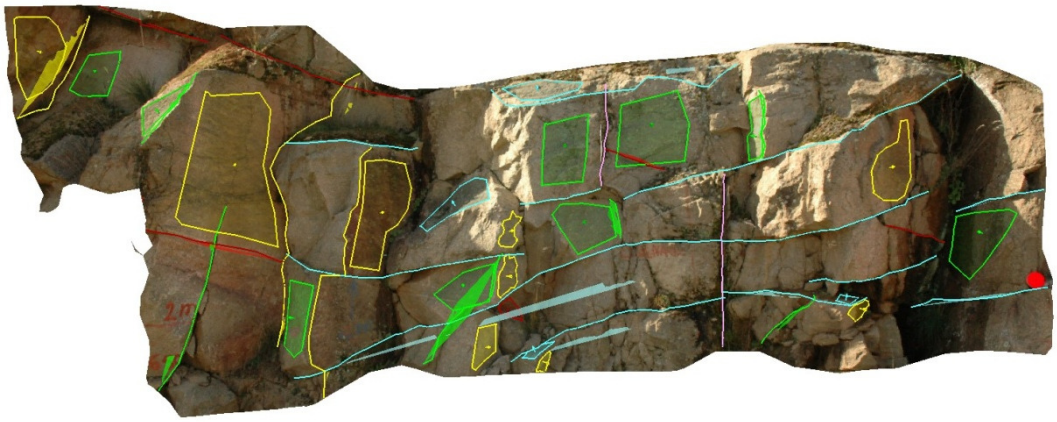

3D Model of Outcrop 10

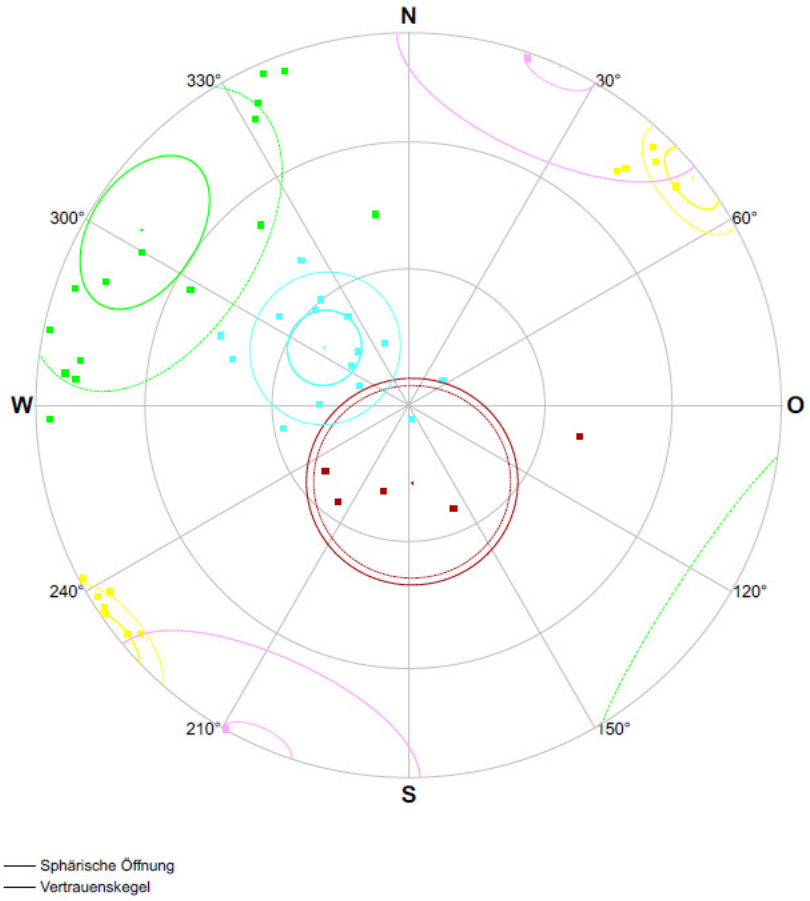

Orientation measurements of outcrop 10 (LHRC - Lambert projection).

- **Statistical details for structural set 1**

Orientation measurements parameters

Beschreibung	Wert	Einheit
Fallrichtung	357.31	°
Fallwinkel	17.05	°
Sphärische Öffnung	21.30	°
Konzentration	12.13	
Orientierungsgrad	86.81	%
Vertrauenskegel	22.89	°
Konfidenz	95.0	%
Anzahl an Orientierungsmessungen	5 / 5	

Trace measurements parameters

Beschreibung	Wert	Einheit
Anzahl an Trennflächenspuren	5	
Trennflächenfrequenz	0.4677	Trennflächenspuren/m
Mittelwert	2.14	m
Standardabweichung	0.06	m
Minimum	2.10	m
Maximum	2.18	m
Länge der Trennflächenspuren	6.35	m
Mittlere Länge der Trennflächenspuren	1.27	m
Standardabweichung der Länge der Trennflächenspuren	0.64	m
Länge der Kluftbrücken	0.00	m
Mittlere Länge der Kluftbrücken	0.00	m
Standardabweichung der Länge der Kluftbrücken	0.00	m

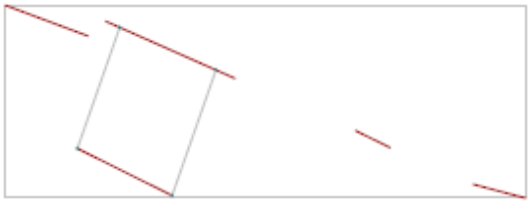

- **Statistical details for structural set 2**

Orientation measurements parameters

Beschreibung	Wert	Einheit
Fallrichtung	123.30	°
Fallwinkel	74.50	°
Sphärische Öffnung	29.49	°
Konzentration	7.70	
Orientierungsgrad	75.77	%
Vertrauenskegel	14.74	°
Konfidenz	95.0	%
Anzahl an Orientierungsmessungen	15 / 15	

Trace measurements parameters

Beschreibung	Wert	Einheit
Anzahl an Trennflächenspuren	6	
Trennflächenfrequenz	0.7352	Trennflächenspuren/m
Mittelwert	1.36	m
Standardabweichung	1.19	m
Minimum	0.00	m
Maximum	2.67	m
Länge der Trennflächenspuren	5.81	m
Mittlere Länge der Trennflächenspuren	0.97	m
Standardabweichung der Länge der Trennflächenspuren	0.55	m
Länge der Kluftbrücken	0.00	m
Mittlere Länge der Kluftbrücken	0.00	m
Standardabweichung der Länge der Kluftbrücken	0.00	m

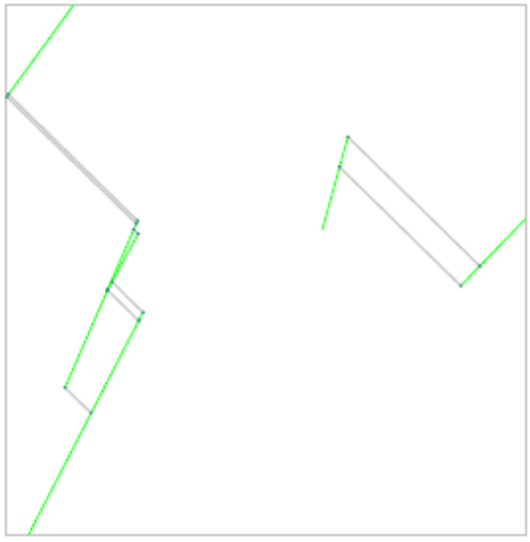

- **Statistical details for structural set 3**

Orientation measurements parameters

Beschreibung	Wert	Einheit
Fallrichtung	231.31	°
Fallwinkel	87.37	°
Sphärische Öffnung	10.28	°
Konzentration	57.52	
Orientierungsgrad	96.81	%
Vertrauenskegel	5.77	°
Konfidenz	95.0	%
Anzahl an Orientierungsmessungen	12 / 12	

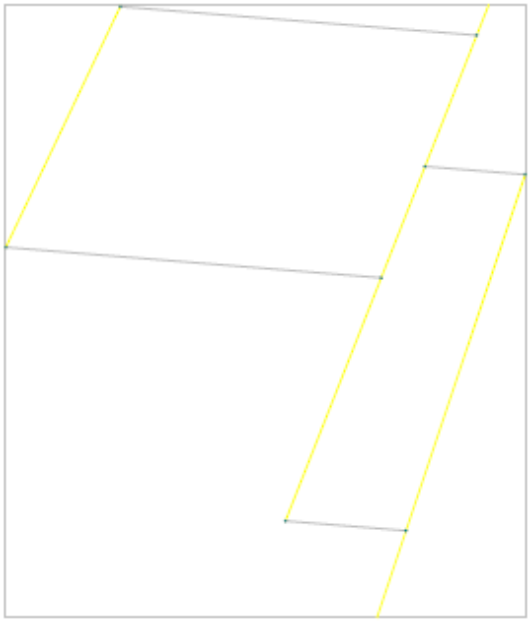

Trace measurements parameters

Beschreibung	Wert	Einheit
Anzahl an Trennflächenspuren	3	
Trennflächenfrequenz	0.6085	Trennflächenspuren/m
Mittelwert	1.64	m
Standardabweichung	1.02	m
Minimum	0.69	m
Maximum	2.59	m
Länge der Trennflächenspuren	6.79	m
Mittlere Länge der Trennflächenspuren	2.26	m
Standardabweichung der Länge der Trennflächenspuren	0.81	m
Länge der Kluftbrücken	0.00	m
Mittlere Länge der Kluftbrücken	0.00	m
Standardabweichung der Länge der Kluftbrücken	0.00	m

- **Statistical details for structural set 4**

Orientation measurements parameters

Beschreibung	Wert	Einheit
Fallrichtung	204.17	°
Fallwinkel	89.62	°
Sphärische Öffnung	5.90	°
Konzentration	94.74	
Orientierungsgrad	98.94	%
Vertrauenskegel	25.95	°
Konfidenz	95.0	%
Anzahl an Orientierungsmessungen	2 / 2	

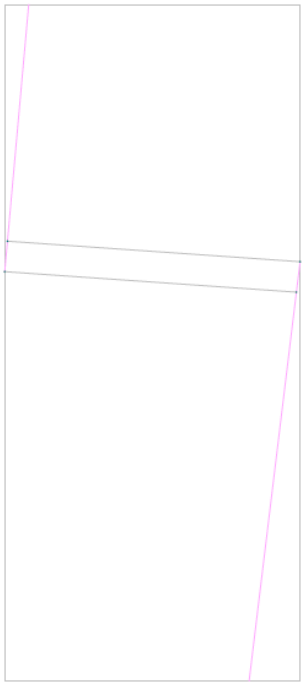

Trace measurements parameters

Beschreibung	Wert	Einheit
Anzahl an Trennflächenspuren	2	
Trennflächenfrequenz	0.8789	Trennflächenspuren/m
Mittelwert	1.14	m
Standardabweichung	0.00	m
Minimum	1.14	m
Maximum	1.14	m
Länge der Trennflächenspuren	2.62	m
Mittlere Länge der Trennflächenspuren	1.31	m
Standardabweichung der Länge der Trennflächenspuren	0.41	m
Länge der Kluftbrücken	0.00	m
Mittlere Länge der Kluftbrücken	0.00	m
Standardabweichung der Länge der Kluftbrücken	0.00	m

- **Statistical details for structural set 5**

Orientation measurements parameters

Beschreibung	Wert	Einheit
Fallrichtung	124.35	°
Fallwinkel	22.31	°
Sphärische Öffnung	16.54	°
Konzentration	23.03	
Orientierungsgrad	91.89	%
Vertrauenskegel	8.14	°
Konfidenz	95.0	%
Anzahl an Orientierungsmessungen	15 / 15	

Trace measurements parameters

Beschreibung	Wert	Einheit
Anzahl an Trennflächenspuren	11	
Trennflächenfrequenz	1.3876	Trennflächenspuren/m
Mittelwert	0.72	m
Standardabweichung	0.34	m
Minimum	0.06	m
Maximum	1.29	m
Länge der Trennflächenspuren	23.51	m
Mittlere Länge der Trennflächenspuren	2.14	m
Standardabweichung der Länge der Trennflächenspuren	1.59	m
Länge der Kluftbrücken	0.00	m
Mittlere Länge der Kluftbrücken	0.00	m
Standardabweichung der Länge der Kluftbrücken	0.00	m